Réponse optique de nuage Rb87 dense

Stephan Jennewein

NNT : 2017SACLO004

THESE DE DOCTORAT
DE L'UNIVERSITE PARIS-SACLAY

préparée à

L'INSTITUT D'OPTIQUE GRADUATE SCHOOL

ÉCOLE DOCTORALE N°572
Ondes et Matière (EDOM)

Spécialité de doctorat : Physique

par

Stephan Jennewein

Réponse optique de nuage Rb87 dense

Thèse présentée et soutenue à Palaiseau, le 23 mai 2017

Composition du jury :

M. Pierre Pillet	Président	Laboratoire Aimé Cotton
M. Guillaume Labeyrie	Rapporteur	Institut non lineaire de Nice
M. Charles Adams	Rapporteur	University of Durham
M. Jerome Beugnon	Examinateur	Laboratoire Kastler Brossel
M. Eric Charron	Examinateur	Institut des Sciences Moleculaires d'Orsay
M. Antoine Browaeys	Directeur de thèse	Institut d'Optique Graduate School
M. Yvan Sortais	Invité	Institut d'Optique Graduate School

Contents

Chapter 1

Introduction

The question "What happens when we shine light onto matter?" has received many answers over the course of history. The concept of a bulk property of dielectrics, the refractive index, can be traced back to the 11th century [1, 2]. The 20th century saw the advent of a more intimate description of the properties of matter as the internal structure of atoms [3] was being discovered and quantum theory established. The accuracy of the models in the description of single atoms or dilute samples achieved nowadays is remarkable [4–6]. Trying to construct matter *ab initio* introduces effects that cannot be included in the mere sum of single atom behaviour as the proximity of atoms is increased [7]. It is with this perspective that work on dense samples is initiated, and it might prove at once edifying to the curious minds and useful to a range of issues in applied science that have been arising in the past ten to twenty years. The fine control over matter commonly exerted nowadays in industrial facilities bring a degree of device miniaturization that was unthinkable forty years ago and finds its place in every household today. The shrinking of useful structures has reached a level where the smallest structure in daily-life products is on the order of 10 nm. Modern computers pack about 1 billion transistors on a chip size of $\sim 1\,\mathrm{cm}^2$. It is not unlikely to see transistors consisting out of single atoms manufactured in the future [8]. As the device density is further increased to speed up the computation, the devices' interface with fast optical communication channels is rendered compulsory. In order to pre-empt possible departures from expected behaviour, a thorough understanding of the impact of density on the atomic response may be crucial.

Another field that might benefit from a fine understanding of dense matter is that of common atomic clocks. Such atomic clocks are commonly embarked on satellites and provide the time to the GPS now standard in all cars and cell phones. Along the way of improving the measurement of time several minute effects have been found (e.g. influence of black body radiation, special and general relativity) that were hampering the advance and had to be understood. These improvements have led to primary standard clocks with an uncertainty as low as $\sim 1 \times 10^{-16}$ [9]. The successive development of optical clocks have reached an absolute frequency uncertainty

of $\sim 2 \times 10^{-18}$[10]. With such high resolution a frequency deviation of the probe light induced dipoles due to density effects could be detected in samples that are orders of magnitude more dilute than in the case discussed before. This offers another perspective to the same question of how matter response to light depending on the matter's density, which if not understood well might be one of the hurdles that prevents us from further improving optical atomic clocks.

In this work I set out to give some answers to exactly this question: "How does light respond to varying density?". To be able to tackle such a question we need a very clean measurement system to properly isolate the effect from any disturbances and we have to be able to change the amount of matter that we put into a volume of constant size. An ideal platform for such an undertaking is provided by cold atoms, which has shown its outstanding performance in many experiments investigating light matter interactions [11–17]. With such a system it is possible to trap atoms inside a vacuum chamber well isolated from external influences by means of intense laser beams. To be able to catch atoms in free space inside an optical dipole trap they have to be extremely cold $< 1\,\mathrm{mK}$ as they would escape the trap otherwise [18]. These traps are formed by tightly focusing a laser beam which then is forming a conservative potential at its focus in which the atoms whose thermal energy is lower than the potential barrier can be trapped. After having trapped the atoms we are going to shine near resonant light onto the sample and measure the amount of scattered light in a given direction. Being able to prepare samples and probe them means that we have to sort out which density ranges we have to explore to get some meaningful insight [19–21]. The so called resonant dipole-dipole interaction (see figure 1.1) can be split into two parts one which is associated with the exchange of photons which can lead to interference effects and a short range interaction which is described by the exchange of virtual photons. A modification of the atomic response due to this light induced interaction starts to be detectable when the interatomic distance is on the order of λ. Indeed, we have to choose the densities that we are going to investigate appropriately, so as to ensure that the modified response is detectable with our apparatus. These resonant dipole-dipole interactions

$$V_{\mathrm{dd}} \propto \hbar\Gamma e^{ikr}\left[\underbrace{\left(\frac{1}{(kr)^3}-\frac{i}{(kr)^2}\right)}_{static}(3\cos^2\theta-1)+\underbrace{\frac{\sin^2\theta}{kr}}_{radiation}\right] \tag{1.1}$$

have three terms scaling like $1/k$, $1/k^2$ and $1/k^3$, where we can associate the long-range $1/k$ term with electro-magnetic radiation and the $1/k^2$ and $1/k^3$ term as the

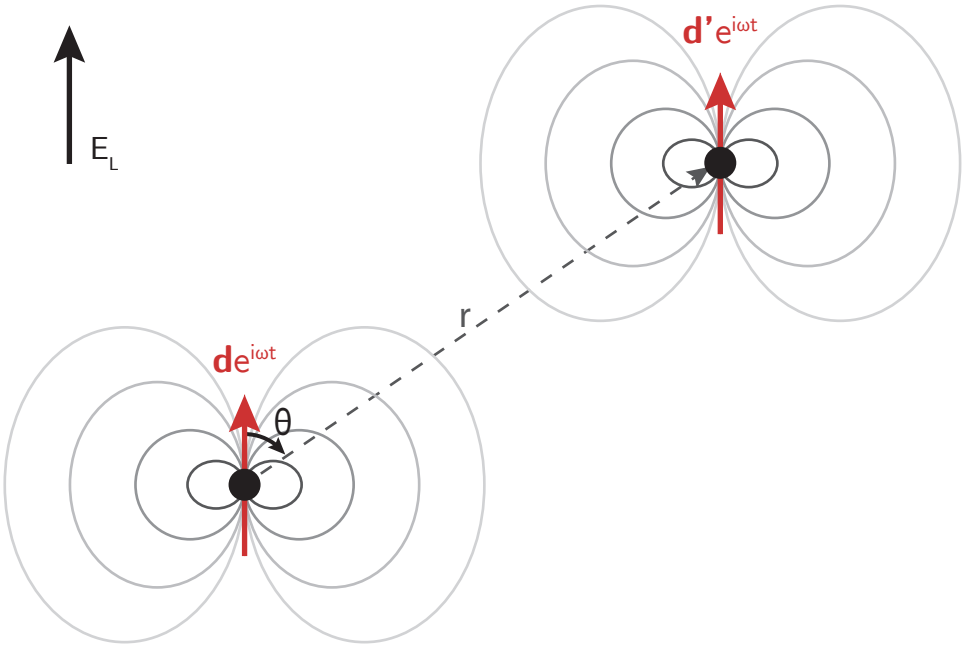

Figure 1.1.: Schematic of two radiating dipoles driven by the E_{L} at frequency ω. Those two dipoles interact via their scattered fields.

electrostatic part, with $k = 2\pi/\lambda$. As a result, when the distance between the scatterers starts to approach $1/k^3$, non-radiative interactions start playing an important role in the sample. As we are working with micro-traps with a volume roughly on the order of $\sim 2\,\mu\mathrm{m}^3$ and the probe light is operated at $\lambda = 780\,\mathrm{nm}$ to be close to resonance with the D_2 transition of Rubidium 87 which we use in our experiment. This indicates that a density of $\sim 10^{14}\,\mathrm{atoms\,cm}^{-3}$ is needed to fulfill the criteria mentioned above. So far different approaches in the field of atomic physics were taken to study density effects and we can group them as followed:

1. Cold atoms with low density $n/k^3 \ll 1$ and large optical thickness e^{-OD} with $OD > 1$:

   Such systems are used in the groups of Havey [5] , Kaiser/Labeyrie [16], Wilkowsky [23]

2. Hot gaseous vapours with large densities $n/k^3 \gg 1$ and low optical thickness

   In the group of Charles Adams [24]

3. Cold atoms with high density $n/k^3 \approx 1$ and low optical thickness

Are used in our group [25]

The theoretical description of such systems can be tackled from two different point of views. The first is a macroscopic approach describing the full sample by a single quantity, the refractive index. This approach had been used before by the group of Charles Adams for their experiment where they measure the transmission of near resonant light on a hot vapour contained in microscopic cell [26]. They measured a strong shift of the resonance when they increased the density, which was confirmed by the textbook theory of refractive indices in dense media the so called "Lorentz-Lorenz" formula [27].

The second perspective is a microscopic view, where all characteristics of the sample constituents have to be known. In our case that would be the individual position of each atom in the cloud. Knowing that all particles are identical the scattered light pattern can be calculated and compared to measurements. This was done for elastically scattered light observed under 90 degrees with respect to the probe light in our group shortly before I arrived and was the work of Pellegrino and Bourgain [25, 28, 29]. Unlike the Adams' group we did not measure a significant shift. In addition the agreement we were able to establish between model and experiment was only on a qualitative level. Having two contradicting results for similar measurements is always an unsettling situation. To resolve this problem we wanted to compare the two theories to one another and to an experimental measurement. This comparison could only be done by switching from measuring scattering under 90 degrees to transmission experiments as these two situations measure two different parts of the probe light. As our sample consists out of atoms at random position the rescattered field inside the medium can be split into two parts an average field $\langle \mathbf{E}_{\mathrm{sc}} \rangle$ and a deviating field $\delta\mathbf{E}$ so that $\mathbf{E}_{\mathrm{tot}} = \langle \mathbf{E}_{\mathrm{sc}} \rangle + \delta\mathbf{E}$ is fulfilled (the average here being a position average). As shown in [30] only the evolution of the average field can be described by macroscopic Maxwell's equations dominating in the forward direction and thus is governed by a refractive index. Measuring under 90 degrees is thus mainly sensitive to the $\delta\mathbf{E}$ of the light field and to compare our measurements directly to the microscopic theory and to a description by macroscopic Maxwell's equation we had to switch to transmission measurements.

Outline of this thesis

To be as stable as possible some technical improvements of the existing experimental setup were necessary. A completely new control system was needed to maximize the repetition rate, thereby improving the statistical sampling of the data to an appropriate degree. These changes are documented in chapter 2 and enabled us to perform the accurate measurements which were conducted afterwards. The first measurements performed with this upgraded system were transmission experiments on "degenerate" Rubidium 87 (12-level system / full internal structure) with a weak driving field. We investigated the steady-state response of a sample for various densities which were modelled by both a macroscopic and microscopic theory. This measurement procedure is described in chapter 3 followed by an introduction of the theoretical framework and a discussion on the discrepancies observed between measurement and theory.

In chapter 4 we investigate the propagation of a Gaussian shaped pulse through the very same sample. Measuring the delay and advance of the peak of such a pulse gives access to the phase imprint by the material it is passing through. With this second measurement we were able to infer phase and magnitude of the scattered field independently. Additionally looking at this pulse propagation allowed us to measure the group-delay as well as the fractional pulse delay/advancement, which turned out to be the largest ever measured while still having 20% transmission. Extrapolating these extraordinary values to a signal level which other groups still consider measurable (1%) would allow to test the theoretical predictions [31, 32] for the fractional-group advancement.

The last chapter 5 starts with the preparation of Rubidium 87 in a pure Zeeman state, while being in a dense sample, thus removing the internal degrees of freedom and moving from a 12-level to a 2-level system by lifting the degeneracy with a strong magnetic field. Afterwards the measurements described in chapter 3 are repeated for the spin polarized sample and the results are systematically compared to the "old" ones. This is followed by a comparison of the new measurements to the microscopic theory. Not having to care about internal degrees of freedom removes all doubt about this aspect of the simulation which was a major concern before. As the quality of the results obtained with polarized samples was substantially better, we could analyse the transient behaviour as well, which are in good agreement with the steady state results.

As an attempt to get further insight into the effect of density on the scattering properties of atoms, I also started to explore the high saturation regime where quantum effects may dominate. By doing so I found that the saturation intensity of the line

probed is not constant with density.

Chapter 6 summarizes the whole thesis and gives an outlook to future experiments.

Chapter 2

Technical changes on the setup

To be able to properly investigate systems such as ours which consist of only few atoms $1-200$ it is crucial to repeat experiments many times to form a proper statistical sample. This repetition has to be performed with diligence as it would lead to an additional source of uncertainty otherwise. Repetitions have to be as identical as possible within the required accuracy, such a task is nowadays best performed by computers. Another key aspect is the flexibility of one's experimental setup to change the measurement protocol as the majority of data acquisition is for the urge of closing loopholes in the assumed model e.g. uncertainties, noise, biases, etc.. This process is very important as otherwise an already understood effect could be misinterpreted and would lead to utter nonsense.

To be in the comfortable situation where we can operate our experiment with a high level of reliability and flexibility I implemented a new control system and the optics mounts were upgraded to the most recent version. This chapter describes where we started from and how the apparatus was operated before and through which developments we arrived at a stage where the before mentioned needs are fulfilled.

2.1 The old setup

The data acquisition of a full dataset on our setup requires on the one hand a repetition of the same measurement sequence and on the other hand the variation of one or several experimental parameters. In the course of this chapter I will call the former "cycles" and the latter "run", see figure 2.1. In practice, a cycle is started when the avalanche photodiode on our experiment measures a certain level of fluorescence from our magneto-optical trap (MOT). In the software, we define a threshold level at which a trigger is send out to a digital output card. As one can see in figure 2.1 our typical sequence can be broken down into three parts, first pattern 1, which is normally the loading of our dipole trap, second pattern 2 the experiment, consisting of a repetitive structure and third pattern 3 the reinitialization of our equipment at

the end of a sequence. In our old setup the repetitive structure was generated by a series of independent pulse generators and logic gates, which were connected to the digital card. To achieve any form of complex sequence the wiring up of those pulse generators and logic gate formed a very difficult task in itself. Another problem was the repeatability of an experiment, the installed wiring together with the values set on each device had to be minutely recorded in our lab book for future measurements. In case of repeating an old experiment the very same setup had to be put together again and all wire connections needed to be installed.

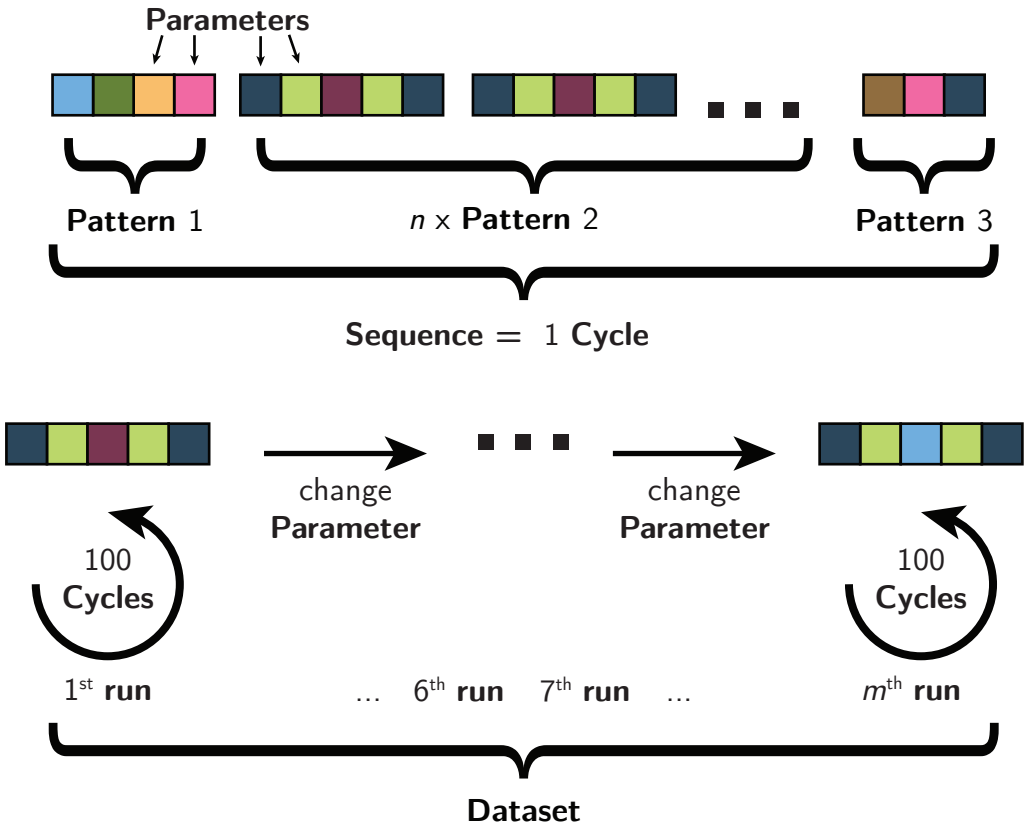

Figure 2.1.: Example of a typical sequence and the structure of a dataset.

Due to the fact that the loading rate of the MOT, which determines the measured level of fluorescence is a non-deterministic process, the time required to reach the triggering threshold can vary significantly (1-10 s). We normally acquire data of our atomic sample by taking pictures with an intensified charge coupled device (I-CCD) or recording the temporal arrival of single photons with the avalanche-photodiode (APD) being connected to a time-tagging device. When we were using the camera it was normally integrating over a full run, which consists for example of a hundred cycles and only read-out the final signal at the end. The problem with this method is that

the camera gets an exposure time set at the beginning, which cannot be changed or interrupted after arming the camera, otherwise the picture is lost. Knowing that the camera needs a fixed exposure time and that the trigger rate is not constant in time leads to a dilemma: either the camera misses events because the exposure time is up before all cycles have been performed or the exposure time needs to be overestimated to make sure the camera captures everything, which leads to a reduced repetition rate. Typically we overestimated the exposure time by a factor of two. At the end of the acquisition, the data had to be saved by hand and converted into a format which was readable by our analysis software. To prepare the experiment for the next run, the operator had to set the new values on the parameters that needed to be changed for example, change the power of a laser beam by turning a half-wave plate or changing the output frequency of a frequency-generator manually.

The combination of the long exposure time, the lack of automation of the change of experimental parameters, together with the manual data saving made for unnecessarily lengthy experimental runs, as well as a high likelihood of making mistakes. The increased complexity of the phenomena explored with our system meant that more and more parameters needed to be perfectly controlled. Therefore we decided to perform the following upgrades:

1. Optimize the beam path to gain beam pointing stability and free space on the optical table

2. Design a new computer control allowing to manage all parameters from a central place as well as automated data acquisition

3. Develop an analysis software which could handle the increased amount of data and integrates nicely into the automated data taking

2.2 Optical Table

I planned the new beam path to optimize the path length and limit the number of optical elements. This new setup freed about a third of the optical-table which is now available for future upgrades. In addition we changed the mirror-mounts and fiber-coupler mounts to the latest version of the Lioptec Star series. This product uses screws with a wider diameter than our old mounts, which probably reduces the play on each thread-turn thereby reducing the amount by which the screw can relax after having been adjusted. Those two changes improved the beam-pointing

stability roughly by a factor of three, meaning that instead of having to re-adjust the mirror-mounts and fiber-couplers every second day we only have to do it once a week.

As doubts over alignment are significantly reduced, more demanding measurements requiring either more time or complexity are now within reach.

2.3 Computer Control

2.3.1 Concept

On the hardware side the computer control consists of three National Instruments cards, one counting card (NI-6601), one digital output card (NI-6534) and one analog output card (NI-6713). These cards were already part of the "old" setup and kept unchanged in the new setup, while the software environment was completely rewritten.

As described in section 2 we trigger the experiment after the measured amount of fluorescence of the MOT exceeds a threshold level. To measure this level automatically the APD is connected to the counting card, which counts the number of pulses generated over a certain time interval. When this value exceeds the required threshold the counting card sends a trigger to the digital output card to start an experimental cycle during which control signals are sent to the analog card, as well as frequency generators, acousto-optic modulators and shutters. This cycle is repeated n times, during which either an I-CCD camera integrates the spatial signal or a time-tagging device (TimeHarp 200) measures the photon arrival time of our atomic sample. After these repetitions the acquired data can be saved manually and the parameters for the next run have to be changed by hand.

The new control system I developed performs the same sequence, but also allows automatic control of the instruments by means of a communication system between several computers, which is directly implemented in software. The National Instrument cards, which we use to control our experiments are installed in two different computers and a third computer is used for data acquisition. I planned and implemented a synchronization protocol that uses the local area network to which all three computers are connected, see figure 2.2. The new system, on top of allowing the repetition of cycles also allows to change an arbitrary number of parameters and automatically starts the next run. This allows fully automatic data acquisition over an arbitrarily large parameter space, without any other manual input than defining the series of sequences at the very beginning of the measurement.

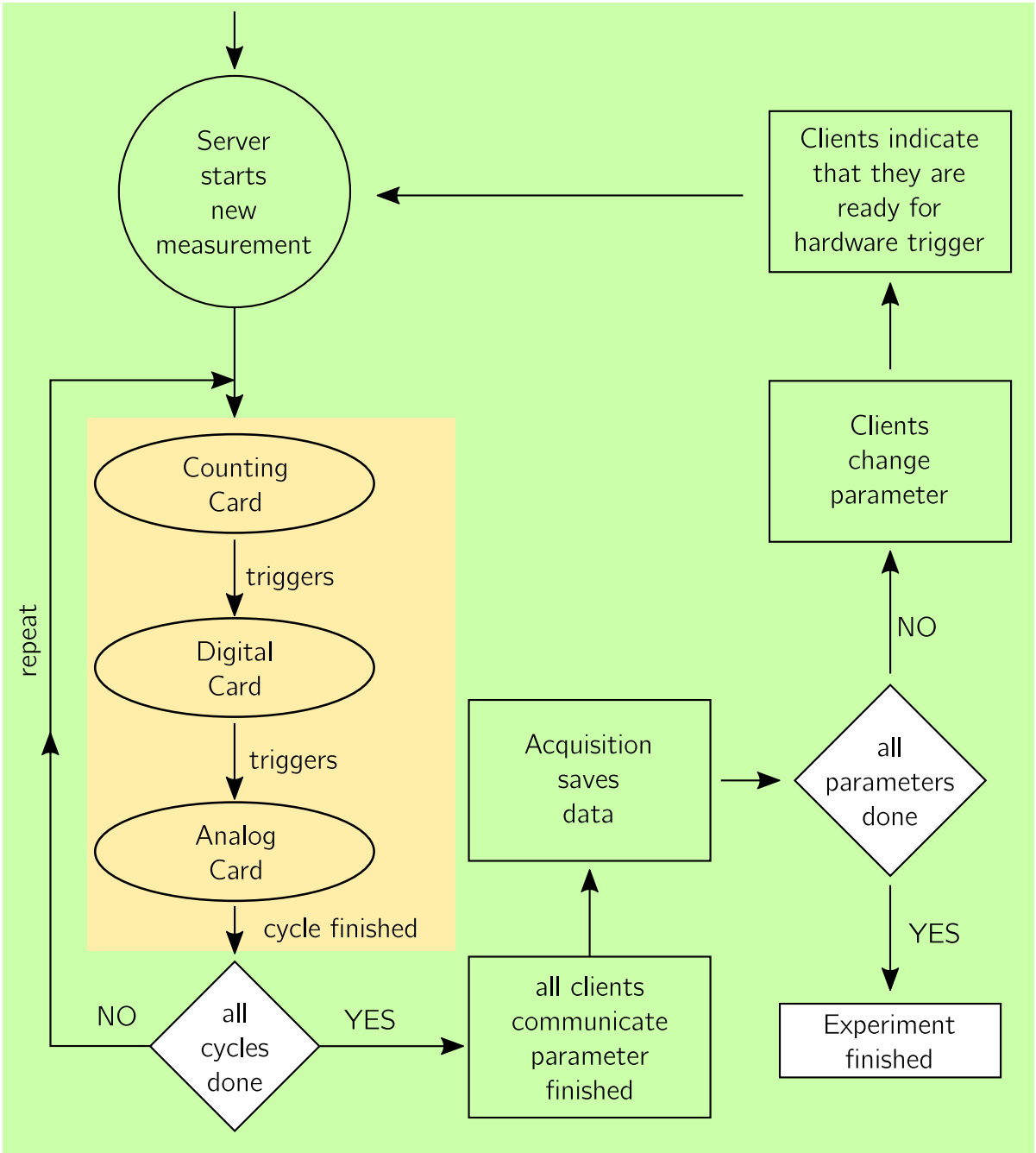

Figure 2.2.: Flowchart of the synchronization protocol of the computers when taking data automatically. The yellow background indicates hardware and the green background software communication.

In our scenario the counting card software acts as the central communication hub (server) to which the other cards' software connect. After connecting on a software level the various clients indicate that they are ready for the measurement and are waiting for a hardware trigger. The latter is repeated until all cycles of one run have been performed. When a run is finished the software checks if there are more runs to be done, if so it changes the parameters for the next one and starts over again, otherwise the measurement finishes, see figure 2.2.

In order to simplify the implementation of repetitive patterns, which was performed by hardware connection of many pulse generators and logic gates, I split the definiton of the sequence in two parts, in software. The first states the concrete implementation (pattern) and the second defines the order in which these implementations (flow) are output or even repeated, see figure 2.4. By doing so it is possible to define the full sequence on the computer without the need of pulse-generators or logic-gates. This way of defining a sequence also allows us to conveniently save and load everything on a computer, which solves the repeatability issue inherent to the hardware concatenation of pulse generators.

2.3.2 Implementation

For this size of project I preferred working with a modern, object-oriented programming language. National Instruments directly provides libraries for Microsoft .NET and all of our laboratory computers are running Microsoft Windows as their operating system, so the natural choice was to use Visual C#. Microsoft provides a very feature rich and easy to use integrated development interface (IDE) for free "Visual Studio Community", which also allows to implement rich graphical user interfaces. For the data acquisition I decided to use Matlab to ease the data analysis, which is performed in Matlab as well (chapter 2.4). In the following sections I present the graphical user interfaces that I designed and implemented and will explain some of their features and concepts.

Graphical User Interface Analog Card

Figure 2.3 shows one of the six patterns of the analog card, which has eight channels (rows) and five time steps (columns). Each channel ranges from $-10\,\mathrm{V}$ to $+10\,\mathrm{V}$, but can be calibrated to any other unit by loading a comma-separated-value (CSV) file in which the first column states the voltage and the second column states the

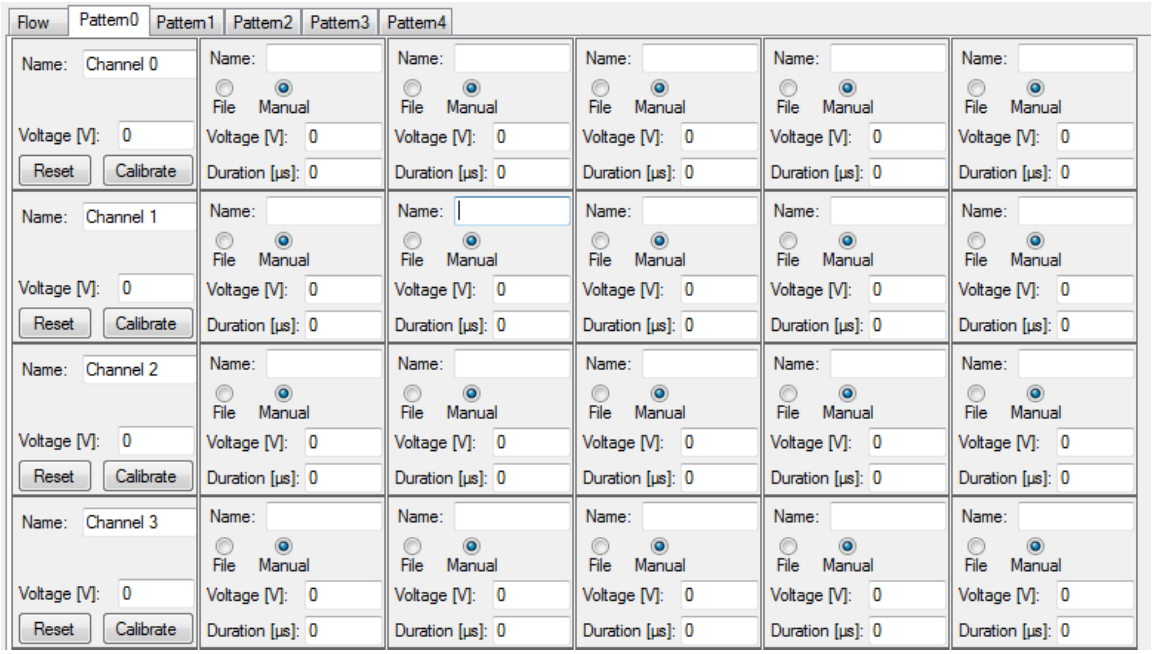

Figure 2.3.: Showing part of the analog card's user interface: 4 out of 8 channels with 5 time steps each

new desired unit. The first row of this file is used to change the unit in the user interface. Afterwards any value between the minimum and maximum value defined in this CSV-file can be used and the output is generated by linear interpolation between the provided calibration points. Time steps can be given a name to make it easier to remember its function, as well as a value and a duration. If two consecutive time steps have different values, a linear ramp is calculated starting from the first value to the second one over the duration of this step. If any more complicated ramp is necessary, it can be loaded from a file with a series of values in CSV format. The total duration of one pattern is given by the channel with the longest duration and the other channels remain in their final value until the end of the pattern is reached. The order in which the patterns are output is defined in a text box located in first tab

Graphical User Interface Digital Card

Figure 2.4 shows one out of six patterns of the digital control, which has 32 channels (rows) and 20 time steps (columns). The time per step is defined for the full column and it can be decided to switch each channel on/off during this time step by clicking the corresponding box. Each time-step can be labeled with a name to state its function.

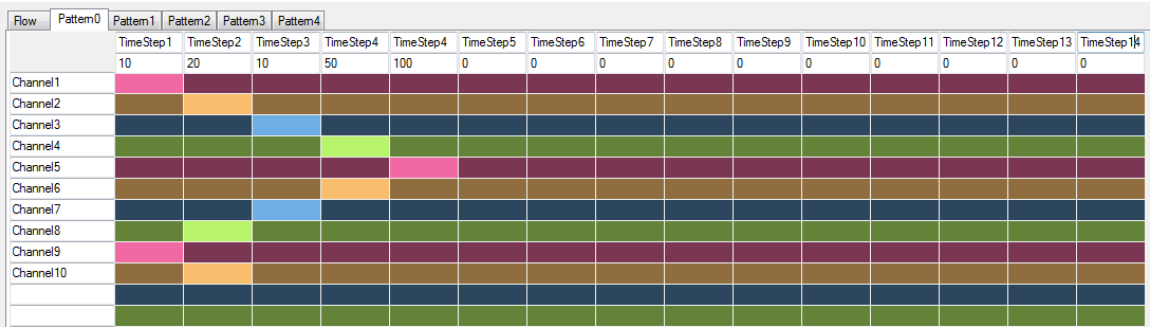

Figure 2.4.: Graphical excerpt of the digital card's user interface showing the first 12 channels with 14 time steps.

Graphical User Interface Counting Card

Input fields:

1. **Binning**: Defines the time over which the counting card sums the APD pulses
2. **Threshold**: Defines the level above which a trigger is sent to the instruments to start an experimental run
3. **Detection bins**: Defines the number of times the threshold has to be exceeded before sending a trigger.
4. **Cycles**: Defines how many cycles are performed.
5. **Runs**: Defines the number of runs for the dataset.
6. **Monitoring/Measurement**: In monitor mode the top chart only shows the integrated APD signal but no triggers are sent. In Measurement mode it also sends triggers, when the threshold is exceeded.
7. **Reference Run**: By activating this field an alternative threshold as well as a different number of cycles can be defined for every second run.
8. **Network**: Shows the list of connected clients via network connection.
9. **Frequency Generator**: Sets a frequency at which triggers are sent.
10. **APD Signal**: Shows the temporal signal acquired from integrating the APD pulses
11. **APD Counter Histogram**: Shows the histogram of the signal seen in APD Signal.

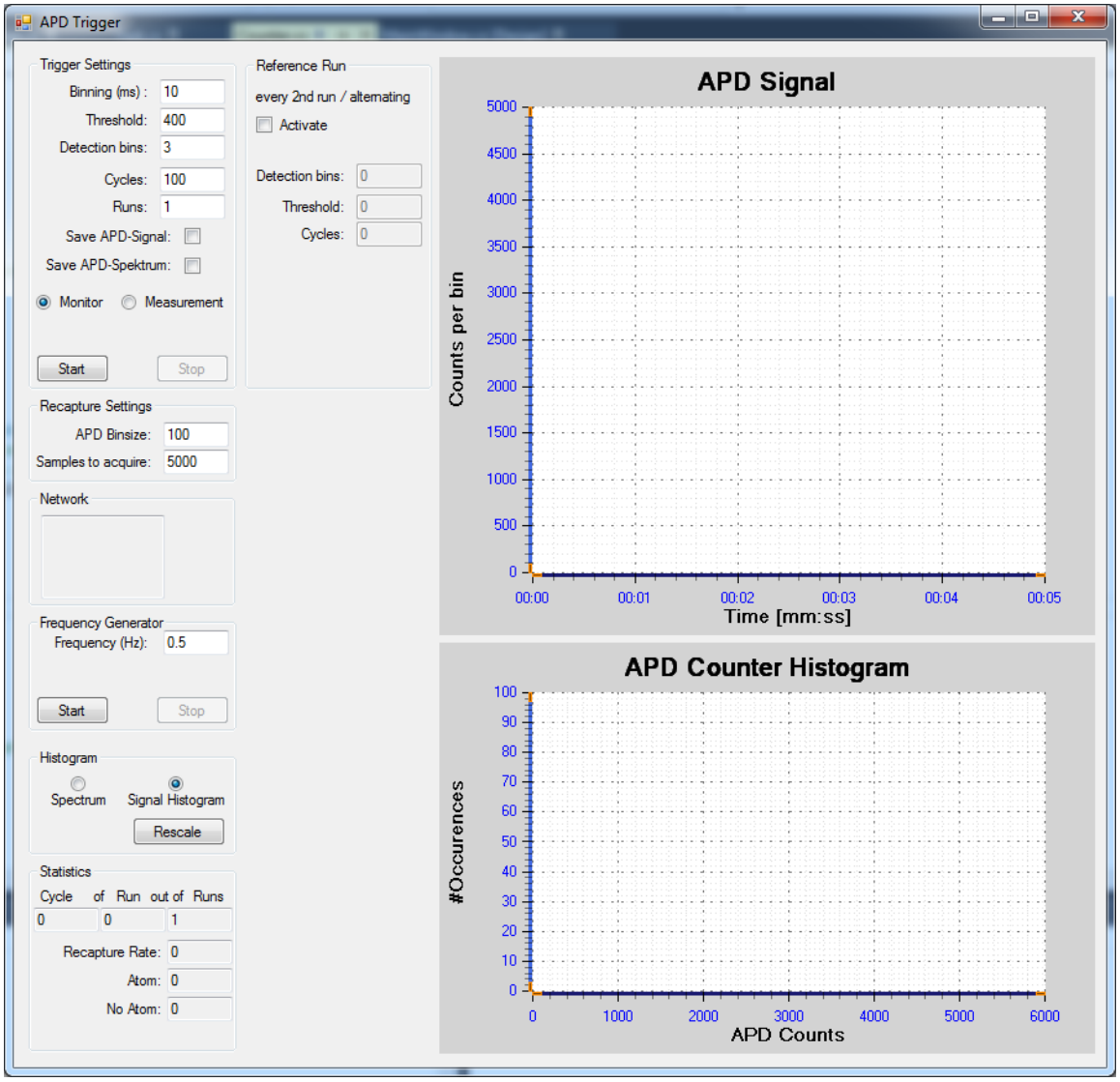

Figure 2.5.: User interface counting card.

The remaining elements are not relevant for the measurements performed in this thesis and are not discussed here.

IEC-625-Bus/GPIB

Many of our scientific instruments support GPIB to interface them to a computer. To be able for example to change a frequency or read out our spectrum analyzer I installed a USB-GPIB-adapter on the computer hosting the digital output card and integrated it into the user-interface, see figure 2.6. In this interface GPIB commands can be freely stated and iterators can be used by writing the name of an iterator, which are highlighted by a blue background. Sometimes we make use of an arbitrary

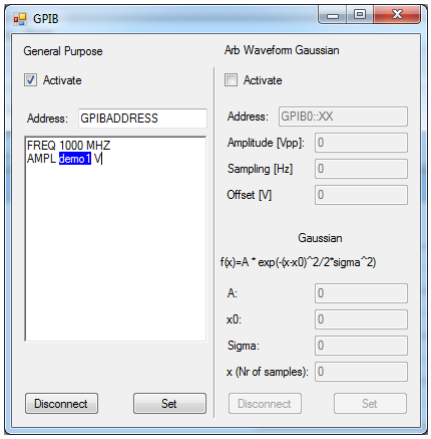

Figure 2.6.: Control Panel for GPIB. On the left hand side the text box for GPIB commands can be seen, on the right hand side the input fields for the Gaussian pulse generation are greyed out until activated. The text in the text box with blue background indicates the usage of an iterator.

waveform generator, which most of the time is used to output Gaussian pulses. To make it convenient to use I implemented a special input field for Gaussian pulses, which allows to enter the full-width-half-maximum (FWHM), amplitude and offset of this function. Those parameters are then used to calculate the values which are output via the arbitrary waveform generator.

Parameters/Iterators

The element in my software which allows to change parameters automatically is called an "iterator". As shown in figure 2.7 a list with an arbitrary amount of iterators can be defined, each of them has a name and a ordered list of values. When doing automated runs the system has an internal counter which determines which value in the list has to be used for the run. The iterator can be assigned to the duration of time steps, as output values for analog channels. It is even possible to use those iterators to completely toggle the state of a digital output channel so that in one run during a time step the channel is on and in the following it is off. Another place where iterators can be used is in the "GPIB" panel, where the name of the iterator can be written and is then highlighted by a blue background. This gives the necessary flexibility to create sequences which acquire a whole data set automatically.

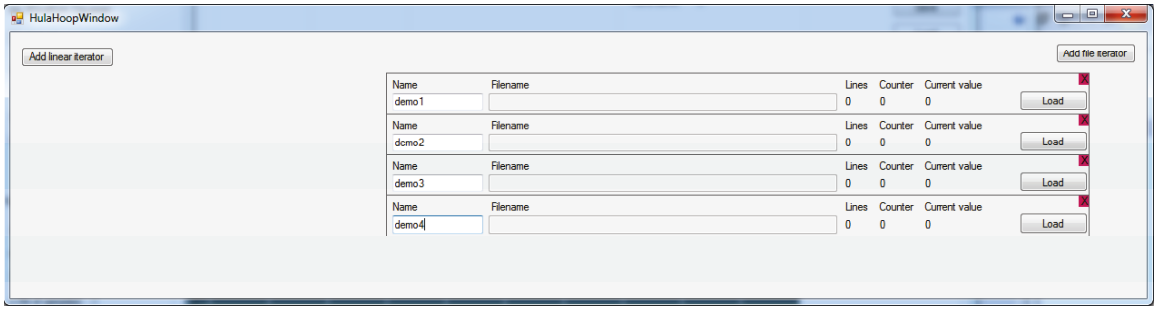

Figure 2.7.: This shows the control element to define and load iterators.

Acquisition

In our experiments two systems are used to acquire data, either an I-CCD, which gives us access to spatial phenomena or a time-tagging device (TimeHarp 200), which measures the arrival time of the APD pulses with a nanosecond resolution.

In order to interface the I-CCD I made use of a freely available Matlab wrapper[1] and modified it to our needs. As for the time-tagging card I wrote a wrapper from its provided C-library to be able to use it in Matlab. This finer control over the camera allowed me to set the exposure time to a very short value and acquire a picture for each cycle instead of integrating over the full run. Those individual pictures are then summed up in software, which produce a full picture as soon as the run is finished. With this method a full picture is acquired as soon as all cycles are performed and there is no uncertainty about the exposure time anymore. It still takes more time if the trigger rate drops, but at all times it is guaranteed that we do not loose a cycle due to underestimating the camera's exposure time.

2.4 Data Analysis

In the past we had a monolithic analysis code which was written in IgorPro and it consisted of approximately 3000 lines of code. I rewrote this analysis in Matlab splitting the various functionalities of the original software into small comprehensible chunks. The core analysis which consists of "background subtraction", "fitting the camera picture" and "measuring the amount of atoms" is performed by one function in Matlab, which returns a list of analyzed objects. Any further analysis functions use this list as an input so to avoid doing tasks twice. In addition I defined a file naming structure to enable automatic extraction of experimental parame-

[1] http://www.eng.utoledo.edu/~smolitor/download/matpvcam.zip

ters from the file name by the analysis software. The naming pattern is defined as: `MeasurementName_Parameter1_Value1Unit1_Parameter2_Value2Unit2.extension`. The analysis script then extracts those 3-tuples, each consisting of (Parameter,Value,Unit), which are used for example to plot the measured atom number versus one of the given parameters by just stating the parameter name in the plot function.

Besides the fact that Matlab is a very widely used language that most students learn at some point in their curriculum, writing the analysis software in Matlab has many advantages. The data can be saved in Matlab's own file format, thus making data reloading faster and easier, and allows to make use of Matlab's extensive library of built-in functions. Also, being able to work directly on binary data (as opposed to the ASCII files required in IGOR Pro) saves a significant amount of space on the hard drive. Finally, another major difference is that the analysis results do not necessarily need to be saved as the raw data and the scripts can be saved instead. As a result, the storage space required for a given set of data is reduced by a factor of ten.

2.5 Conclusion

Improving the beam-pointing stability by a factor of three, grants time for more complex measurements. This fact paired with having implemented a computer control system that only needs human interaction to set up the measurement and then runs without any further manual work, allowed me to perform measurements of up to 24 hours duration. The most limiting factor on our setup is now the time for which our lasers stay locked on their frequency reference. Even for shorter measurement streaks, not having to perform manual tasks during the measurements minimizes the total time for a measurement, which is directly reflected in the higher signal to noise ratio in the acquired data. Another important aspect of further experimental automation is the freed workforce, now available for other tasks.

One major problem remains, whenever we started a new measurement streak the number of atoms in our micro-trap might have drifted away. To obtain the required amount of atoms was and still is a long and tedious task for which no clear rule could be found. From time to time just this re-optimizing could take several weeks.

Chapter 3

Coherent Transmission through cold and dense Rubidium 87 clouds

In the field of light scattering by dense media two contradicting results were recently published, on the one hand the work of Charles Adams' group investigating the transmission behaviour through a slab of hot vapour [26], on the other hand the work done in our group looking at the light scattering of a cold atomic sample under a 90 degrees angle [25]. The Adams' group took a macroscopic approach to describe their work theoretically, which clearly agrees very well with the experimental results. Both groups study the scattering behaviour of a sample by varying the density from a dilute to a dense case, but the Adams' group is able to model their outcome with the Clausius-Mossotti equation whereas our group could only establish a qualitative agreement between the microscopic theory and the experimental results.

The scattered light of a sample can be separated into two parts $\mathbf{E} = \langle \mathbf{E} \rangle + \delta\mathbf{E}$, where $\langle \ldots \rangle$ denotes the ensemble average and $\delta \ldots$ the fluctuations (deviation from the average). We call $\langle \mathbf{E} \rangle$ the *coherent* electric field and $\delta\mathbf{E}$ the *incoherent* electric field. Only the coherent electric field can be described by the macroscopic Maxwell's equation. In this chapter I will explain the experimental setup used to measure the coherently transmitted light on a micron-sized atomic sample, which thus can be described by both theories a microscopic and macroscopic one. I will introduce the two theoretical frameworks and establish a qualitative link between the two and then compare them systematically to the acquired data trying to resolve the contradiction of the two publications. When striking disagreements between theory and experiments are found, it is natural to question the rigour of the experimental method as well as the limitations of the applied models. I will thus end this chapter with a discussion of possible experimental and theoretical shortcomings.

3.1 Choice of sample

A sample is considered dilute when its scattering properties are independent of the environment of the scatterer while also maintaining a low optical density. As the density increases (atoms per volume), the close proximity of scatterers may lead to interactions and an effect on the scattering properties of the medium is to be expected. In our atomic sample illuminated by a near-resonant probe, we expect resonant dipole-dipole interactions to be significant when the distance between pairs of scatterers is on the order of $\frac{\lambda}{2\pi}$, with λ the transition wavelength. Expressing this criteria in terms of mean-free path is given by $kl < 1$, where l is the average distance a light wave travels before it is scatters again and $k = \frac{2\pi}{\lambda}$. This directly gives us a rule of thumb for the minimum density ρ for which effects due to these interactions start to be observed: $\rho\left(\frac{\lambda}{2\pi}\right)^3 \geq 1$. In our experiments we probe the D_2 transition of ^{87}Rb at $\lambda_0 \approx 780\,\mathrm{nm}$, which directly dictates that densities as high as $10^{14}\,\mathrm{atoms\,cm^{-3}}$ have to be reached for any influence of the above mentioned interactions to be observed.

At the same time another problem emerges: if the extinction coefficient $OD = -\log(\frac{I}{I_0})$, with I_0 the input intensity and I the output intensity, is too high, the number of photons collected is insufficient to perform any clear measurement. This calls for a geometrically thin, but dense sample. Our experimental setup fulfils both requirements, as the microscopic trap realised on the Aspherix apparatus has a volume of about $2\,\mu\mathrm{m}^3$ where up to 200 atoms can be trapped. Using such a small sample adds another complexity as diffraction of the edges of the sample is no longer negligible thus the convenient description by an extinction coefficient is strictly speaking not possible anymore.

In addition, using a small cloud with only a few hundred atoms is also favourable for the theoretical description in the framework of a microscopic theory where the information of each atom need to be known. Working with many more atoms would be impossible due to the limited computational power of available computer systems.

3.2 Brief Overview of our Experimental Setup

Figure 3.1 shows the main experiment chamber of our vacuum setup. In this chamber are two aspherical lenses ($NA = 0.5$) [33] in a confocal setup. By shining a collimated laser beam onto the first lens it is focused and forms an optical dipole trap. In our case we use two overlapped traps: a macro-trap of $4\,\mu\mathrm{m}$ at $1/\mathrm{e}^2$ and a micro-trap of $1.2\,\mu\mathrm{m}$,

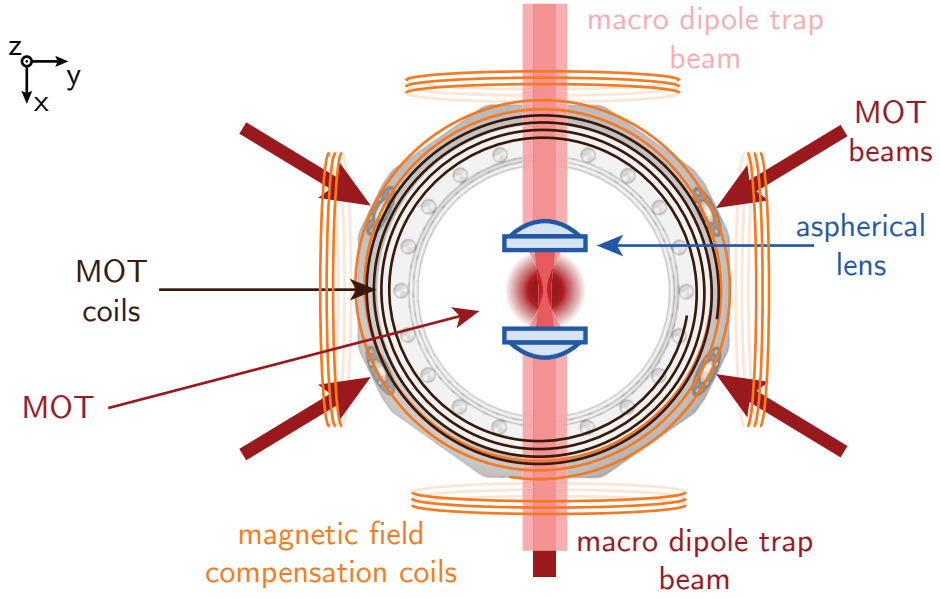

Figure 3.1.: Schematic of our main experiment chamber.

which form a dimple configuration [34]. In order to maximally fill the micro-trap, we first load the macro-trap and then funnel the atoms into the small trap [35]. This technique allows to load up to 200 atoms into the microscopic trap and reach the necessary density of $10^{14}\,\mathrm{atoms\,cm^{-3}}$. Both traps are operated at 940 nm with a trap depth of $U_0 \approx \mathrm{k_B} \times 1\,\mathrm{mK} \approx \mathrm{h} \times 20\,\mathrm{MHz}$ and are orthogonally polarized to prevent interference.

The dipole traps are initially filled from a Zeeman-slower loaded magneto optical trap (MOT) (Zeeman slower not shown on figure 3.1).To apply the necessary magnetic field for the MOT we have two coils in anti-Helmholtz configuration on the outside of our chamber as well as three pairs of compensation coils in Helmholtz configuration along each axis to be able to null the external field down to remaining $\sim 80\,\mathrm{mG}$.

The trapped atoms in the microscopic trap are imaged through one of the aspherical lenses on a camera. Due to the fact that this system is diffraction limited we gain the highest possible resolution of $\sim 1\,\mu\mathrm{m}$ [33]. A detailed description of this setup is given in Andreas Fuhrmanek's PhD thesis [36].

3.3 Imaging System

A confocal lens setup (figure 3.2) is used for the preparation and the probing of the atomic sample. A first lens ($\mathrm{L_1}$) focuses two 940 nm co-propagating laser beams

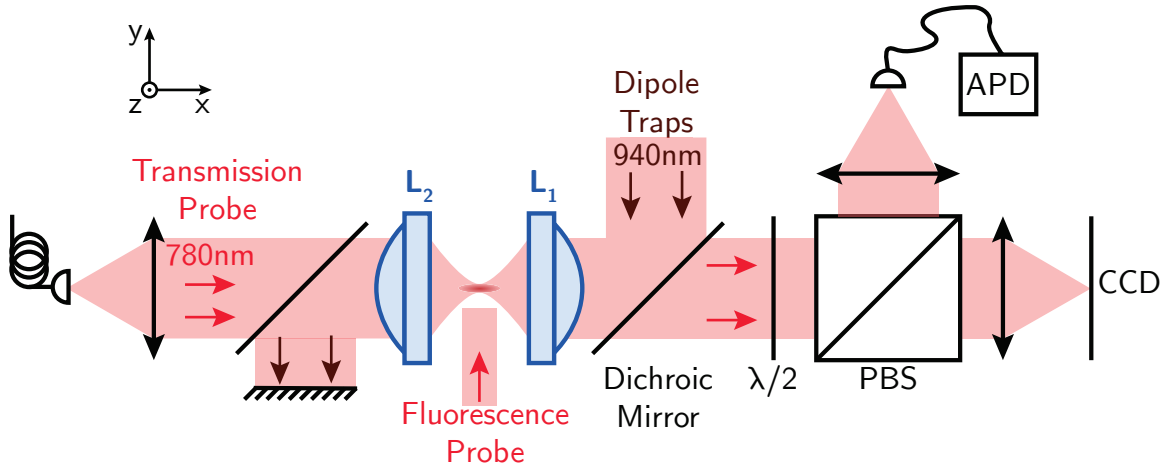

Figure 3.2.: Imaging system used during this thesis. From the left the transmission probe propagates through the cloud and is separated off the dipole-trap beam by an dichroic mirror and is then detected by an APD or an I-CCD. In addition a fluorescence probe beam can be used.

to produce the micro- and macro-traps and to collect the scattered light of the atomic sample. The second lens (L_2) is used to focus a probe beam which is linearly polarized along the y-axis and counter-propagating the trap beams onto the atomic sample to probe the transmission behaviour of the sample [37]. In addition we have a fluorescence probe, which travels along the z-axis of figure 3.2 and is always circularly polarized. It is used for example to measure the number of atoms in a sample. The different wavelengths of the probe 780 nm and the trapping beams 940 nm allow us to separate them with a dichroic plate. Afterwards the light of the probe passes through a half-waveplate which is set so that the following polarizing beam-splitter divides light which is linearly polarized along the y-axis 50:50 between its output terminals. One terminal feeds the light into a single mode fibre which is connected to an avalanche photodiode, which we use together with a time-tagging device (resolution of ~ 150 ps) to measure the arrival time of individual photons and the other terminal is used for an I-CCD to spatially resolve our sample. The I-CCD system in our setup has a quantum efficiency of $\sim 10\%$ which is determined by the efficiency of the intensifier. The APD (Perkin-Elmer SPCM-AQR-14) that we use has a quantum efficiency of $\sim 50\%$.

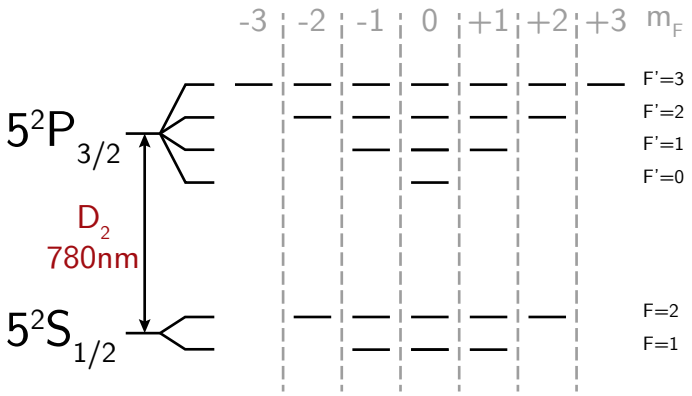

Figure 3.3.: Level scheme of rubidium 87.

3.4 Rubidium 87

This experiment was designed to work with ^{87}Rb atoms [38], which is an atomic species that can be conveniently laser cooled to a few hundred micro-Kelvin [39]. Also, an important feature of Rubidium is its relatively broad D_2 transition with $\Gamma_0/(2\pi) = 6\,\mathrm{MHz}$, which leads to a minute influence of Doppler-broadening $k_\mathrm{B}\Delta\nu \approx 0.06\Gamma_0$ at the typical sample temperature of $T \sim 120\,\mu\mathrm{K}$.

As we will see throughout this thesis being able to get rid of thermal effects seems to be key to explore a new regime of light scattering. Figure 3.3 shows the D_2 transition of Rubidium 87 with its hyperfine and m_F states, all measurements shown in this thesis are performed using this transition.

3.5 Preparing Dense Atomic Samples

In order to prepare all atoms in the same hyperfine state, we first switch off the MOT repumping beam, which drives the $\left|5S_{1/2}, F = 1\right\rangle \leftrightarrow \left|5P_{3/2}, F = 2\right\rangle$ transition and then the MOT cooling beams, while having the macro-trap on. By doing so we gather all atoms in the lowest lying ground-state $\left|5S_{1/2}, F = 1\right\rangle$, which is a dark-state for the remaining cooling light. During this first step the density we are able to reach is limited by light assisted collisions of the near resonant MOT light. The preparation in the lowest ground-state is done to prevent hyperfine exchange collisions [40] while letting the sample thermalize in the dipole trap. Indeed, thermalization in $\left|5S_{1/2}, F = 2\right\rangle$ would lead to a higher loss rate for atoms in the trap, because the collision of two atoms could release the hyperfine ground state energy of $\mathrm{h} \times 6.8\,\mathrm{GHz}$ in the form of kinetic energy thus expelling both atoms from the trap whose depth U_0 does not

exceed h × 20 MHz. After about 100 milliseconds the micro-trap is switched on, and fills up from the reservoir provided by the macro-trap. The latter is switched off for the atoms of the micro-trap to thermalize again. The atoms are always probed on the $\left|5S_{1/2}, F = 2\right\rangle \leftrightarrow \left|5P_{3/2}, F = 3\right\rangle$ transition so to be able to probe this transition the atoms need to be repumped from $\left|5S_{1/2}, F = 1\right\rangle \rightarrow \left|5P_{3/2}, F = 2\right\rangle$. In order to prevent losses, repumping into $\left|5S_{1/2}, F = 2\right\rangle$ only takes place briefly before the measurement. At the end of this sequence up to 180 atoms are prepared in $\left|5S_{1/2}, F = 2\right\rangle$ [41].

3.6 Microscopic Traps and the Density of our Sample

With our aspherical lens we focus the far off resonant trapping beam down to 1.20(5) μm, such a low uncertainty of 5% is obtained by carefully calibrating the magnification of our imaging system. To obtain the magnification factor MA accurately we measured the angular displacement before and after the imaging system. The magnification is then given by: $\mathrm{MA} = \tan(\epsilon)/\tan(\epsilon_0)$, with ϵ_0 the angle between the optical axis and the laser-beam on the object side and ϵ the angle between the laser-beam and the optical axis on the image side. Knowing this allowed us to infer the focal spot size with an uncertainty of 50 nm.

The traps have a typical depth of $U_0 \approx k_\mathrm{B} \times 1\,\mathrm{mK}$ and the temperature of our atomic cloud of $\sim 120\,\mu$K, which is measured by the standard time of flight method [36]. We calculate the extent of our cloud at zero time of flight by following [42]:

$$a(P_0, T) = \sqrt{\frac{\mathrm{k_B} T}{4\pi^2\, m\, (\nu(P_0))^2}},$$

T the temperature of the cloud, P_0 the power of the trap beam, k_B the Boltzmann constant, m the mass of a Rubidium atom and $\nu(P_0)$ the trap frequency depending on the trap power. This model assumes that the sample is in thermal equilibrium to deduce the extent of the cloud, which for our sample is a fair assumption as we always let it thermalize before performing any measurements (see sec. 3.5). Another assumption is the harmonicity of our trap, which maybe questionable for the longitudinal dimension which has a Lorentzian profile. The calculated root-mean-square (RMS) size of this cloud is $(a_\perp, a_\mathrm{x}) = (0.2, 1.2)\mu$m. The transverse size of the cloud is well below the resolution limit of our imaging system working at 780 nm, and the estimate of the cloud density clearly has to rely on the accuracy of this calculation. The only quantity we can check experimentally is the transverse trapping frequency, which was measured

to be within 10% of the calculated value [33]. I repeated the measurement of the transverse trap frequency and confirmed the deviation of 10% by using a different method described in [43, 44].

The atom number on the other hand can directly be measured. We use a camera (PIXIS 1024) whose conversion between detected light and digital counts is extremely linear and an intensifier (Hamamatsu C9016-22), which increases the signal to noise ratio (SNR) to a level at which we are able to detect single photons. The linearity of the camera allows us to easily calibrate the CCD to the amount of light scattered by a single atom at infinite saturation and the high SNR makes it possible to measure atom numbers from one to a few thousands.

To obtain an accurate value for the amount of atoms inside the cloud we switch off the dipole trap to let the cloud expand. The density drops down to $\sim 10^{11}\,\mathrm{atoms\,cm^{-3}}$ where the atoms can be treated as independent scatterers. The expanded cloud is illuminated by a circularly polarized fluorescence probe beam with a saturation well above one, $\frac{2\Omega^2}{\Gamma^2} = \frac{I}{I_{\mathrm{sat}}} > 1$ with $I_{\mathrm{sat}} = 1.7\,\mathrm{mW\,cm^{-2}}$ and the collected light is measured with the previously calibrated camera, which allows to directly infer the number of atoms in the sample.

3.7 Measuring Transmission

To measure the transmission I performed an experiment during which the ambient magnetic field is compensated down to $|\mathbf{B}_{\mathrm{res}}| \approx 80\,\mathrm{mG}$. In order to measure the transmission of the sample we send top-hat pulses of a duration of about 300 ns and a rise time of $1 - 2\,\mathrm{ns}$ with a fibre-coupled Mach-Zehnder interferometer (typical pulse shown in figure 3.4a). Such steep slopes allow the observation of the transient and steady-state response of ^{87}Rb, which we record with a temporal resolution of 150 ps. It is crucial to make sure that the pulse intensity is $I \ll 0.1 \times I_{\mathrm{sat}}$, as failure to do so would not allow to compare the results to a classical dipole model, because quantum effects such as the saturation of the scattering rate and Rabi-oscillation have to be taken into account. While it is very important to perform many times the same experiment to get good statistics and increase the SNR, it is unnecessary to prepare an atomic sample for each measurement. This however is only possible with the advances of our control system to handle complex sequences (see chapter 2) which allow the interleaving of probe pulses with trapping pulses to keep the volume constant. The exact number of pulses in the burst-train is determined by checking that the transmission does not increase by more than 2% with respect to a single

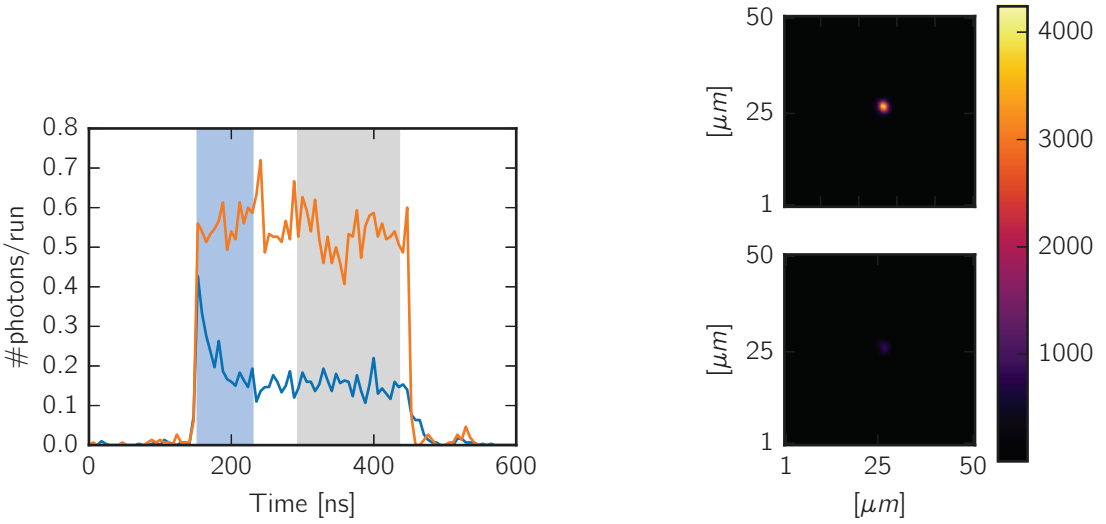

(a) The plot shows the number of photons per run versus the arrival time. The blue curve shows the atomic response and the orange curve shows the reference signal. The blue area indicates the time during which the medium gets polarized and the grey area indicates the time span that we defined as steady-state.

(b) The top plot shows in fake colour the spatial signal without atoms and the lower one the response with atoms. The colours are normalized to the case without atoms and the colourbar indicates ccd counts per run.

Figure 3.4.: The two different signals acquired during the measurement.

probe pulse. Staying within this limit I can send up to 1000 pulses per sample. The transient decay was fitted by $A\exp(-t/\tau)$ to see if the density has any influence of the decay time which for a single atom is $1/\Gamma_0 \approx 26\,\text{ns}$. Surprisingly I did not find any significant deviation from 26 ns for any atom number. As we are mainly interested in the steady-state behaviour a duration without any temporal evolution of the scattering response was chosen, which is shown as the grey area in figure 3.4a. The camera acquires a spatial signal which is not temporally resolved (figure 3.4b), but as we will see in the next section of this chapter, we can directly compare the two signals as the contribution of the transient is very minor. As all those measurements are performed close to the atomic resonance of the D_2 transition of ^{87}Rb they are repeated for various detunings $\Delta = \omega - \omega_0$, because the response of the system depends on the atomic polarizability

$$\alpha(\omega) = i\frac{6\pi/(\omega/c)^3}{1 - i(2\Delta/\Gamma)}, \tag{3.1}$$

which strongly depends on the exact frequency ω close to resonance.

3.7.1 The Signals

As we can obtain measurements from the APD and CCD for the same experiment we need to understand in detail what each of those two devices detect. The measured intensity I_{tot} consists of two interfering fields, the laser field $\mathbf{E}_{\text{L}}$ and the scattered field of the sample $\mathbf{E}_{\text{sc}}$: $I_{\text{tot}} = |\mathbf{E}|^2 = |\mathbf{E}_{\text{L}} + \mathbf{E}_{\text{sc}}|^2$. Due to the fact that the light reaching the APD is first coupled into a single-mode fibre the APD does not directly measure I_{tot}, but the field $\mathcal{E}$ which is a projection of $\mathbf{E}$ onto the fibre mode $\mathbf{g}$:

$$\mathcal{E} = \int \mathbf{E}(\mathbf{r}, \omega) \cdot \mathbf{g}^*(\mathbf{r}) \, \mathrm{d}S, \tag{3.2}$$

where $\mathrm{d}S$ denotes a differential area element perpendicular to the optical axis. As we are interested in the transmission, this measured signal is normalized by the field amplitude in the absence of atoms. The fibre connected to the APD is identical to the one the probe light is coming from so it can be assumed that $\mathbf{g} \propto \mathbf{E}_{\text{L}}$, which leads to:

$$\mathcal{S}(\omega) = \frac{\mathcal{E}(\omega)}{\mathcal{E}_{\text{L}}(\omega)} = \frac{\int \mathbf{E}(\mathbf{r}, \omega) \cdot \mathbf{E}_{\text{L}}^*(\mathbf{r}) \, \mathrm{d}S}{\int |\mathbf{E}_{\text{L}}(\mathbf{r})|^2 \, \mathrm{d}S}. \tag{3.3}$$

In comparison to the CCD which measures all incoming photons no matter in which spatial mode they are in:

$$|T(\omega)|^2 = \frac{\int |\mathbf{E}(\mathbf{r}, \omega)|^2 \, \mathrm{d}S}{\int |\mathbf{E}_{\text{L}}(\mathbf{r})|^2 \, \mathrm{d}S} \tag{3.4}$$

This means that whenever our sample distorts the incident light's spatial mode the transmission measured by the APD will be lower in amplitude than on the CCD, $|\mathcal{S}(\omega)|^2 \leq |T(\omega)|^2$, for any given atom number.

3.7.2 The Results

If we now carry out the analysis for the temporal and spatial signal by normalizing the atomic response to the reference signal we obtain the figures 3.5 (a) and (b), respectively. Following [17] the measured data is fitted by:

$$|\mathcal{S}(\omega)|^2 = |1 - \frac{A}{1 - 2i\frac{\omega - \omega_{\text{c}}}{\Gamma_{\text{c}}}}|^2, \quad |T(\omega)|^2 = |1 - \frac{A'}{1 - 2i\frac{\omega - \omega'_{\text{c}}}{\Gamma'_{\text{c}}}}|^2, \tag{3.5}$$

by assuming a Lorentzian line-shape and using the shift ω_c, the linewidth Γ_c and the amplitude A as free fit parameters.

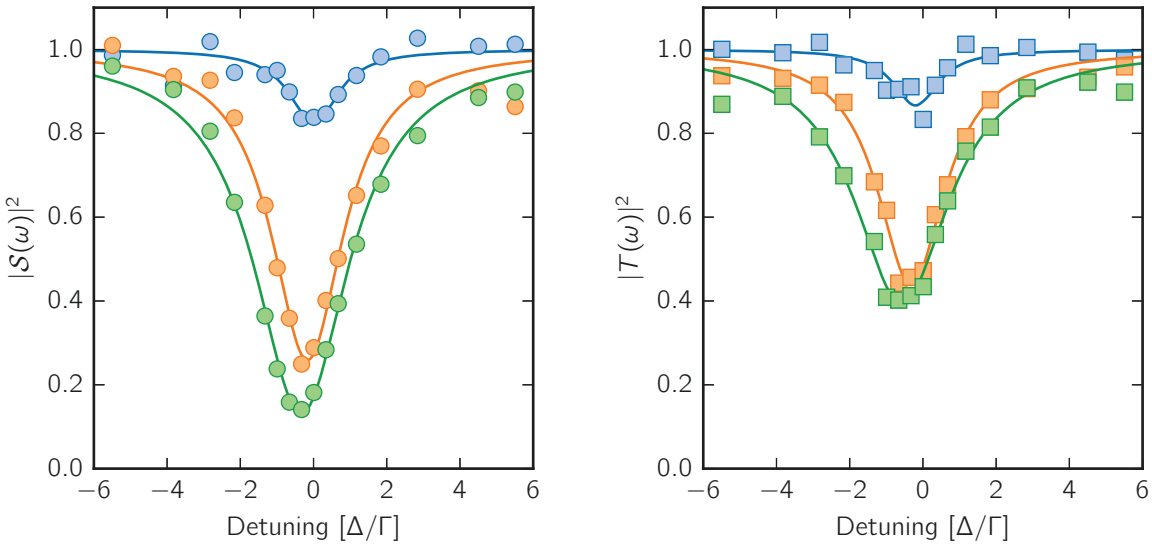

(a) Steady state frequency response measured by the APD.

(b) Transmission measured by the CCD.

Figure 3.5.: Comparison of the results acquired with the APD and CCD. The data points are obtained by measurement and the solid lines are fits by $F(\omega)$. The colors indicate different atom numbers: blue = 10, orange = 83, green = 180

To observe the density dependence of the scattering response I acquired seven spectra sampling the accessible range of atoms from $10 - 180$ on this experiment. As it is a difficult task to set a precise atom number for a measurement the span of atoms is not equally sampled, and the total acquisition time amounts to 30 hours, not taking the preparation time of the experimental sequence into account. From the fit of $\mathcal{S}(\omega)$ and $T(\omega)$ the amplitude $A(N)$, shift $\Delta_c(N)$ and linewidth $\Gamma_c(N)$ are extracted and shown in figure 3.6. The amplitude data was fitted with $A(N) = 1 - \sqrt{a + (1-a)\exp(-b\,N)}$ and the shift Δ_c and width Γ_c with a linear fit of type $f(N) = a + b\,N$, with a and b as free fit parameters. The results for the fit parameters are shown in figure 3.6 on the right hand side next to the corresponding plot. As expected $A_{c,CCD}(N) < A_{c,APD}(N)$, which confirms the simple fact that the dipole radiation of an atom is not at all a TEM_{00} and couples less into the single-mode fibre of the APD than the reference beam. It is rather puzzling that after shifting $\Delta_{c,APD}$ so that for zero atoms there is zero shift, the result for $\Delta_{c,CCD}$ has the very same slope but a constant offset to the result of the CCD. No plausible explanation of this result has been proposed so far.

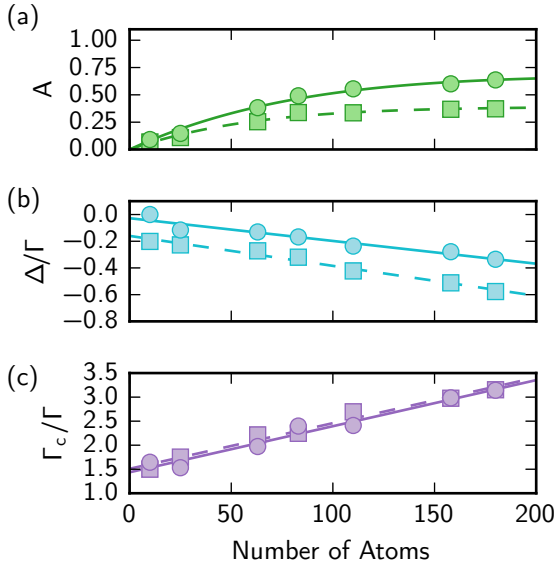

	a	±a	b	±b
APD	0.10	0.02	0.02	0.002
CCD	0.37	0.03	0.02	0.003

	a	±a	b	±b
APD	-0.03	0.02	-0.002	0.0002
CCD	-0.2	0.02	-0.002	0.0002

	a	±a	b	±b
APD	1.4	0.09	0.01	0.0009
CCD	1.5	0.08	0.009	0.0007

Figure 3.6.: Plots of the data points together with the fitted function on the **left**, on the **right** tables with the according fit parameters. In all three plots circles refer to the APD data and squares to the CCD data, the solid and dashed lines are fits, respectively. **(a)** shows the amplitude parameter of the fit function F, **(b)** shows the shift of the central $\Delta_c = \omega_c - \omega_0$, **(c)** Full width at half maximum Γ_c

3.8 Theoretical Models

As described in the introduction of this chapter, these measurements were performed to bridge the gap between two theoretical models that were used in prior experiments: a microscopic theory [25] and the other one a macroscopic theory [45].

A microscopic scattering model requires to have the individual knowledge about each constituent of the bulk sample. This means that we have to know the dipole-moment d of each particle. Knowing all of them allows us to calculate the scattering properties for the full sample by interfering their scattered field with the laser field.

On the contrary a macroscopic model assigns one parameter to the bulk sample, namely the susceptibility χ and only this one quantity is needed to describe the scattering. By restricting the probe beam intensity well below saturation, a classical description of the dipoles is sufficient as there is maximally one excitation in the sample. This allows us to ignore quantum effects such as saturating the transition [46].

In the following subsections I will first introduce the concept of a microscopic theory and how I implemented it. I will then outline the textbook derivation of the macroscopic model to clarify its domain of application. As a last step I will compare

the two theories and explain their differences on a qualitative level.

3.8.1 Microscopic Theory

As we are taking the viewpoint of a microscopic model our goal is to be able to calculate the dipole-moment d of each atom in the sample, which in turn allows us to calculate the scattering pattern of the full sample. Illuminating our atomic cloud with low intensity light $\frac{I}{I_{\text{sat}}} \ll 0.1$ we can consider the atoms to be classical dipoles, which respond linearly to the driving field. The induced dipole moment d is given by

$$\mathbf{d} = \alpha\, \epsilon_0\, \mathbf{E}_{\text{driving}}, \tag{3.6}$$

where α is the atomic polarizability of an individual scatterer, $\mathbf{E}_{\text{driving}}$ is the field which drives the dipole transition and ϵ_0 is the vacuum permittivity. For the simple case of a dilute medium the driving field is equivalent to the incident field, which for us would just be the probe laser. When the medium becomes denser, the effect of the medium as part of the driving field can no longer be neglected, and the latter is thus the sum of the laser field and all fields re-radiated by all other scatterers to the position of the jth scatterer:

$$\mathbf{E}_{\text{driving}} = \mathbf{E}_{\text{laser}} + \sum_{j \neq l} \mathbf{E}_{j \to l} \tag{3.7}$$

The interaction between two such dipoles is described with $V_{dd} = -\frac{1}{2}\mathbf{d'}_1 \cdot \mathbf{E}^*_{\text{d}_2}$ and the resulting interaction potential is according to [47]:

$$V_{\text{dd}} = -\frac{3\hbar\Gamma}{4} e^{ikr} \left[\left(\frac{1}{(kr)^3} - \frac{i}{(kr)^2} \right) (3\cos^2\theta - 1) + \frac{\sin^2\theta}{kr} \right] \tag{3.8}$$

In steady-state this leads to a set of coupled equations, the so-called coupled-dipole equation:

$$(\Delta + i\frac{\Gamma}{2})\mathbf{d}_j = \Omega + \sum_{l \neq j} [\mathbf{V}_{lj}]\, \mathbf{d}_l, \tag{3.9}$$

with Ω the Rabi-frequency and Γ the linewidth, l and j refer to the lth and jth dipole so that the matrix $\mathbf{V}_{lj}$ expresses the interaction between all pairs of dipoles.

So far this model would be correct for a two-level system, but due to the fact that the atoms are not prepared in a pure m_j state the full manifold of the $\left|5S_{1/2}, F = 2\right\rangle \leftrightarrow$

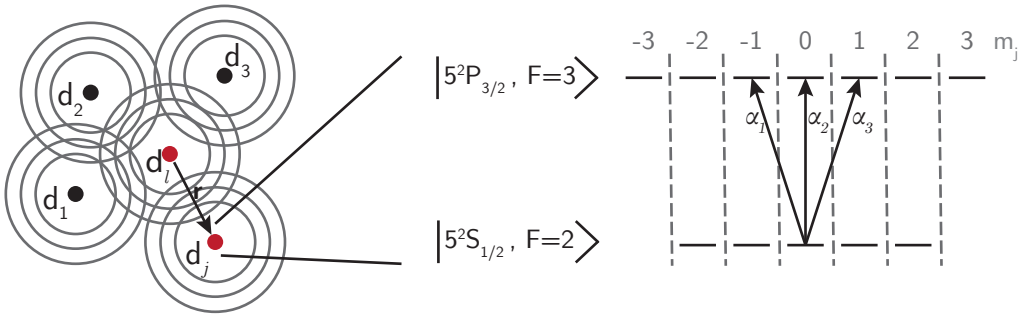

Figure 3.7.: Illustration of the microscopic theory.

$\left|5P_{3/2}, F=3\right\rangle$ transition has to be taken into account (figure 3.7). Each transition has to be weighted with its according Clebsch-Gordan coefficient, which depends on the polarization which couples the two m_j states. With the help of our collaborators from Southampton we included the effect of the internal structure [25]:

$$(\Delta + i\Gamma/2)\boldsymbol{\mathcal{P}}_{j\alpha} = \boldsymbol{\Omega}_{j\alpha} + \sum_{l\neq j}\sum_{\beta} \mathbf{C}^{(\beta)}_{m_l}\mathbf{C}^{(\alpha)}_{m_j}\mathbf{V}^{l\beta}_{j\alpha}(\mathbf{r})\boldsymbol{\mathcal{P}}_{l\beta}. \tag{3.10}$$

We substituted $\mathbf{d}_j$ in equation (3.9) by $\mathbf{d}_\mathrm{j} = \mathcal{D}\sum_\sigma \hat{\mathbf{e}}_\sigma \mathbf{C}^{(\sigma)}_{\mathrm{m_j}}\boldsymbol{\mathcal{P}}_{\mathrm{j}\sigma}$, where $\sigma = \pm 1, 0$ respectively α, β denotes the polarization of the transition. This relates the amplitude of the induced dipole moment of the jth atom from state $|g, m_\mathrm{j}\rangle \rightarrow |e, m_\mathrm{j}+\sigma\rangle$, $\mathcal{D}$ being the reduced dipole matrix element, $\mathcal{P}_{\mathrm{j}\sigma}$ the atomic coherence and $C^{(\sigma)}_{\mathrm{m_j}}$ the according Clebsch-Gordan coefficient. An illustration of this 12-level model is given in figure 3.7. In this model we consider each atom as a anisotropic classical dipole, thereby neglecting any optical pumping effects as well as Raman scattering and restricting each dipole to a manifold of one ground state and three excited states, this assumption should be true for $I \rightarrow 0$. As this model now is fully vectorial in terms of the light field the simple expression (3.8) for V_dd has to be generalized, which leads to:

$$\mathbf{V}^{l\beta}_{\mathrm{j}\alpha} = -\frac{3\hbar\Gamma}{4(kr)^3}\left[p_{\alpha\beta}(ikr-1) + q_{\alpha\beta}(kr)^2\right]e^{ikr}, \tag{3.11}$$

with $p_{\alpha\beta} = \delta_{\alpha\beta} - 3(\hat{\mathbf{e}}^*_\alpha \cdot \hat{\mathbf{r}})(\hat{\mathbf{e}}_\beta \cdot \hat{\mathbf{r}})$ and $q_{\alpha\beta} = \delta_{\alpha\beta} - (\hat{\mathbf{e}}^*_\alpha \cdot \hat{\mathbf{r}})(\hat{\mathbf{e}}_\beta \cdot \hat{\mathbf{r}})$, where $\hat{\mathbf{r}}$ is the interatomic separation vector between two scatterers and $\hat{\mathbf{e}}_\sigma$ is the unit polarization vector.

Implementation

I developed a Matlab code to simulate the interaction between light and atoms using the theoretical description shown above. In order to evaluate the influence of the model on the outcome, I will show a comparison between the simulation of a 2-level system and a more realistic 12-level system.

In a first step we fix the number of atoms and pick their positions from a 3D normal distribution, the position picking is repeated typically a hundred times, to provide a statistically meaningful sampling of the cloud. For the 12-level system we also randomly pick the initial m_j state of the jth dipole, which fixes the transition strength. The statistical distribution of the initial state depends on how our experimental sample is prepared, and for now we pick from a uniform distribution, meaning that all m_j states have the same likelihood of occurrence. We then calculate the interaction potential for a fixed position and m_j set then solve the linear equation system for a chosen detuning. The solution yields $\mathbf{d}_j$ or $\mathcal{P}_{j\alpha}$, which we then use to propagate the scattered light to our detector and interfere it with the laser light. The laser field is described by a paraxial beam approximation. Then we repeat the solving of this interaction potential for all the other detunings we are interested in, pick new positions and repeat the full sequence until all detunings have been calculated for all 100 position sets. My code for this simulation is available online[1]. The typical runtime of such a simulation for 200 atoms and a spectrum spanning over roughly 12Γ with a sampling of 0.1Γ takes less than 10 minutes on a quadcore-i5 Intel desktop computer.

Special care was taken when we interfered the laser field with the sum of the scattered field on the detector, because due to the high numerical aperture used on our experiment of NA $= 0.5$ we are on the edge of what can be described by the paraxial beam approximation[37]. We checked our numerical results for the case of a single atom pinned to the origin (focal spot) of the laser field and observed an asymmetry in the calculated spectrum which came from numerical errors in the calculation of the relative phase between the scattered light of the atom and the driving field. To compensate for this effect we changed the expression for the Gaussian beam in the far field to:

$$E_{\mathrm{LaserFar}}(\rho, z) = \frac{E_0}{w(z)} e^{-\rho^2/w(z)^2}\, e^{i(k\sqrt{z^2+\rho^2}-\pi/2)}, \tag{3.12}$$

with $w(z)$ the beam width at position z. The substitution exchanges the phase factor e^{ikz} by $e^{ik\sqrt{z^2+\rho^2}}$ to take into account that for high numerical aperture the wavefront is still curved and not flat.

[1] http://github.com/sjennewein/CoupledDipoles

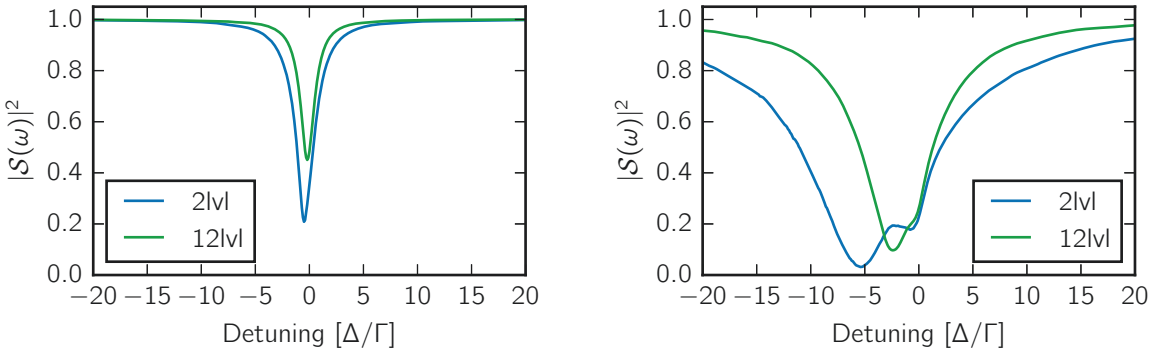

(a) 20 atoms **(b)** 200 atoms

Figure 3.8.: Comparison between the response of an ensemble made out of 2 level or 12 level atoms (Microscopic theory)

3.8.2 Macroscopic Theory

This approach now relies on the expression of the bulk dielectric constant of the material ϵ, and how it is related to the atomic polarizability α [45]:

$$\epsilon(\omega) = 1 + \rho\alpha(\omega), \tag{3.13}$$

with ρ the density. α is a microscopic quantity as it can be evaluated for each individual atom in the medium, whereas the dielectric constant is a bulk property of the whole medium. The equation (3.13) only describes dilute media and it was shown that for dense media a correction term has to be introduced. As in the previous chapter the question is how do all the other atoms in the medium affect the local response in a part of the medium. An interesting and elegant approach can be found in [27], and goes as follows: take a piece of dielectric medium and polarize it. Then freeze the polarization and cut out a sphere of the middle of the sample, which leads to a hole and a sphere. Due to the superposition principle of electrodynamics the total field should be $E_{\text{tot}} = E_{\text{hole}} + E_{\text{sphere}}$. The field of a uniformly polarized sphere amounts to $E_{\text{sphere}} = -\frac{P}{3\epsilon_0}$ and therefore $E_{\text{hole}} = E_{\text{tot}} + \frac{P}{3\epsilon_0}$. In any dense medium the field experienced by an atom placed at the position of the hole is therefore E_{hole}, because the neighbouring scatterers are so close that their radiated field will influence other scatterers locally. This is the reason why this correction is called **the local field correction**. This correction leads to a new relation between the atomic polarizability

and the susceptibility, which for dense media looks like:

$$\chi = \epsilon - 1 = \frac{\rho\alpha}{1 - (\rho\alpha/3)} \tag{3.14}$$

This new relation is called the Clausius-Mosotti or Lorentz-Lorenz equation. It describes very well the scattering properties of dense thermal vapours as shown by the Adams' group [26] and is the only feasible approach for large atom number.

Implementation

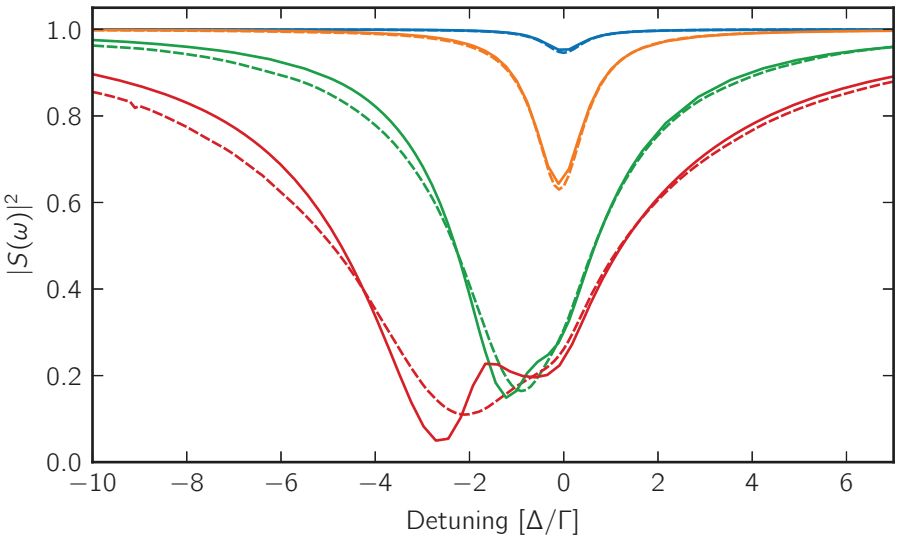

Figure 3.9.: Comparison between the 12-level system of the microscopic theory (dashed line) and the macroscopic theory (solid lines). The different colours indicate the atom number in the sample: blue = 1, orange = 10, green = 83, red any= 180

The concrete implementation for this theory framework was done by one of our collaborators Mondher Besbes from the group of Jean-Jacques Greffet. They developed a finite element Maxwell-solver, which allows them to simulate any geometry in a continuous media approach. In our concrete case they used $\alpha(\omega) = i\frac{7}{15}\frac{6\pi}{k^3}\frac{1}{1-i(2\Delta/\Gamma)}$, with $\frac{7}{15} = \sum_{j=-2}^{2}\sum_{l=-1}^{1}\mathcal{C}_l^j$, which is the polarizability of a single rubidium 87 atom taking the internal structure into account, by assuming equal population in the m_j states of the $\left|5S_{1/2}, F = 2\right\rangle$ and calculating the average polarizability [48]. The cloud geometry is then parametrized with the RMS width from the experiment and the inhomogeneous density is taken into account by $\rho(\mathbf{r})$. This leads to $\chi(\mathbf{r}, \omega)$ with which the electric field scattered in the far field by the cloud illuminated by the Gaussian laser beam is

calculated. Finally we compare the result of this theory with the twelve level result from the microscopic theory in figure 3.9. As can be seen for low atom number (density) the two theories are very similar, but when the atom number is increased the two theories start deviating from one another. The macroscopic theory clearly shows a bimodal distribution whereas the microscopic does not and rather broadens faster.

3.8.3 Discrepancy

Figure 3.9 shows a comparison between the results yielded by the two theories. It is quite clear that the larger the density, the larger the discrepancy. This may come as a surprise, but it was shown [20, 21, 49–52] that certain scattering terms which are included in the microscopic description are neglected in the macroscopic approach. Despite the fact that the macroscopic theory does not take all scattering events into account it has produced excellent results in the past for gaseous media [27, 45, 53], while being easier and faster to use than the microscopic approach.

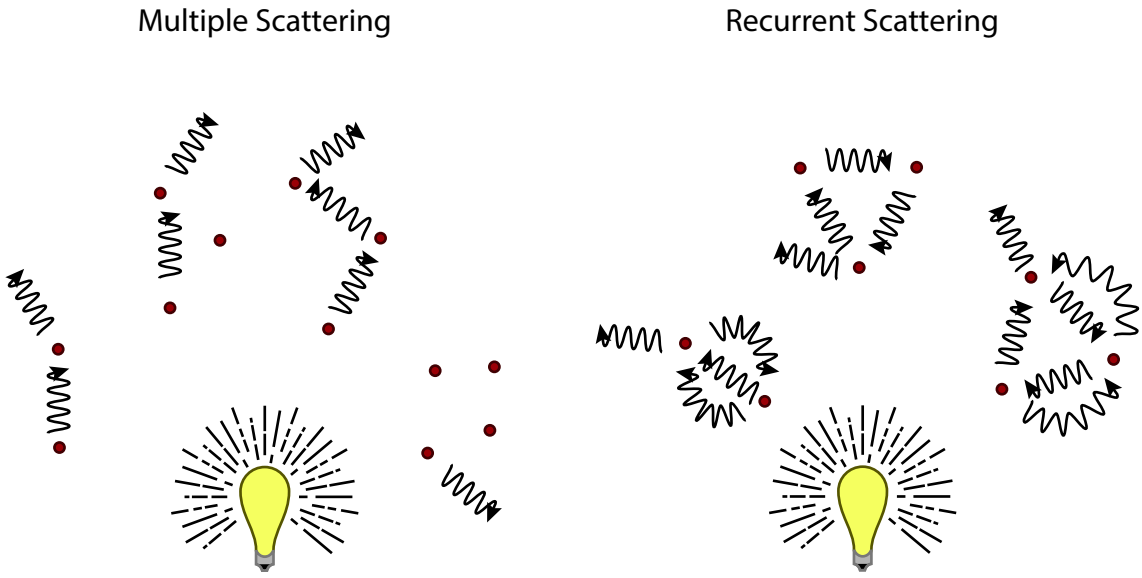

Figure 3.10.: Illustration of multiple and recurrent scattering events.

I will give now a qualitative understanding of what causes the discrepancy between the two theories, but for more detailed reads I advice the documents cited above. The difference between those two theories can be better understood when we categorize the type of scattering events that can happen into two groups, namely *multiple scattering* and *recurrent scattering*. Multiple scattering [16, 50, 54, 55] is characterized by the

fact that each scatterer in the sample is at most involved in one scattering process. In contrast recurrent scattering [51, 56] means that the scatterers involved participate more than once to the scattering process (illustration on figure 3.10). Those two groups have a wildly different scaling behaviour: *multiple scattering* can simply be increased by increasing the medium size. As a wave is travelling through the larger object it has to pass more dipoles which increases the likelihood for scattering events. However this would not increase the number of events that contribute to *recurrent scattering* for a sample made out of identical particles with polarizability α this type of scattering scales as the number of pairs of atoms $(\rho\alpha)^2$ in the volume of size α. This contribution only becomes important as $\rho\alpha \sim 1$ and it has been shown that these scattering events are ignored in the macroscopic theory. The exact contribution of recurrent scattering has been studied in great detail in [21, 50, 57–59] and it has been shown that in the presence of recurrent scattering and density approaching $\rho/k^3 \lesssim 1$ the susceptibility $\chi(\omega)$ becomes

$$\chi(\omega) = \frac{\rho\alpha(\omega)}{1 - \rho\alpha(\omega)(\frac{1}{3} + \beta(\omega))}, \tag{3.15}$$

where $\beta(\omega)$ is the term coming from recurrent scattering.

Introducing any sort of inhomogeneous broadening as for example the Doppler effect in hot vapour cells [26] the resonant frequencies of the j-dipoles are spread over a frequency range of $\Delta\omega_{\mathrm{D}}$ thus reducing the average dipole moment and thereby reducing β by a factor $\Gamma/(\Gamma + \omega_{\mathrm{D}})$ [49]. This explains why the classical Lorentz-Lorenz formula describes all cases where inhomogeneous broadening is dominant so well.

3.9 Theory versus Experiment

The comparison in figure 3.11 shows clearly that neither the macroscopic simulations, as expected from the discussions before, nor the microscopic simulations quantitatively describe our experiment. Qualitatively the increase and the plateauing of the amplitude are described by the two theories, the absolute value never matches the experiment. Also the two theories show the emergence of a second resonance, which is most likely due to the shape of our sample. In appendix A the response of such an atomic cloud is shown changing from an ellipsoid with an aspect ratio of 1:6 to a sphere. One of the shapes that does not influence the response and for which a simple analytic formula can be derived is a slab geometry, but for our apparatus it was not feasible to change to this geometry. Surprisingly enough this shape-dependent resonance never shows up in the actual measurements as the data is well described by a single Lorentzian

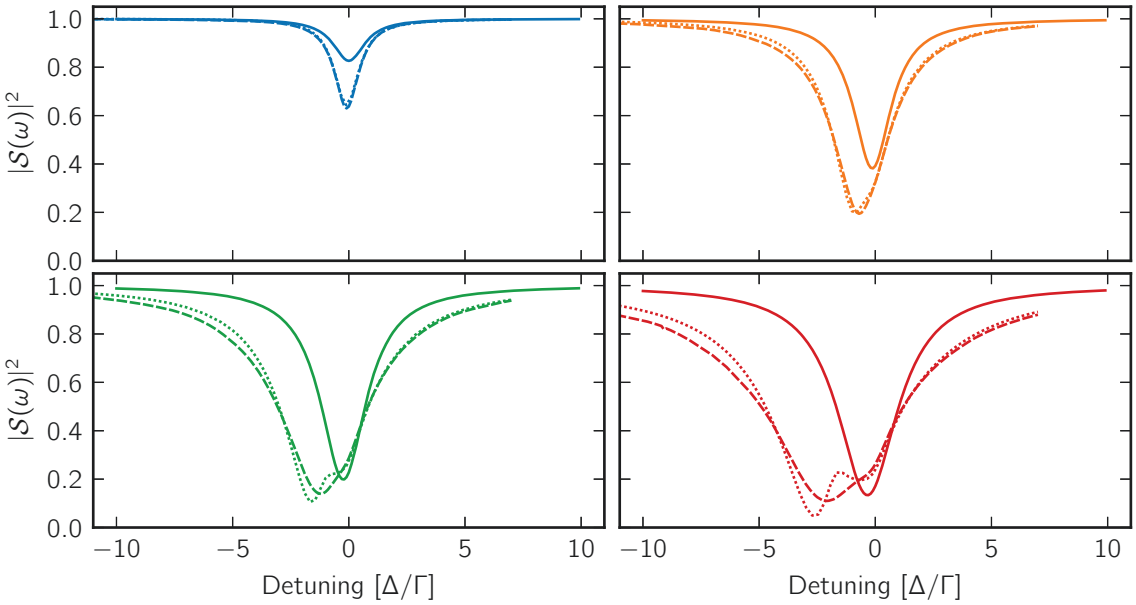

Figure 3.11.: Comparison of the macroscopic model (dotted line), microscopic twelve level theory (dashed line) and the fit result of the data (solid line). The different colours indicate the atom number: blue = 10, orange = 63, green = 110, red = 180

function.

The emergence of a second peak makes the comparison in linewidth and shift of the peak(s) between experiment and theory difficult. Figure 3.12 shows a comparison of the variation of the linewidth, shift [60, 61] and amplitude as a function of the atom number. To be able to compare the similarities and differences more quantitatively local maxima are extracted numerically from the simulated curve to track the two peaks. The width was estimated from the FWHM taken with respect to the global maximum and plotted versus the atom number in figure 3.12. The kinks of the line corresponding to the macroscopic theory result from the finite sampling of the simulation. The FWHM curve below one for low atom numbers is also a result of the finite sampling. These diagrams illustrate nicely that the overall trends are reproduced in the sense that all slopes have the same sign but in quantitative terms the theories do not match the experiment.

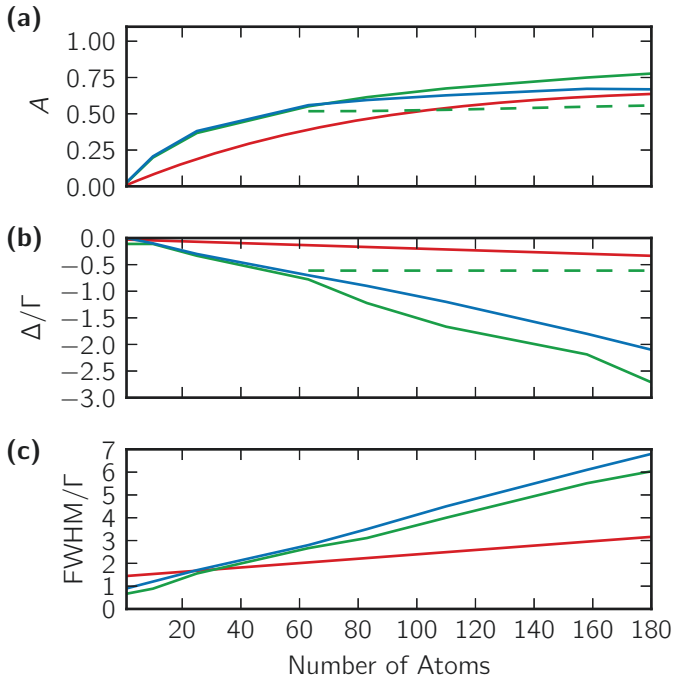

Figure 3.12.: Shows the comparison between the experimental data fit (red), 12-level microscopic theory (blue), macroscopic theory (green), the dashed line visualizes the emergence of the second peak in the macroscopic theory. (a) Amplitude, (b) shift of peak, (c) Full width at half maximum

3.10 Remaining Unknowns

When an experiment is not at all described by the well established existing theory it is obvious to ask oneself what could have gone wrong. Several candidates for the discrepancies may be found:

- Aligning a probe beam on to an atomic cloud, which is smaller than the wavelength in its transverse extended is a hard task. Could some frequency shift be introduced by misalignment?
- Obtaining the cloud size relies solely on a calculation under certain assumptions, how much can we trust this value?
- None of the models used to describe the atomic response take motional effects into account. How much does the finite temperature and the force introduced by the dipole-dipole interaction skew the result?
- Modelling the full internal structure of Rubidium 87 is very challenging, we did

our best to take all terms into account. Have we missed something?

The first point of this list will be clarified in the next section, the second and third point will be discussed in the conclusion chapter 6 and for the solution of the internal structure of Rubidium 87 see chapter 5.

3.11 Imperfect Alignment of the Microscopic Sample with respect to the Probe Laser

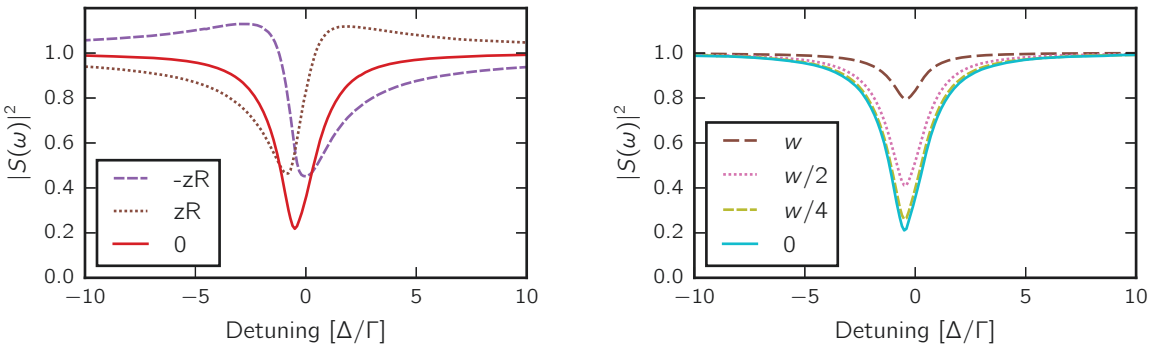

(a) Longitudinal displacement of the atomic sample with respect to the focal plane of the probe beam.

(b) Transverse displacement of the atomic cloud with respect to the center of the probe beam.

Figure 3.13.: Checking the influence of imperfect probe beam alignment

As the focal spot size of the probe is only $1.20(5)\,\mu$m and the cloud size $(a_\perp, a_z) = (0.2, 1.2)\mu$m it is not a trivial task to align the probe beam so that the cloud is exactly in the focal plane and the probe beam hits the cloud right on axis. I simulated the longitudinal and transverse displacement of the cloud with respect to the focal plane of the lens (L2) to get some insight into the effect of misalignment on the response of the sample. In figure 3.13a the atomic sample was placed one Rayleigh range z_R before and after the focal plane as well as in the focal plane itself. The curves corresponding to the displaced sample show a strong asymmetry. This asymmetry can be explained by introducing an additional phase factor, which is coming from the Gouy phase [62] $\Psi(z_0)$ of the probe laser. This phase evolves as $\Psi(z_0) = -\arctan(z_0/z_\mathrm{R})$, z_R being the Rayleigh-range, which we add as a factor to the previous transfer function (3.5) leading to:

$$\mathcal{S}_\mathrm{Gouy}(\omega) = 1 - \frac{A}{1 - 2i\frac{\omega-\omega_\mathrm{c}}{\Gamma_\mathrm{c}}} e^{i\Psi(z_0)}. \tag{3.16}$$

This allows us to extract the acquired phase from the measurement and convert it to a displacement. Due to the fact that the fiber output coupler of the probe beam is mounted on a translation stage (figure 3.2) with micrometer precision we can directly compare the results from the fit to the measured displacement. For this reason the focal spot was moved manually by 3.6(5) μm and by fitting $S_{\text{Gouy}}(\omega)$ to a spectrum before and after the movement and extracting Δz_0 a displacement of 2.0(6) μm was confirmed. I also confirmed that this asymmetry is constant for all atom numbers as expected for a geometrical effect. If it had been a lensing effect of the atomic sample as claimed in [63] this effect would be atom-number dependent, which was not experimentally observed. Using the Gouy phase for alignment as well as interferometrically measuring the size of a nano object is a well established practice in the field of microscopy with nano-particles [64, 65]

In figure 3.13b the cloud was moved transversally to the probe beam in the simulation. This only results in a reduction of contrast, but no additional shift or change in linewidth can be observed, either. Clearly no alignment imperfection would introduce any additional shift or broadening of the observed spectra. The transverse misalignment decreasing the measured amplitude could have let to a constant offset in the observed amplitude.

3.12 Depolarization due to Multiple Scattering

As discussed in the introduction of this chapter the total scattered light of a sample is made out of a coherent and incoherent contribution, the macroscopic Maxwell equation can only be applied for the coherent scattering, which maintains the polarization of the incident field. In this section I investigate if our system is truly dominated by coherent scattering as the multiple scattering can depolarize the probe light [51, 66]. To measure the polarization state of the transmitted light I use the same scheme as described in section 3.7, but this time, keeping the number of atoms constant at 140 atoms and instead turn the half-waveplate in front of the polarizing beam splitter (figure 3.2) so to measure spectra for different linear polarizations. Fully polarized light follows Malus' law: $I = I_0 \cos^2\theta$, I_0 being the incident light power and θ the angle of the analyser. As for completely depolarized light $\frac{I}{I_0} = \frac{1}{2}$ because the light would be composed of a mixture of linear polarizations at all angles and the average value of $\sin^2\theta$ amounts to one half. Figure 3.14 shows the detected light by the APD for different analyzer angles with and without an atomic sample in the beam path, normalized to the maximum of the reference signal. The values shown for the atomic

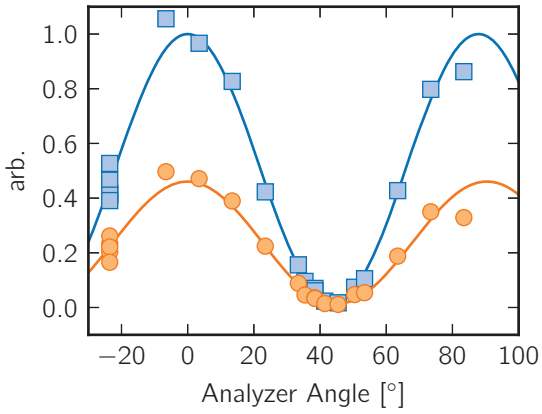

Figure 3.14.: Measured light versus analyzer angle. The zero is set to the case where polarizer and analyzer are parallel. The blue marker shows the reference without atoms and the orange marker the modification due to the presence of atoms, the solid lines are fits respectively.

signal are taken very close to resonance so to see the largest effect.

The contrast $C = \frac{x_{\max} - x_{\min}}{x_{\max} + x_{\min}}$ of those two curves is almost the same, for the reference curve I obtain $C_{\mathrm{ref}} = 0.97$ and for the signal with atoms $C_{\mathrm{atoms}} = 0.96$. Both measurement series are also very well fitted by Malus' law, these two facts indicate that no depolarization takes place for the light transmitted through the samples. Those spectra were taken while the sample was not perfectly placed in the focal plane, so they are fitted with equation (3.16) to account for the Gouy phase. The obtained fit parameter are plotted versus the analyzer angle in figure 3.15. The data shown was acquired over the course of several days and in random order so to avoid any systematic drifts, each day the spectrum at $-23°$ was taken again to serve as a reference. Overall no trend can be observed from the amplitude, peak shift or Gouy phase, but the linewidth, which shows a surprising dispersive behaviour at the analyzer position of 43°. This is the angle for which the analyzer is orthogonal to the probe light polarization as can be seen from figure 3.14. I checked numerically that the distortion related to the Gouy phase does not have any influence on the extracted linewidth on an experimentally relevant level of 10^{-3}. It can also be ruled out that it is an odd effect of the polarizing beam splitter, as no trace of modification can be found on the reference measurement. No plausible explanation of this result has been proposed so far.

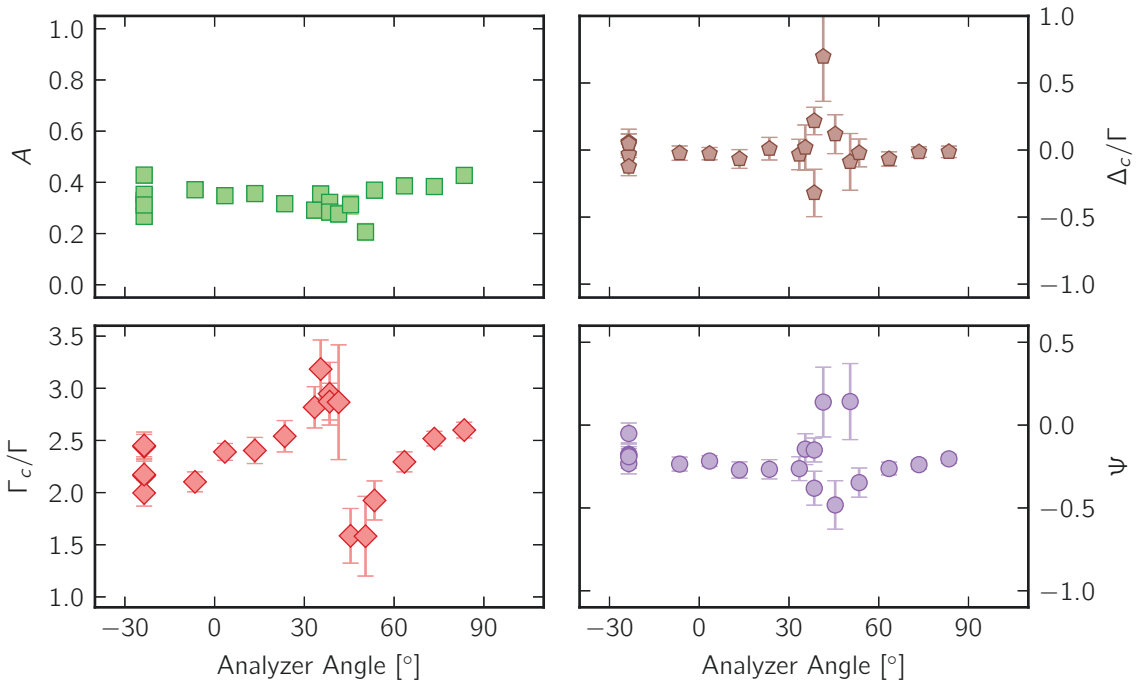

Figure 3.15.: Showing the four fit results plotted against the analyzer angle. Top left (green) amplitude, top right (brown) peak shift, bottom left (red) linewidth, bottom right (purple) Gouy phase

3.13 Conclusion

In this chapter we have seen the transmission behaviour of dense clouds of Rubidium 87 probed at $B = 80\,\mathrm{mG}$ without a m_F state preparation by a linearly polarized probe light close to resonance of the D_2 transition. Resulting from that are a saturating behaviour of the transmitted light amplitude as well as a very small line shift of up to 0.3Γ and a broadening of the linewidth of up to $\sim 3\Gamma$. The transmitted light has the same polarization as the incident beam and is not depolarized due to multiple scattering. The trends are reproduced by the available scattering theory but surprisingly the simulated values never match the experimental results.

We have also seen where the differences in the two applied theories lie and why any system with inhomogeneous broadening (e.g. hot vapour cells) is well described by a macroscopic model. The microscopic approach, most suited to our small cold atomic sample, in spite of its completeness, still seems to be insufficient to describe the scattering properties of cold dense samples.

Chapter 4

Acquired Phase by passing through a dense sample

As the transmission experiment described in the previous chapter is governed by interference between the probe light and the re-emitted light from the sample, it is key for the full understanding of this process to not only study the effect of scattering on the amplitude of the probe pulse, but also the phase shift that scattering induces. It is indeed the knowledge of both which permits a full description of the interference process.

I will show how the phase imprint of the cloud of atoms can be retrieved from a measurement of the group delay of a Gaussian shaped pulse I will then establish a self-consistent link with the previous chapter by describing my system by a linear transfer function.

4.1 Experimental Setup

The experimental setup required to measure the group delay from which the phase shift can be inferred is absolutely identical to that described in the previous chapter 3. In order to measure the group delay, an accurate definition of the pulse arrival time must be established. For this reason I exchanged the top-hat pulse by Gaussian shaped one, using a Gaussian pulse defines a peak which is used to accurately infer the arrival time. The width of the Gaussian pulse $I_{\mathrm{Gauss}}(t) = A\exp(-t^2/(2\sigma_{\mathrm{I}}^2))$ is $\sigma_{\mathrm{I}} = 25\,\mathrm{ns}$ and the peak intensity A was kept well below $0.1 \times I_{\mathrm{sat}}$. The measured signals are shown for two different detunings in figure 4.3.

4.2 Group Delay & Phase Shift

A common way to measure the phase imprint is by splitting the beam and passing one part through a medium and afterwards interfering the two beams to measure

the acquired relative phase shift [17, 67–69]. Achieving the interferometric stability required for such fine measurements is challenging. It is however possible to work around this constraint by establishing the relationship between phase shift and group delay.
For any dispersive medium [70]:

$$\tau(\omega) = \frac{d\phi}{d\omega}, \tag{4.1}$$

τ being the group delay, which can be measured easily provided the arrival time of the pulse is well defined. By propagating through a certain thickness of material the

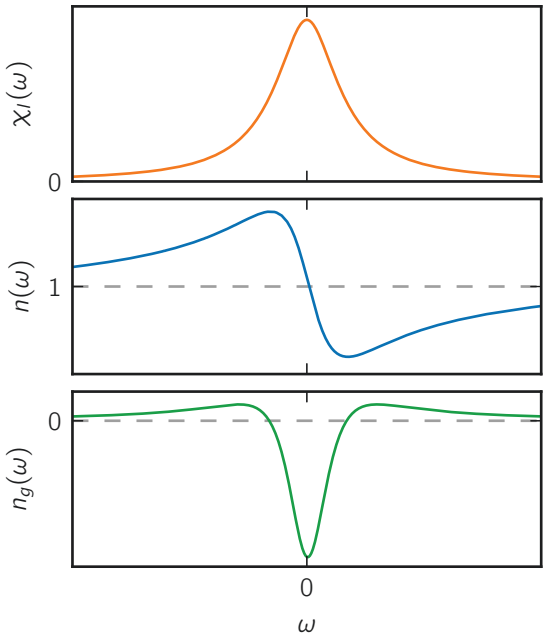

Figure 4.1.: Exemplaric illustration of refractive index n and the corresponding susceptibility χ_I and group index n_g of an absorptive medium.

measured group delay also gives access to the group velocity v_g:

$$v_\mathrm{g} = \frac{l}{\tau} = \frac{c}{n_\mathrm{g}(\omega)} = \frac{c}{n(\omega) + \omega\frac{dn(\omega)}{d\omega}}, \tag{4.2}$$

n_g the group index, l the thickness of the medium, ω the angular frequency and c the speed of light. (For this setup we have to be cautious with stating a velocity as the probed sample has an ellipsoidal shape and thus not a constant length l.)

Due to the fact that around a resonance the refractive index varies significantly with

frequency (see figure 4.1) it is possible that the group velocity is positive as well as negative [71–73]. Those two scenarios are called fast light $\tau < 0$ and slow light $\tau > 0$, the first one being a pulse advancement and the second a delay with respect to the vacuum case. One of the interesting questions to ask is now what can the maximal speed up or retardation be. In [31, 32, 74] two groups have derived a criterion for the maximum fraction pulse advance to be $\frac{\tau}{\Delta t} \leq 2$ with τ the advancement of the pulse and Δt the width of the pulse. They reach this conclusion by comparing the advancement of the pulse, which varies linearly in sample thickness with the absorption of the material. The absorption follows the Beer-Lambert law and is exponential with sample thickness. The exact reasoning to reach the value of 2 is quite intricate and is best understood by reading the cited papers.

4.3 Transfer Function

As the refractive index of a material is given by $n = \frac{c}{v}$ it only depends on the speed of light c and the phase velocity in the medium v and is therefore geometry independent. As we are working with a sample which has the shape of an ellipsoid it is not unlikely that the results are influenced by an unknown geometrical factor. For this reason we describe the sample by a linear transfer function $\mathcal{S}(\omega) = 1 - \frac{A}{1-2i\frac{\omega-\omega_c}{\Gamma_c}}$, which is *not* the refractive index for a slab:

$$E_{\text{out}}(t) = \frac{1}{2\pi} \int_{-\infty}^{\infty} \mathcal{S}(\omega) E_L(\omega) e^{-i\omega t} \mathrm{d}\omega, \tag{4.3}$$

with $\mathcal{S}(\omega)$ from (3.5) and the Fourier transform of the incoming laser field:

$$E_L(\omega) = \frac{\sigma_{\text{E}}}{\sqrt{1 + i\beta\sigma_{\text{E}}^2}} e^{-(\omega-\omega_L)^2\sigma_E^2/(2(1+2i\beta\sigma_E^2))}. \tag{4.4}$$

For the free fit parameters $A(N), \Delta_{\text{c,APD}}(N), \Gamma_{\text{c,APD}}(N)$ of $\mathcal{S}(\omega)$ and $\sigma_{\text{E}} = \sqrt{2}\sigma_{\text{I}}$ we use the functional forms from section 3.7.2 measured in steady-state. Conceptually the refractive index is a form of linear transfer function, but as stated before the refractive index is shape independent whereas in the transfer function used here the influence of the shape of the sample might be included.

As we will see in the measurements section, the dependence of the delay with detuning exhibits an asymmetric behaviour. Such *asymmetric* behaviour could be explained by a chirp of the probe pulse, which was confirmed by a piecewise measurement of

its instantaneous frequency. It was therefore necessary to introduce an additional parameter, β, which allowed to account for this chirp.

4.4 Measuring the Chirp

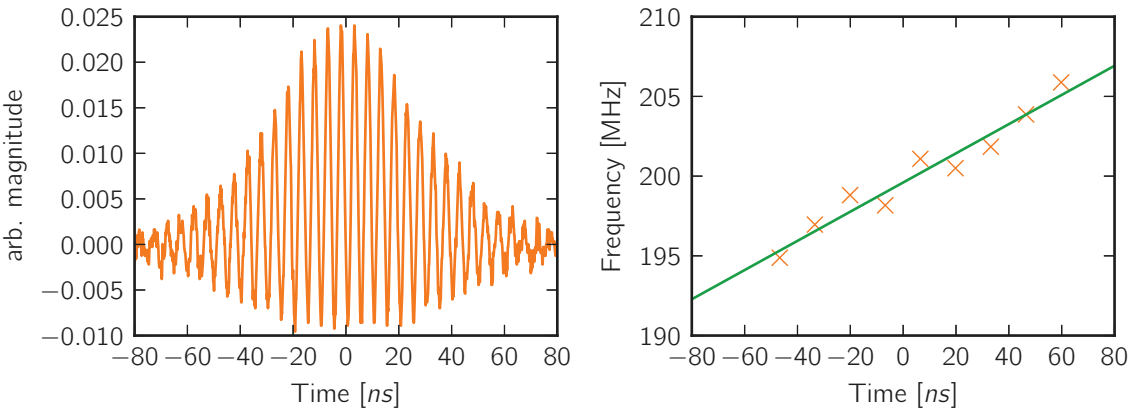

Figure 4.2.: The left plot shows the temporal interference signal of a pulse with a Gaussian envelope and a constant beam from the same laser source. On the right the orange crosses show the extracted local frequency corresponding to the pulse on the left. The green solid line is a linear fit to extract the slope of the frequency chirp.

For the pulse length of $\sigma_{\mathrm{I}} = 25\,\mathrm{ns}$ I measured a chirp of $\beta = 37\,\mathrm{kHz\,ns^{-1}}$ which integrated over the pulse length and compared to the carrier frequency of 200 MHz is an effect of $\sim 0.5\%$. To measure such a minute chirp I split the beam before the AOM, which modulates the Gaussian pulse on to the laser light and afterwards superimposed the two. The interfering light is guided to a fast photodiode with a bandwidth of $\sim 12\,\mathrm{GHz}$, the photodiode signal is recorded with a fast oscilloscope. To reliably extract the chirp I first fitted the pulse with the function

$$P(t) = y_0 + \alpha e^{-\frac{(t-t_0)^2}{2\sigma_p^2}} \sin(2\pi f t + \phi) + \beta e^{-\frac{(t-t_0)^2}{\sigma_p^2}} \tag{4.5}$$

to fix all parameters $(y_0, t_0, \sigma_p, \phi)$, but the frequency f for a second analysis run. Afterwards I split the pulse into ten time windows of equal length and fitted each of them with the function (4.5) fixing all free parameters to the values from the first run but the frequency, so as to extract the local frequency. A linear chirp is assumed and by fitting a linear function to the previous results the slope is extract, see figure 4.2. The extracted chirp with this method is $\beta = 37\,\mathrm{kHz\,ns^{-1}}$ for a pulse with $\sigma = 25\,\mathrm{ns}$.

As we will see in the following section this leads to a very good agreement between the model and the data. The chirp itself originates from the AOM driver, which was thought of being the only device in our group that is capable of handling such fast amplitude modulation, but as we have seen it does not properly. The bandwidth requirements for such an amplitude modulation are very hard to achieve as they range from tens of MHz to almost DC, as otherwise either the pulse is distorted or kinks in the wing of the Gaussian can be observed.

4.5 Measurement

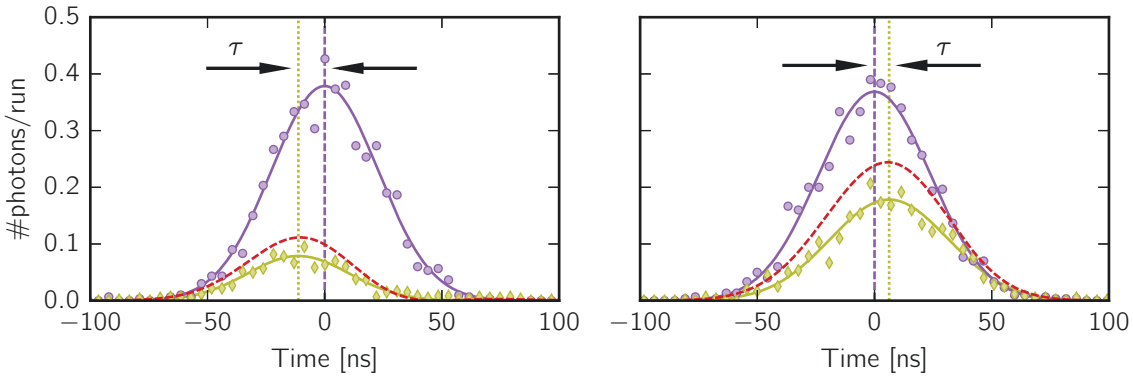

Figure 4.3.: Comparison between the Gaussian pulse with (yellow) and without atoms (purple), as well as the calculated one (red) using (4.3) for 170 atoms. On the left for $\Delta = -0.7\Gamma$ and on the right $\Delta = 1.8\Gamma$. The vertical dashed lines indicate the peak of the measured signal corresponding to their colour.

Figure 4.3 shows the measured Gaussian pulse for two detunings, illustrating the two phenomena of fast and slow light. What can be seen in this figure is that for two different detunings the response of the atomic cloud can arrive before or after the unperturbed signal on the detector. This seems as if signals could be sped up by passing through an atomic sample at a frequency close to resonance. It was shown many times that this is not the case as it would violate causality as we know it [75, 76]. This process should not be thought of as shrinking the original signal and moving it to the new position with a sample in place, but rather as cutting the new envelope out of the old one. Ultimately this process is limited by the time it takes to polarize dielectric matter, which is the cause of the delayed response. This directly shows that this effect of increase and decrease in velocity (we will focus on the increase as it is the only one

that conflicts with causality) directly comes together with a reduction in amplitude. In fact the quantity that matters to causality is the information velocity v_{info} which at all times has to be smaller than the speed of light. Whereas the quantity we are actually measuring is the group delay τ from which we infer the group velocity v_{g}. The group velocity in fact can take values smaller and larger than the speed of light [75, 77, 78]. So by cutting out the smaller envelope out of the envelope of the unperturbed signal also comes a loss of information, due to the fact that the new signal might be zero or close to zero in regions where the original pulse still has information encoded. It turns out to be sufficient to not break causality at any time as a retransmission would be needed, which decreases the information speed sufficiently to not conflict with causality.

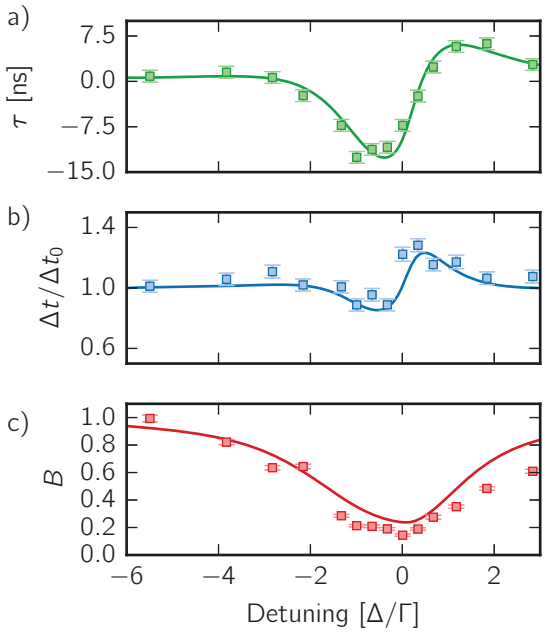

Figure 4.4.: Measurement results for 170 atoms: (a) shows the measured delay for various detunings (b) shows width change normalized to the incident pulse length (c) shows the magnitude. All solid lines are calculated without any free parameter using (4.3). **The asymmetry in the delay and width comes from the chirp in the probe light.**

In the experiments I measured these signals for 14 detunings and for a total of seven different numbers of atoms in the sample. Fitting the transmitted pulses by a Gaussian $G(t) = B\exp[-(t-\tau)^2/(2\Delta t^2)]$ and thereby extracting a set of parameters consisting of the amplitude B, the delay τ and the width Δt. In figure 4.4 I only show the result for one atom number the remaining results can be found in appendix B. The dashed red line on the same figure is calculated with equation (3.5) and the free

parameter in this equation are determined by the values obtained in chapter 3. As we can see this model fits very well the measured data and it is a fair assumption to fit the data in chapter 3 by a complex function. Using a complex function to fit a steady-state amplitude signal allows to extract the phase imprint, too, but might have been a bold assumption. I want to emphasize once more that the observed asymmetry in figure 4.4 is solely due to the imperfect probe light which is chirped in frequency.

As described before the thickness of the material divided by the group delay defines the group velocity v_g. In our case it would be awkward to talk about a thickness as the sample is ellipsoidal and thus does not have a fixed thickness. To circumvent this problem I am going to calculate the following parameters for a *fictive* slab of thickness $L = \sqrt{2\pi}L_z = 3\,\mu$m with $L_z = 1.2\,\mu$m the RMS size of the ellipsoid. The length L together with the delay $\tau = -10\,$ns leads to a velocity of $v_g = -300\,$m/s [79] and a group index of $|n_g| = 10^6$. Another way of looking at it is the pulse compression which is given by $1/|n_g|$. One of the $\sigma_I = 25\,$ns pulses has a length of $c \cdot \sigma_I = 7.5\,$m in vacuum but is compressed inside the medium down to $7.5\,\mu$m. This means that the atomic cloud does not fully store the pulse but rather acts as a very efficient delay line. The quantities stated so far have outstandingly high values and are neighbouring results that have been so far only achieved in electro-magnetically induced transparency situations [67].

With such remarkable delays of $-10\,$ns while still having 20% transmission the fractional advance amounts to $\tau/\Delta t \approx 0.4$. In the light of the findings of the group of Charles Adams [24], where Gaussian shaped light pulses are send through a hot atomic vapour, this comes as much of a surprise as they extrapolate from their measurement a fractional advancement of 0.55 at 1% transmission level. If we perform the same extrapolation (again for the imaginary slab of constant density) using the Beer-Lambert law to calculate how thick the sample needs to be to only have 1% transmission and then use this value to calculate the pulse advance, which is linear with sample thickness we obtain that for a sample of $6\,\mu$m a fractional pulse advancement of 2. The extrapolation using the Beer-Lambert law ($e^{-\chi'' kl}$) might be a bit dodgy as it is only valid for media which are dominated by single scattering events, which might not be the case here. But even if it would not reach 2, it is still the most promising system for testing such extreme pulse advancement.

4.6 Maximum phase and delay

By having shown that the transfer function approach describes our system very well we can deduce the largest phase imprint, which occurs for 180 atoms to be on the order of one radian (figure 4.5). The maximum group delay is obtained by deriving $\mathcal{S}(\omega)$ with respect to ω leading to:

$$\frac{\mathrm{d}\mathcal{S}}{\mathrm{d}\omega} = \tau_{\max}(N) = -\frac{2}{\Gamma_c(N)}\frac{A(N)}{1-A(N)}, \tag{4.6}$$

with $A(N)$ and Γ_c taken from the previous chapter. The calculated value (purple) shown in figure 4.5 indicates larger delays than what was measured experimentally. Having a finite pulse length of 25 ns leads to a certain frequency spread, which is not taken into account in the simple derivation (4.6). For this reason I simulated the pulse propagation for pulses of 200 ns (dashed yellow), which reduces the frequency spread of a pulse and leads to a very good agreement.

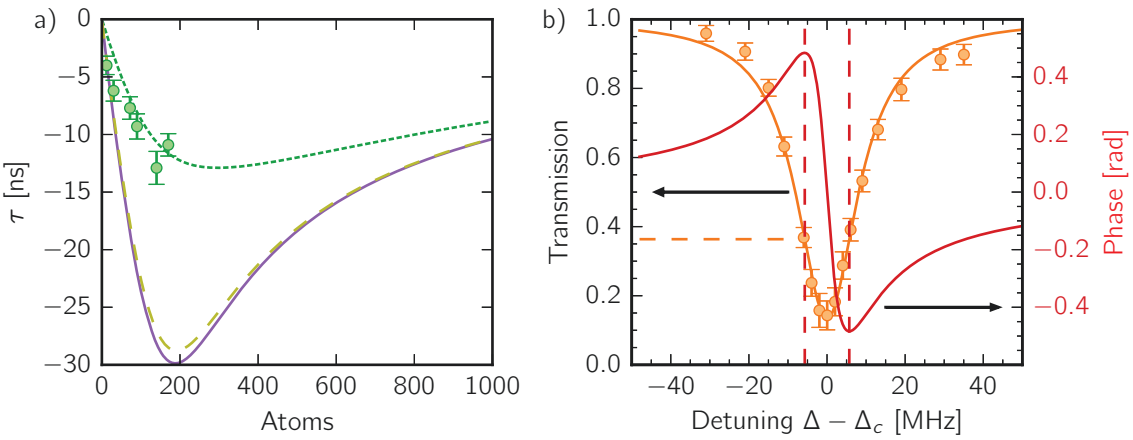

Figure 4.5.: (a) shows in green the measured maximum delay for several atom numbers, the green dashed line is numerically extracted from the theory for a pulse length of 25 ns. The solid purple line is calculated using (4.6) and the dashed yellow line is the simulation for a pulse length of 200 ns. (b) shows in orange the absorption measured for the largest number of atoms (180) and in red the corresponding phase

4.7 Conclusion

In this chapter we confirmed the results of chapter 3: despite the lack of an intrinsic model we can describe this microscopic cloud of atoms very well by a linear transfer function. Using this approach supports the use of a complex function for the steady-state response to extract the amplitude as well as the phase imprint of the system. With this transfer function it was possible to calculate theoretical curves without any further free parameter which are in very good agreement with the measurements. Despite the fact that this sample is smaller than the waist of the probe laser we have seen large pulse advancements $\sim -10\,\mathrm{ns}$ as well as delays $\sim 7\,\mathrm{ns}$ while having a fairly high transmission of $\sim 20\%$. The fractional pulse advance of 40% is also the largest measured so far and if it would be possible in our setup to scale the system up to $\sim 6\,\mu\mathrm{m}$ while keeping the density constant the fractional pulse advancement would go up to 2 which is approaching the theoretical limit Boyd and Macke [31, 74] have predicted.

Chapter 5

Rubidium as a 2 Level System

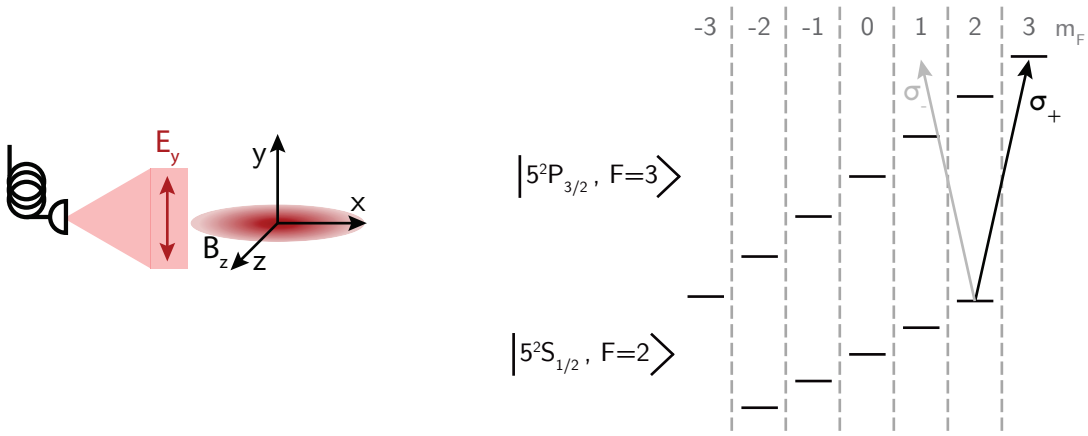

(a) Schematic of 2-level probing. The transmission probe light is linearly polarized along the y-axis and a strong homogeneous B-field is applied along the z-axis.

(b) Schematic of the lifted degeneracy for high B-field together with the probe light consisting of $\sigma_+ + \sigma_-$ light

Figure 5.1.: Core features of the 2-level measurement.

In chapter 3 we identified the internal structure of Rubidium as one of the possible sources of the discrepancy between theory and experiment. In order to rule it out it was important to repeat the same experiments, but this time starting from atoms in a pure m_F state and lifting the degeneracy so that we have a pure 2-level system (see figure 5.1b).

Optical pumping in dense samples is often thought to be hard to achieve due to the screening effects that such systems may exhibit. In dense samples the amount of rescattered light cannot be neglected, thus the exact polarization with which a second atom in the sample experiences depends strongly on the relative position. This is thought to be the process which prevents efficient pumping in a dense sample [80]. As we will see here it is nevertheless possible to spin polarize our sample while being dense ($\sim 10^{14}\,\mathrm{atoms\,cm^{-3}}$).

In the course of this chapter I shall present the results of the experiments that I performed and compare the behaviour of our dense sample with (chapter 3) and without internal structure, as well as with the available coupled dipole model. The case of low saturation driving of our spin polarized sample proves especially interesting as we are even able to consistently link the temporal behaviour with the steady-state results indicating the influence of the interaction on the dynamics. In addition I also performed measurements for higher probe light intensities as well as measurements of I_{sat} for various densities. All results of this chapter are still preliminary and are not published, yet.

5.1 Preparation in the extreme Zeeman state

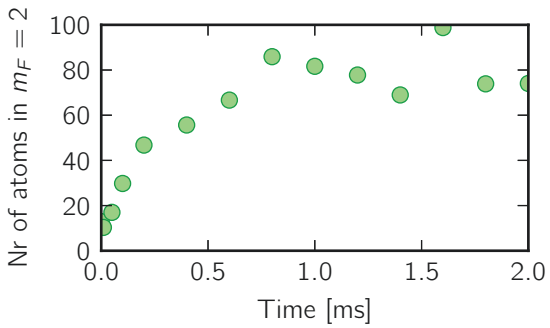

Figure 5.2.: Preparation of the extreme m_F state at different pumping durations starting from 100 atoms in the $\left|5S_{1/2}, F = 2\right\rangle$ manifold.

The density of the atomic samples that we are studying in the scope of this thesis is on the order of 10^{13} to $10^{14}\,\mathrm{atoms\,cm^{-3}}$. With atoms in such close proximity optical pumping was thought to be a very difficult task. Indeed, light scattered by a first atom is very likely to be rescattered by another atom. As the relative position of the two atoms determines which polarization is experienced by the second one, the effectiveness of optical pumping is bound to be limited. For example light which was initially σ_+ polarized might turn into σ_- polarization, which would lead to an unwanted change in m_F state and thus hinder the pumping process.

In the end the solution was reasonably straightforward by using a repumper $\left|5S_{1/2}, F = 1\right\rangle \rightarrow \left|5S_{1/2}, F = 2\right\rangle$ and a pumper $\left|5S_{1/2}, F = 2\right\rangle \rightarrow \left|5P_{3/2}, F = 2\right\rangle$ which are both σ_+ polarized, while slowly ramping up a magnetic field along the z-axis. In detail I first ramped up a small B-field along the z-axis of $\sim 2 - 5\,\mathrm{G}$ then

I shone in a repumper $|5S_{1/2}, F = 1\rangle \rightarrow |5S_{1/2}, F = 2\rangle$ ($\sim$ 1 ms) and a pumper $|5S_{1/2}, F = 2\rangle \rightarrow |5P_{3/2}, F = 2\rangle$ with σ_+ polarization. At the end of the pumping period I quickly ramped up the magnetic field ($\sim$ 10 ms) so to lift the degeneracy and isolate the extreme m_F state from the rest. After 1 ms of this pumping scheme 80 out of 100 atoms are prepared in the extreme m_F corresponding to a density of $\sim 10^{13}$ atoms cm^{-3} (see figure 5.2). Another effect of this preparation scheme is that the final temperature of the sample goes up from 120 μK to 160 μK which is most likely due to the proximity of the centre frequency of the pumping light with the atomic resonance, which introduces a source of heating.

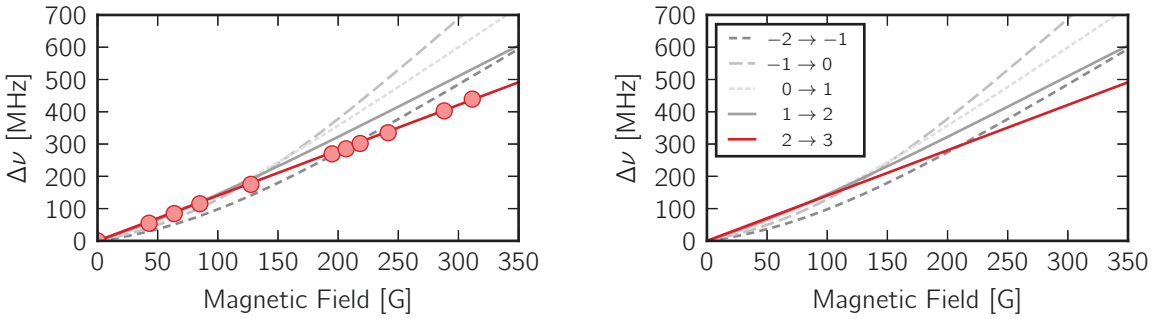

(a) Measured shift of the transition of the extreme m_F-state from $F = 2 \rightarrow F = 3$ (red markers). The solid and dashed lines are theoretical values. The stretched transition is emphasized in red.

(b) Calculation of all σ_+ transitions from $F = 2 \rightarrow F = 3$. The stretched transition is highlighted in red.

Figure 5.3.: Measurement and theory comparison for the measured transition of $|5S_{1/2}, F = 2, m = 2\rangle \rightarrow |5P_{3/2}, F = 3, m = 3\rangle$

The next problem to have a proper two level system is that the stretched transition has to be separated in frequency as far as possible from any other transition to which it could couple. Figure 5.3b shows the calculated evolution of the σ_+ transitions from $|5S_{1/2}, F = 2\rangle \rightarrow |5P_{3/2}, F = 3\rangle$ for increasing magnetic field. With our apparatus we are able to apply a homogeneous magnetic field up to $\sim$ 310 G, which should isolate the stretched transition by roughly $12\Gamma_0$ from the closest other transition. This splitting is good enough for our probing scheme as the probe light is only shone for a brief 300 ns, which leads to a negligible amount of depumping due to the remaining overlap of the neighbouring states. The separation of $12\Gamma_0$ is also larger than the expected line broadening which is expected to be $3\Gamma_0$ (see chapter 3) and should thus be enough to also avoid coupling to neighbouring states due to this effect. Apart of

introducing a line splitting a B-Field also leads to an absolute shift, which for the stretched transition follows:

$$\Delta\nu = \frac{\mu_B}{h} \times B_z \tag{5.1}$$

with $\mu_B = h \times 1.399\,\mathrm{MHz\,G^{-1}}$ [38]. This relation is only true for the stretched transition as due to conservation of total angular moment the two extreme states do not mix population with other states transitioning from low to high B-field and thereby undergoing the change of basis from m_F to m_J. Figure 5.3a shows the experimental finding of the resonance for various B-Fields, which are fitted by a linear function $f(B) = \frac{\mu_{\mathrm{exp}}}{h} B$ yielding a slope of $\mu_{\mathrm{exp}} = h \times 1.391(5)\,\mathrm{MHz\,G^{-1}}$, which is in very good agreement with the literature value.

5.2 Frequency Offset-Lock

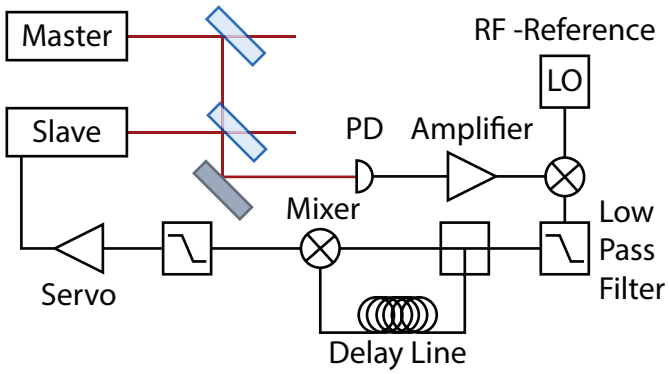

Figure 5.4.: Schematic of a frequency-offset-lock setup.

To be able to follow the resonance over a range of several hundreds of megahertz corresponding to an offset field of 0-310 G the setup used in chapter 3 was not sufficient anymore. The double-pass AOM used on the setup has a bandwidth of $\sim 80\,\mathrm{MHz}$, which would limit the B-field to $\sim 60\,\mathrm{G}$. To overcome this limitation I introduced a new probe laser whose frequency is locked onto the previous probe laser by beating the two and locking the beatnote frequency to a radio frequency (RF) source [81], see figure 5.4. Assuming the two lasers operating at frequency ω_{M} and ω_{S} we get the signal of the photodiode:

$$\begin{aligned} V_{\mathrm{PD}} &\propto (\cos(\omega_{\mathrm{M}}\, t) + \cos(\omega_{\mathrm{S}}\, t))^2 \\ &= 1 + \frac{1}{2}(\cos(2\omega_{\mathrm{M}}\, t) + \cos(2\omega_{\mathrm{S}}\, t)) + \cos([\omega_{\mathrm{M}} + \omega_{\mathrm{S}}]\, t) + \cos([\omega_{\mathrm{M}} - \omega_{\mathrm{S}}]\, t) \end{aligned} \tag{5.2}$$

as the photodiode has a finite bandwidth in my case of $\sim 12\,\mathrm{GHz}$ only frequencies in the radio-frequency range will be detected and the constant term vanishes due to the AC coupling of the photodiode, which reduces (5.2) to the last term $\cos([\omega_\mathrm{M} - \omega_\mathrm{S}]\,t)$. $\omega_\mathrm{B} = |\omega_\mathrm{M} - \omega_\mathrm{S}|$ denotes the beat frequency of the two lasers which then is amplified and mixed with the local oscillator. The output of the mixer can be stated as the sum and difference frequencies $\omega_\pm = |\omega_\mathrm{B} \pm \omega_\mathrm{LO}|$:

$$\cos(\omega_\mathrm{B}\,t) \cdot \cos(\omega_\mathrm{LO}\,t) \propto \cos(\omega_+\,t) + \cos(\omega_-\,t) \tag{5.3}$$

The low pass filter after this mixing stage removes the sum term and the remaining difference signal is split into two parts. One which passes through a delay-line and a second one which directly goes to a second mixer in which those two parts are recombined. The two input signals of this mixer have the same frequency ω_- but one part is delayed by l/v, where v denotes the signal speed in the cable. The output of the mixer is:

$$V_\mathrm{mixer} = \cos(\omega_-\,t) \cdot \cos(\omega_-[t + \frac{l}{v}]) \propto \cos(\omega_-\frac{l}{v}) + \cos(2\omega_-[t - \frac{l}{2v}]) \tag{5.4}$$

Another low pass filter removes the time dependent (oscillating) part and we obtain our final output:

$$V_\mathrm{error} \propto \cos(\omega_-\frac{l}{v}) \tag{5.5}$$

This signal is time independent which means that it only changes when either the local oscillator frequency or the beatnote frequency changes. As this signal is periodic in the length l of the delay line (in our case $\sim 50\,\mathrm{cm}$) the steepness of the slope and the spacing of the zeros can be adjusted by the cable length allowing to adjust these parameters to one's needs. By using this signal as an error signal for the locking system of the slave laser it is possible to change its frequency by changing the frequency of the local oscillator. This scheme allows to scan from a minimal offset of $\sim 100\,\mathrm{MHz}$ up to $\sim 1\,\mathrm{GHz}$ with respect to the master laser's frequency, which is locked to the $\left|5S_{1/2}, F = 2\right\rangle \rightarrow \left|5P_{3/2}, F = 23\right\rangle$ cross-over transition. Thus the resonance could be followed over the full range of magnetic fields (figure 5.3a). For the reader's interest or future replications I listed the parts in Appendix C

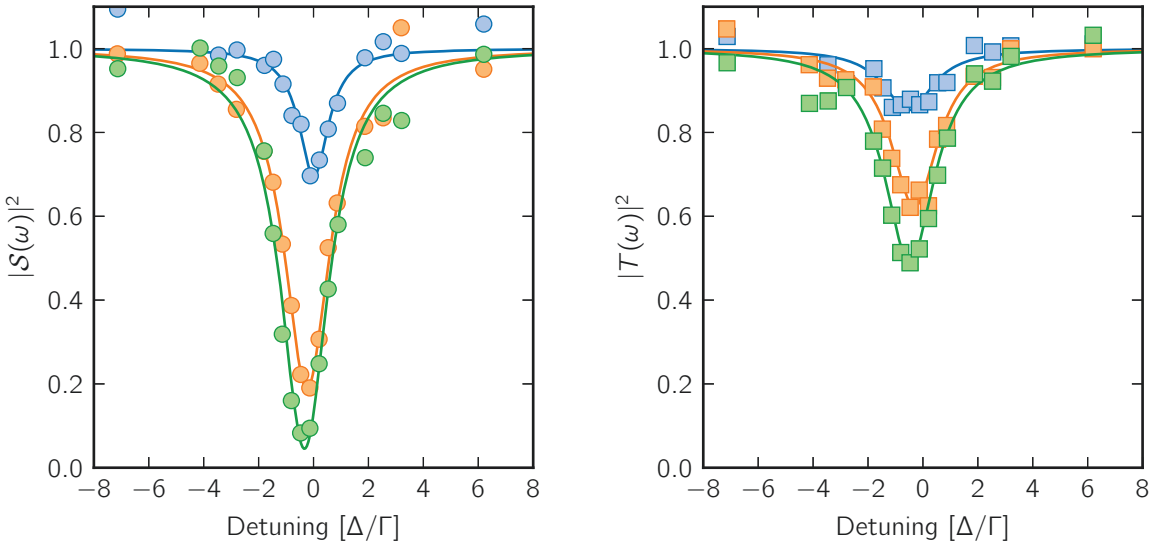

(a) Steady state frequency response measured by the APD

(b) Transmission measured by the CCD

Figure 5.5.: Comparison of the same experimental cycle measured with the APD and CCD. The data points are obtained by measurement and the solid lines are fits by (3.5). The colours indicate different atom numbers: blue = 10 , orange = 60, green = 100

5.3 Measurement of Transmission with a low saturation Probe

As we wanted to measure a set of data which is comparable to the one shown in chapter 3, I performed the same measurements again, but now on a spin polarized sample. As already explained in chapter 3 a flat-top pulse of 300 ns with a peak saturation of $s \approx 0.005$ is shone in, which is repeated for 1000 times interleaved with trap pulses to prevent the expansion of the atomic cloud. This scheme was repeated for typically 300 clouds of atoms per detuning and for a total of 17 different detunings. The transmission probe shown in figure 3.2 is linearly polarized along the y-axis. This leads to a superposition of $\sigma_+ + \sigma_-$ polarization with respect to the quantization axis set by the B-field (see figure 5.1). Figure 5.5 shows the results for the APD on the left and for the CCD on the right for three different atom numbers. The data is again fitted by (3.5) and the extracted fit parameters amplitude A, width Γ_c, and shift Δ_c are plotted versus the according atom number in figure 5.6 (fit results are available in Appendix D).

Before we discuss the results it is interesting to have a look at what we expect to change for the amplitude going from a 12-level to an effective 2-level system. Intuitively

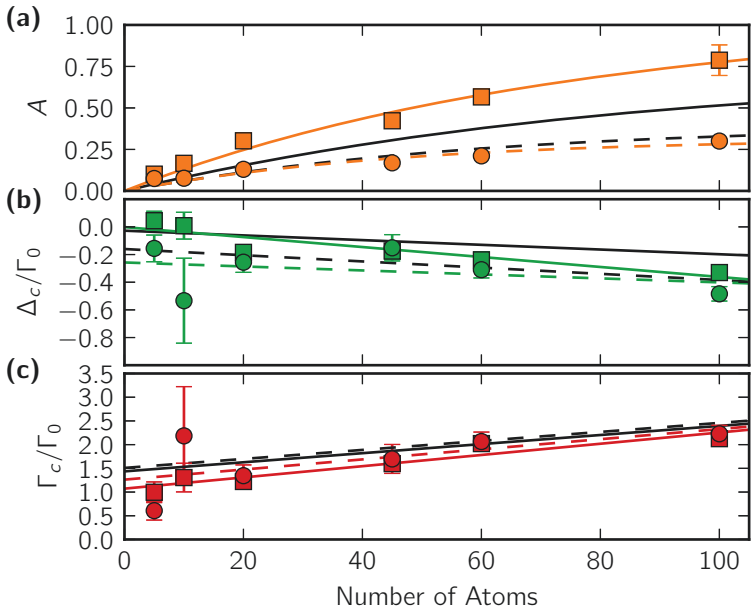

Figure 5.6.: Plots of the data points together with the fitted function. In all plots circle refer to the APD data and squares to the CCD data, solid and dashed lines are fits, respectively. The black lines (solid and dashed) are the corresponding results from chapter 3 for the 12-level system (see figure 3.6). **(a)** shows the amplitude parameter of the fit function F, **b)** shows the shift of the central $\Delta_c = \omega_c - \omega_0$, **(c)** Full width at half maximum Γ_c

the dipole-moment has to be larger in the 2-level case as all atoms are prepared in the stretched state and thus the Clebsch-Gordan coefficient is 1 compared to 7/15 corresponding to the average value for a 12-level system. Additionally the probe light polarization has to be taken into account as it is for our setup a super-position of $\sigma_+ + \sigma_-$. The total field can be split in a sum of the laser-field and the atom-field along the z-axis:

$$E_{\text{tot}} = E_{\text{L}} + E_{\text{sc}} = \underbrace{-i\frac{z_{\text{R}}}{r}E_0 e^{ikr}}_{\text{far field Gaussian beam}} + \underbrace{\frac{\langle d\rangle}{4\pi\epsilon_0}\frac{k^2}{r}e^{ikr}}_{\text{scattered light from dipole}} , \tag{5.6}$$

with the average dipole moment $\langle d\rangle = \epsilon_0 \alpha E_0$ and z_{R} the Rayleigh-range. As we are looking close to resonance the polarizability α simplifies to $\alpha = i6\pi/k^3$ and the cross-section is given by $\sigma = 6\pi/k^2$ [38]. We can thus rewrite (5.6) in terms of

scattering cross-section:

$$-iE_0\frac{z_\mathrm{R}}{z}e^{ikr}\left[1-\frac{\alpha k^2}{4\pi i z_\mathrm{R}}\right]=-i\frac{z_\mathrm{R}}{z}E_0e^{ikr}\left[1-\frac{\sigma k}{4\pi z_\mathrm{R}}\right] \tag{5.7}$$

This now allows us to compare the case of the 12-level with an ideal 2-level (pure probe polarization) and our effective 2-level system. The relation between a multilevel system and a perfect two level system is given by:

$$\frac{7}{15}\,\sigma_{2\mathrm{lvl}}^{\mathrm{ideal}}=\sigma_{12\mathrm{lvl}} \tag{5.8}$$

where the $\frac{7}{15}$ is the reduction in polarizability due to averaging over the internal m_F states. The perfect two level system here refers to a two level system that is also perfectly driven, meaning that the entire driving field has the correct polarization. As this is not the case in our measurement, because we probed the atoms with linearly polarized light perpendicular to the quantization axis we ended up with a superposition of $\sigma_+ + \sigma_-$ polarization with respect to the quantization axis of the atoms. To take this into account the scattering cross-section of the sample is reduced by $\sqrt{2}$, which leads to:

$$\sqrt{2}\,\sigma_{2\mathrm{lvl}}^{\mathrm{eff}}=\sigma_{2\mathrm{lvl}}^{\mathrm{ideal}} \tag{5.9}$$

With (5.8) and (5.9) we get the following relation:

$$\frac{7\sqrt{2}}{15}=\frac{\sigma_{12\mathrm{lvl}}}{\sigma_{2\mathrm{lvl}}^{\mathrm{eff}}} \tag{5.10}$$

This means that the ratio between the amplitude curve of the 12 level and 2 level case should be ~ 0.66. We have to compare this value to the ratio of the orange and black solid line of figure 5.6 (a) which correspond to fits to the amplitude results of the APD for 2 and 12-level, respectively. Dividing one curve by the other yields 0.66 ± 0.01, which is in very good agreement with our estimate. Performing the same operation for the dashed green and black line the results of the CCD we obtain a value close to 1. So far we have not found a plausible explanation for the discrepancy between APD and CCD.

For a system in which the response is given mainly by one mode the line shift Δ_c is given by:

$$\Delta_\mathrm{c} \propto \mathrm{Re}[V_\mathrm{dd}] \tag{5.11}$$

and the linewidth Γ_c can be written as:

$$\Gamma_c \propto \mathrm{Im}[V_{dd}] + \Gamma_0. \tag{5.12}$$

As $V_{dd} \propto Cn\lambda\!\!\!^{-3}\Gamma_0$ with C the Clebsch-Gordan coefficient we directly expect a ratio of 7/15 between the results of the 2 and 12-level system for the peak shift and linewidth change. The fit for the APD gives a slope of -0.004 ± 0.001 and -0.002 ± 0.0002 for the 2 and 12-level measurements, respectively. If we now calculate the ratio of those two disregarding the errorbars we obtain 0.5 which deviates only 7% from 7/15. In comparison to the APD the CCD (-0.001 ± 0.002) result does not show any traces of change between the two measurements, taking the errorbars of APD and CCD into account the two measurements are compatible with one another. The APD now agreeing with the CCD contradicts the agreement with the theoretical expectation which is not met by the CCD results. This discrepancy will only be resolved by expanding the range of density explored to reduce the errorbars which we could not do in the present state of the apparatus.

Also for the width, a ratio of 7/15 is expected following the argument of (5.12) which neither the APD nor the CCD shows (figure 5.6 (c)) as the red solid (APD) and dashed (CCD) lines are parallel to the 12-level measurements in black. This fact in itself is very interesting, because it means that this quantity seems independent of transition strength. We point out that the width of the sample's response is only dependent on the density and maybe also on the absolute sample size. The dependence on the sample size is a consequence of the discussion in chapter 3.8.3. As multiple scattering can simply be increased by making the volume larger and keeping the density constant whereas recurrent scattering can only be increased by increasing the density and thus decreasing the spacing between two adjacent scatterers. This means that for example a simulation using two atoms and varying the spacing to emulate different densities will not lead to the same result as simulating the same densities with samples of for example 30 or 100 atoms. Such extensive scaling behaviour is to be expected for system with long range interaction.

The two level measurement was performed two years after the 12-level measurement was done. This should rule out any short-term biasses, which could lead to the very similar results of the shift and width measurements. Also having changed a substantial part of the setup by introducing a new probe laser should have reduced the likelihood of systematic errors due to using the same apparatus again.

5.4 Comparison with Theory

As we are now only dealing with a 2-level system we can now focus on a subset of the problem discussed in chapter 3.8, namely the removal of internal structure of the scatterers, shown in figure 5.7. This simplifies the equation to describe the system to

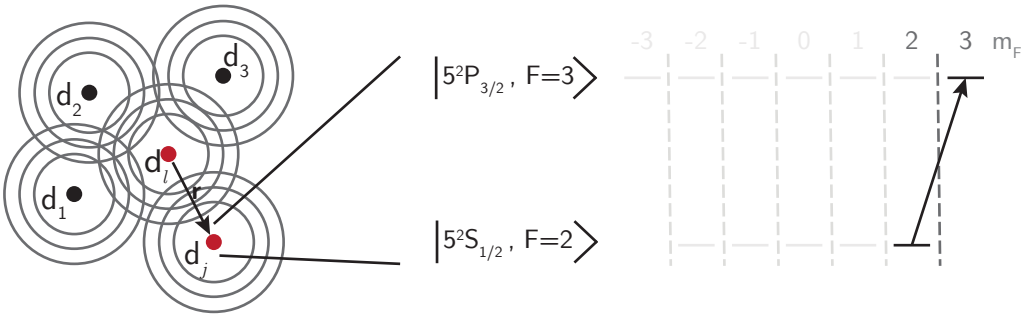

Figure 5.7.: Show the simplification of the new 2 level system with respect to the 12 level case

(5.14) and (5.13). In order to account for the experimental conditions, in which the probe laser polarization is a superposition of σ_+ and σ_-, the driving field was divided by $\sqrt{2}$:

$$(\Delta + i\frac{\Gamma}{2})\mathbf{d}_j = \frac{\Omega}{\sqrt{2}} + \sum_{l \neq j}[\mathbf{V}_{lj}]\,\mathbf{d}_l, \tag{5.13}$$

with

$$V_{\mathrm{dd}} = -\frac{3\hbar\Gamma}{8}e^{ikr}\left[\left(\frac{1}{(kr)^3} - \frac{i}{(kr)^2}\right)(1 - 3\cos^2\theta) + \frac{1+\cos^2\theta}{kr}\right], \tag{5.14}$$

which are essentially the same equations as (3.9) and (3.8), but taking into account the experimental conditions. This experimental improvement simplifies the theoretical approach tremendously as we have perfect knowledge about the initial state of the atoms and know exactly on which transition we operate them. We thereby removed all uncertainties resulting from the presence of internal structure.

In figure 5.8 the simulation is shown for various atom numbers comparing the measurement results with the simulation. On the one hand we can see that we get better agreement for small atom numbers than in the 12 level case, which simply indicates that the chosen initial distribution of the m_F-states for the simulation was not perfect. On the other hand looking at the higher atom numbers we see that the level of disagreement reached for the 12-level case at ~ 180 atoms is now reached at

~ 100, which is roughly a factor 2 lower. To grasp the experimental and theoretical

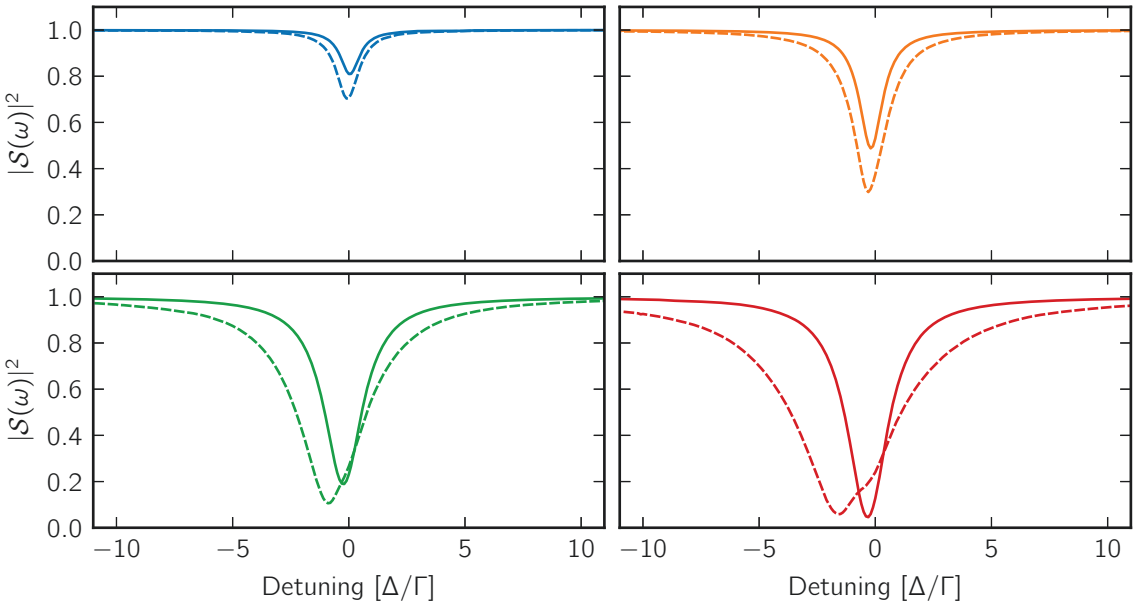

Figure 5.8.: Comparison of the microscopic two level theory (dashed line) and the fit of the APD (solid line). The different colours indicate the atom number: blue = 5, orange = 20, green = 60, red = 100

discrepancy better I did the same as in chapter 3.9, where I numerically extract the amplitude, FWHM and shift of the simulation and then plot that together with the experimental finding of figure 5.9. The amplitude shown in figure 5.9 (a) agrees for the low atom numbers better than for the 12 level system but still does not agree very well, as the curvature of the simulated and experimental curves are different. It can clearly be seen that the experimental curve (red) crosses the simulated amplitude at around 60 atoms and settles at a higher value than the simulation. The plots for the shift (b) and FWHM (c) agree qualitatively again as was the case for the 12 level system, as far as the slope has the right sign, but the magnitude does not agree. The kinks in the simulation results (blue) in figure 5.9 are artefacts due to finite sampling in atom number and frequency. In spite of stripping the atoms of the complexity of their internal structure, thereby providing the most favourable grounds to compare experiment and theory, the discrepancy between the two remains striking.

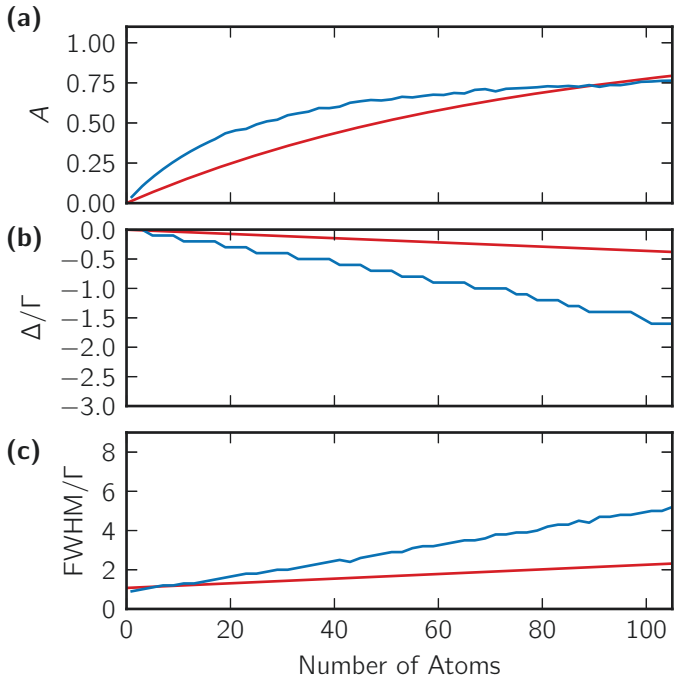

Figure 5.9.: Shows the comparison between the experimental data fit of the APD (red) and the 2-level microscopic theory (blue). (a) Amplitude, (b) shift of peak, (c) Full width at half maximum

5.5 Temporal Response

As an interesting side note I wish to show the transient analysis that could be extracted from the experiments discussed above as we recorded the full temporal response. To analyse the transient we consider the cloud as a whole to be a dipole D with linewidth γ_c and shift Δ_c we can then write the following relation to describe this system:

$$\dot{D} + (\Delta_c + i(\gamma_c + \Gamma_0)/2)D = \epsilon_0 \alpha E \exp(i\omega t) \tag{5.15}$$

We cast the solution of this differential equation in the following form:

$$D(\Delta_c, t) = |A(1 - \frac{B}{1 + 2i\Delta_c/\gamma_c}(1 - \exp(-2\pi\, 0.006\, t\, (\gamma_c/2 + i\Delta_c))))|^2, \tag{5.16}$$

with A, B, γ_c free fit parameters, A and B are relative amplitudes and γ_c the linewidth in units of Γ_0 such that the time constant $\eta = 1/(2\pi\, 0.006\, \gamma_c)$. In figure 5.10a and 5.10b we can see the response for two different atom numbers together with the fit results. η is related to the natural linewidth by $\eta = 1/\Gamma$, which for a single Rubidium

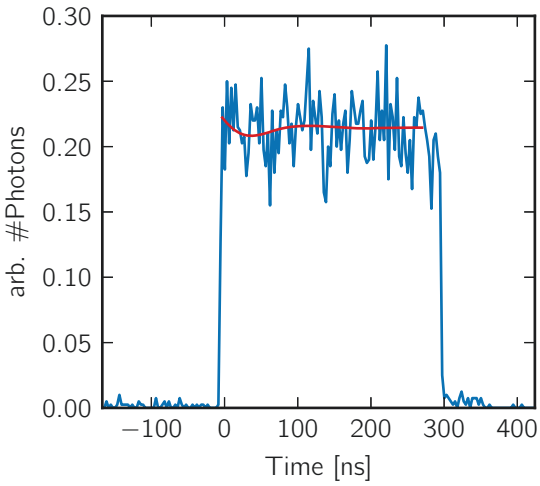

(a) 10 atoms at $-1.1\Delta_c/\Gamma_0$

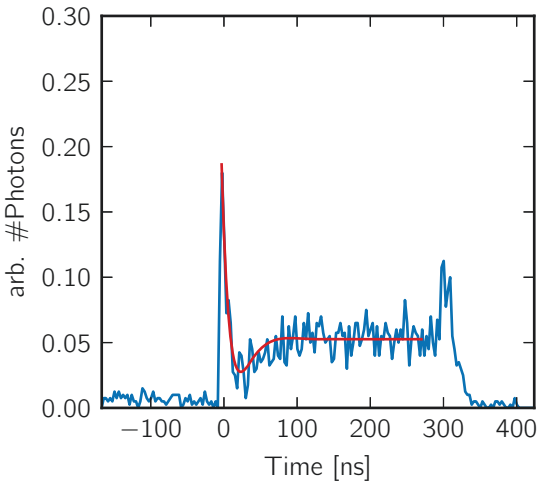

(b) 100 atoms at $-1.1\Delta_c/\Gamma_0$

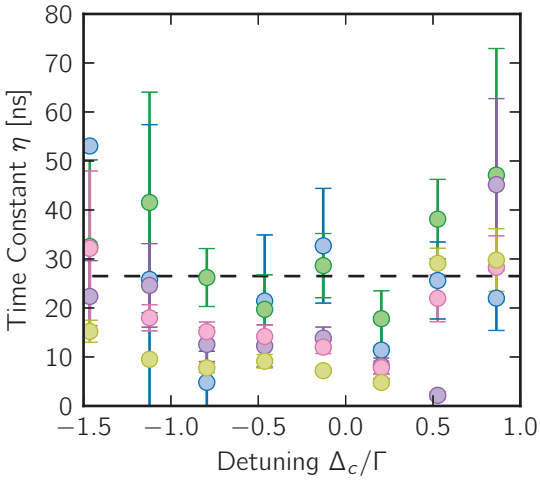

(c) Extracted decay constant η versus the detuning.
yellow = 100 atoms, pink = 60 atoms,
purple = 45 atoms, green = 20 atoms,
blue = 10 atoms.
The black dashed line indicates $\eta_0 = 26.5\,\mathrm{ns}$.

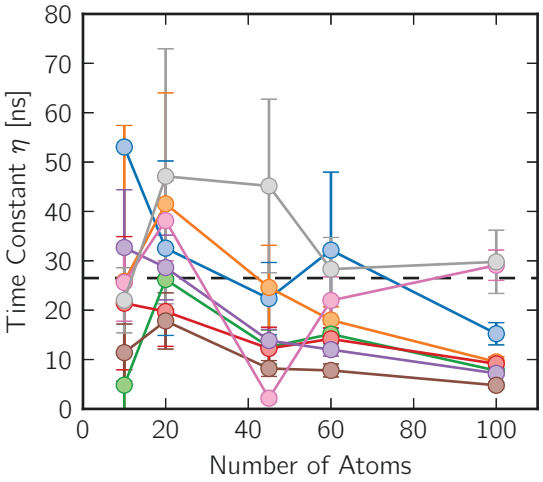

(d) Extracted decay constant η versus the number of atoms.
blue = $-1.5\Delta_c/\Gamma_0$, orange = $-1.1\Delta_c/\Gamma_0$,
green = $-0.8\Delta_c/\Gamma_0$, red = $-0.5\Delta_c/\Gamma_0$,
purple = $-0.1\Delta_c/\Gamma_0$, brown = $0.2\Delta_c/\Gamma_0$,
pink = $0.5\Delta_c/\Gamma_0$, grey = $0.9\Delta_c/\Gamma_0$.
The black dashed line indicates $\eta_0 = 26.5\,\mathrm{ns}$.

Figure 5.10.: Temporal responses of the two level system (a) and (b). (c) and (d) show the results of the fitting for all detunings and atom numbers.

atom amounts to $\eta_0 = 26.5\,\mathrm{ns}$. If now the decay constant is smaller than the one of a single atom the response is commonly called "super-radiant" [6, 82, 83] and if the

decay-constant is larger we talk about "sub-radiant" decay [84–87]. For the 12 level samples it was not possible to find a significant deviation from 26.5 ns, but now with the two level system it was possible to observe super and sub-radiance, as we are going to see. Another feature that is clearly visible in figure 5.10b is the peak at the end of the pulse. This "flash" at the end of the pulse comes from the fact, that at the moment where it appears the incident light was switched off and thus the light still propagating through the sample does not interfere destructively with the laser light of the probe. Such interesting behaviours could only be observed for a very small subset of the measurements, it is thus beyond the scope of the work presented in this thesis to provide any sort of in-depth study. A thorough analysis can be found in [11, 12] where this flash is studied in large sample and thus propagation effects were taken into account. To study this effect in detail we need to gather more data but our microscopic cloud should simplify the model to $|E_\mathrm{L} + E_\mathrm{sc}|^2$ without propagation effects.

In figure 5.10c we can clearly see that around zero detuning we obtain for large number of atoms (~ 100) super-radiant behaviour as the data points are clearly below the black dashed line which indicates the reference for a single atom response. The super-radiant response agrees with the measured broadening in steady state as $1/(2\,\pi\,2.5\,\Gamma_0) \approx 10\,\mathrm{ns}$. The values measured for points of $|\Delta_\mathrm{c}/\Gamma_0| \geq 1$ should not be called sub-radiant as there is no clear settling time and the curve is just flat on top, that is why these results are more and more sub-radiant. Additionally we can see in figure 5.10d that the evolution of the time constant seems to be similar for all detunings with respect to the number of atoms, but no explicit relation can be deduced from this dataset.

5.6 Measuring Transmission for a high saturation Probe

So far we only looked at the limit where the sample behaves like a set of classical dipoles, which is to say each dipole's response is linear as a function of the driving field. If we now increase the driving field strength to the point where $\frac{I}{I_\mathrm{sat}} \geq 1$ we enter the regime which is dominated by quantum mechanical effects, such as power-broadening and Rabi-oscillation. As proper quantum mechanical modelling [88] is beyond the scope of this thesis I will only provide the experimental results and a qualitative explanation. All effects that we are going to see have to my knowledge never been reported before and it is unclear what to expect as there are also no theoretical predictions.

Working with probe beams of high intensity comes with a major issue as the atoms are pushed by the probe itself. It is then impossible to send more than one pulse per

atomic cloud, which severely restricts the amount of data that may be acquired. In practice, due to the fact that our time-tagging device is only able to mark one photon per pulse, this would have meant an increase in measurement time by a factor ~ 1000 to keep the signal to noise ratio the same as I decreased the number of pulses from 1000 to 1. This would have made it impossible to acquire any meaningful data. For this reason I did not measure the temporal response and instead only acquired data from the CCD. I repeated each detuning for typically 400 samples. As a result I obtain again Lorentzian-like responses, which were fitted by (3.5): $|T(\omega)|^2 = |1 - \frac{A'}{1-2i\frac{\omega-\omega_c'}{\Gamma_c'}}|^2$ (Spectra in appendix F). In order to study the change in behaviour between low and high saturation, I performed the experiment for $I/I_{\mathrm{sat}} = s \approx 0.01, s \approx 1$ and $s \approx 8$, the three fit results are plotted versus atom number in figure 5.11. The amplitude was fitted by the function $A(N) = 1 - \sqrt{a + (1-a)\exp(-b\,N)}$ and the shift Δ_c as well as the FWHM Γ_c with a linear fit of type $f(N) = \alpha + \beta\,N$ with a, b and α, β as free fit parameters (results in appendix E).

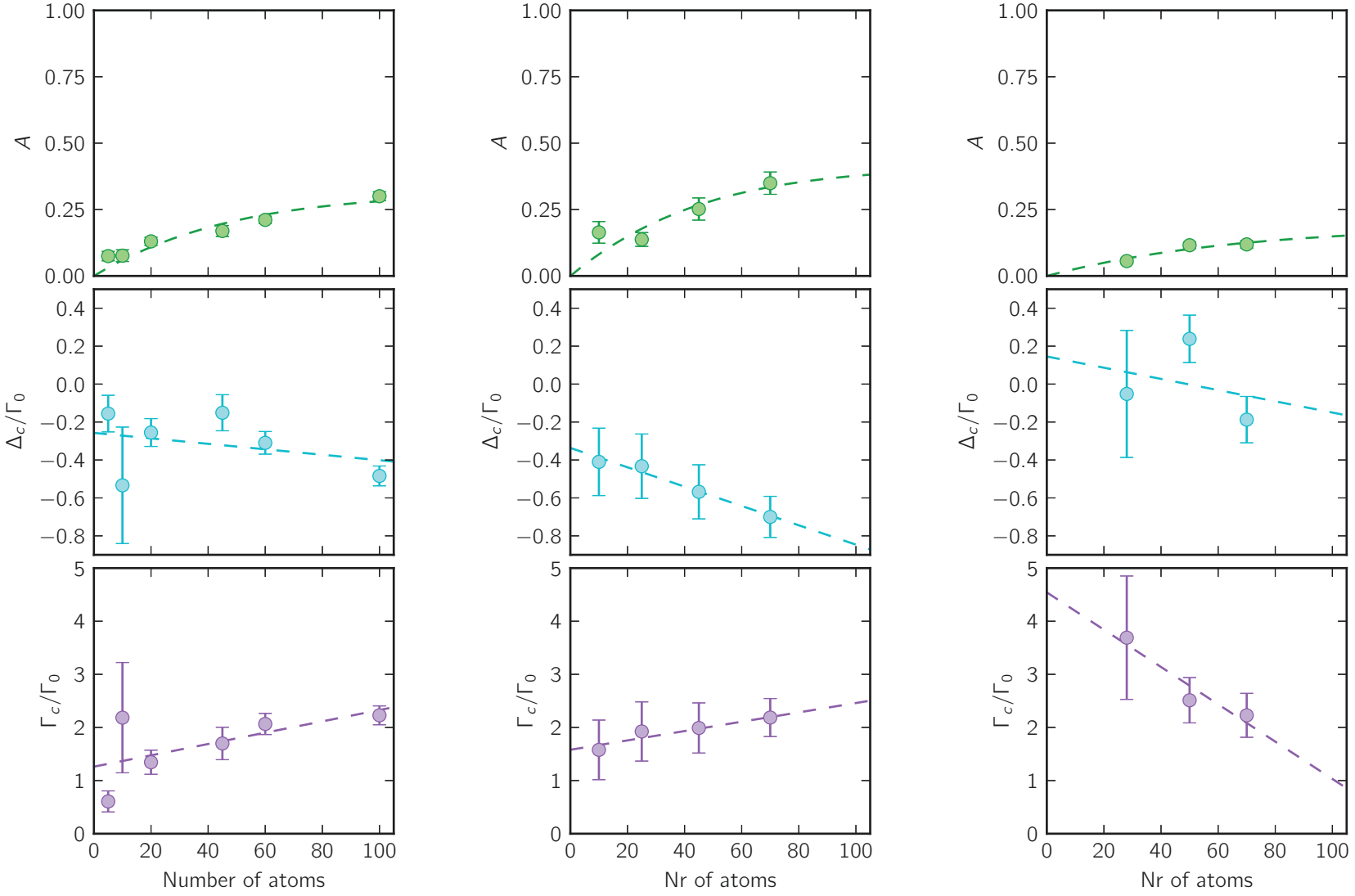

(a) $s \approx 0.01$ **(b)** $s \approx 1$ **(c)** $s \approx 8$

Figure 5.11.: Fit results for various probe saturations measured by the CCD.

The variation of the amplitude A as a function of saturation (figure 5.11) shows a rather peculiar behaviour as A is larger for $s \sim 1$ than it is for $s \ll 1$. So far no satisfying answer was found. Having a decrease going further up in saturation $s \approx 8$ can be understood due to having a fully saturated scattering rate. As more photons are shone in more and more pass through the medium without being scattered and thus the "contrast" of the signal decreases.

The observation for the shift (figure 5.11) of the peak is also somewhat inconclusive as we first see the slope getting steeper going to $s \approx 1$ and then less steep again but obtaining a fairly large offset.

Unlike the other parameters the FWHM is revealing an interesting and unexpected fact: the linewidth for independent atoms is related to the saturation by:

$$\gamma = \Gamma_0 \sqrt{1 + s} \tag{5.17}$$

This suggests that the slope throughout all three measurements should have the same sign and magnitude. What we see in fact is rather that the slope starts with a positive sign at $s \approx 0.01$ getting less steep going to $s \approx 1$ and then changes sign going to $s \approx 8$. Such a behaviour rather indicates that the saturation the sample experiences for different atom number varies. The linewidth for the higher atom numbers, starting at > 40 hardly changes, where as the samples with lower atom number show a way larger influence due to the change in probe saturation.

5.7 Measuring the density dependence of the saturation intensity

To have an independent measurement of the saturation I kept the atom number constant (~ 70) and measured the fluorescence of my sample for various intensities of the σ_+ polarized fluorescence probe. In addition I repeated this measurement for various time of flights of the sample after switching off the trap so as to measure the response of samples with different densities. As discussed before varying the volume and keeping the atom number constant is strictly speaking not the same as keeping the volume constant and varying the number of atoms. I tried changing the atom number first, but this was too time consuming as for low atom number and low saturation there is very little signal, so to obtain a meaningful signal the integration time would have been very large. A long integration time would have probably also introduced an error due to the motional effects induced by the intense probe light which could have washed out the effects we are trying to capture. Figure 5.12 shows the measurements

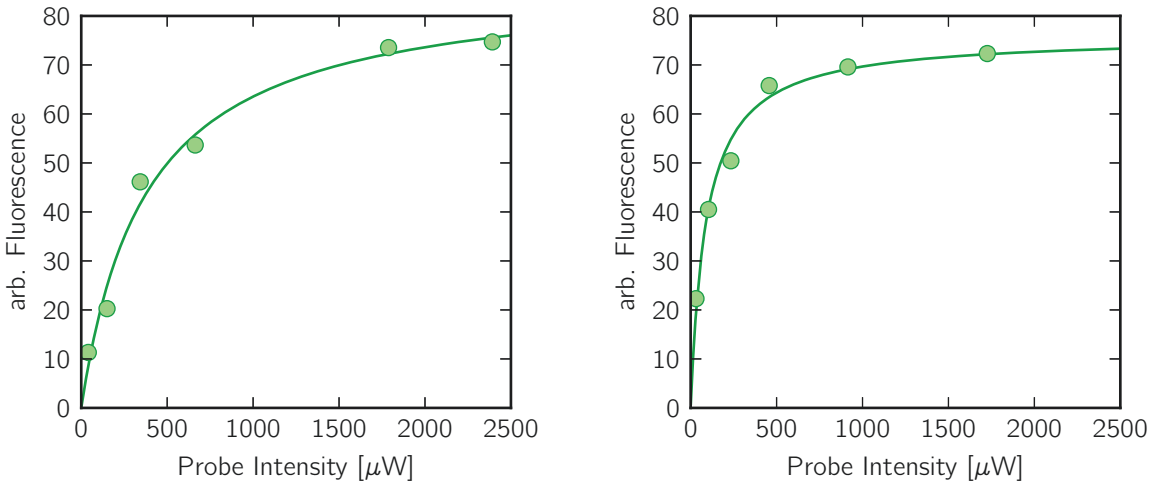

(a) Dense $\sim 10^{14}\,\mathrm{atoms\,cm^{-3}}$ **(b)** Dilute $\sim 10^{11}\,\mathrm{atoms\,cm^{-3}}$

Figure 5.12.: Measurement of I_{sat} for different densities

for two different densities (atoms = 70) where I measure the amount of fluorescence for different input intensities close to resonance. As stated in [38] the total photon scattering rate of a single 2-level atom is given by:

$$R_{\mathrm{sc}}(I) = \left(\frac{\Gamma}{2}\right)\frac{(I/I_{\mathrm{sat}})}{1+4(\Delta/\Gamma)^2+(I/I_{\mathrm{sat}})}, \tag{5.18}$$

with Δ the detuning, Γ the natural linewidth and I_{sat} the saturation intensity, which in our case for the stretched σ_+ transition is $1.7\,\mathrm{mW\,cm^{-2}}$. This allows to fit the data close to resonance ($\Delta = 0$) by:

$$P(I) = a\,\frac{b\,I}{1+b\,I}, \tag{5.19}$$

with a and b as free fit parameters and I the input intensity. It directly follows that:

$$b = \frac{1}{I_{\mathrm{sat}}} \tag{5.20}$$

With this knowledge it is possible to directly extract the saturation intensity from the measurement. I took seven different moments within the free flight of the atoms, which lead to a range of densities ρ of 5×10^{13} to $10^{10}\,\mathrm{atom\,cm^{-3}}$, shown in figure 5.13. As we can see for short time of flight and thus high densities there is a group of data points for which the average $\langle I_{\mathrm{sat}}\rangle \approx 9.5\,\mathrm{mW\,cm^{-2}}$. Between 5 and 10 μs expansion time of the cloud the saturation intensity drops to roughly $3.2\,\mathrm{mW\,cm^{-2}}$, which corresponds

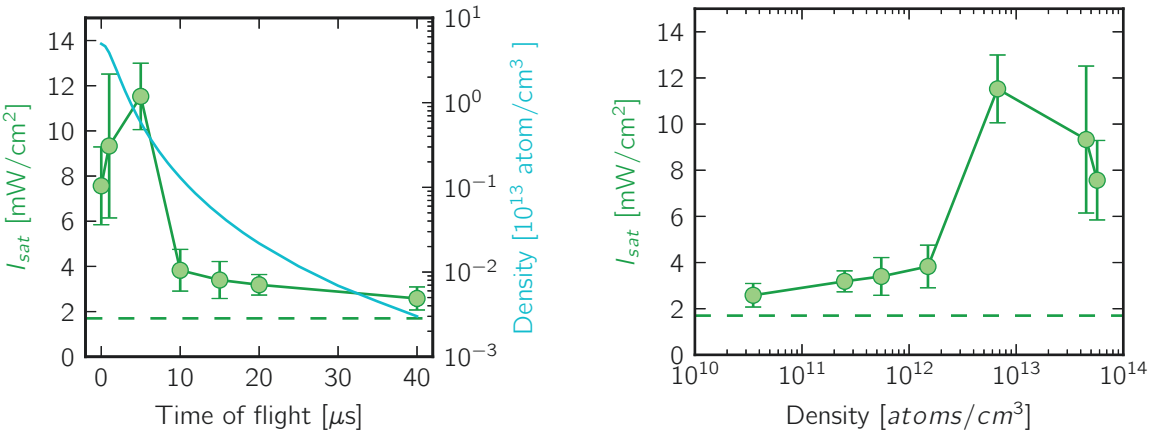

(a) Variation of the saturation intensity I_{sat} for different probing times after a time of flight (green), together with the according calculated density (blue) of the sample at that moment. The dashed green line indicates the literature value of $I_{\mathrm{sat}} = 1.7\,\mathrm{mW\,cm^{-2}}$.

(b) Saturation intensity versus density

Figure 5.13.: Saturation intensity behaviour

to a factor of 3 between the dense and dilute case. The offset of the dilute samples with respect to the literature might be due to the fact that the measurement was not performed exactly at resonance, which would lead to an increase in saturation intensity as the scattering cross-section is reduced. As this would only lead to a systematic offset the factor of three would remain. With this independent measurement I could confirm what we expected from the chapter 5.6, namely that the saturation intensity is not constant and actually depends fairly violently on the density. The exact dependency cannot be derived from this measurement as the sudden drop is undersampled. This independent measurement of $I_{\mathrm{sat}}(\rho)$ confirms the assumption of chapter 5.6. As the more dilute samples have $3\times$ lower saturation intensity the effect of power broadening is more striking for them then for the denser samples.

5.8 Conclusion

In this chapter we first saw that it is possible to prepare dense atomic samples with an 80% efficiency in a pure m_F state, while only causing a moderate temperature increase of $\sim 25\%$. Using these 2-level systems it was possible to see that the linewidth

broadening is independent of the transition strength of the dipoles. We have seen that the APD measured the predicted change in amplitude between 12 and 2-level system. For the CCD we did not find this predicition and are left with a discrepancy between the two detectors for which we have not found a plausible explanation, so far. The result for the shift Δ_c is not completely clear ignoring the errorbars on the measurement values we could say that it fulfills the prediction but taking them into account could also lead to the conclusion that APD and CCD agree but then the prediction is not confirmed. Measurements over a larger density range are required to finally conclude on this point.

The comparison between the measured two level system and the theory showed a clear improvement for low atom numbers. Going to higher number of atoms and thus higher densities showed instead the same discrepancy as before. This clearly rules out the point raised about the internal structure causing the disagreement between theory and experiment in chapter 3.10. The better agreement between theory and experiment for small atom numbers also suggests that the size of the cloud is well known. There is nonetheless the slight possibility that the sample's geometry changes with the number of atoms contributing to the overall disagreement at higher densities.

Analysing the temporal response and in particular the transient we found that for the high atom numbers, which show a broadening of up to $2.5 \times \Gamma_0$, the corresponding settling time of $1/(2.5_0) \approx 10\,\text{ns}$ can be seen on the data as well.

Afterwards we investigated what happens when we leave the regime of low saturation probing and enter the domain of high intensity. We saw that for low atom number the measured linewidth changes dramatically with probe intensity, whereas for denser samples this was not the case. As a logical consequence we conducted an independent measurement of the saturation intensity and indeed found out that I_{sat} is not constant in density ρ. Sadly it is not possible to derive a functional form for $I_{\text{sat}}(\rho)$ as it has a fairly sudden jump and is not well enough sampled to draw any more quantitative conclusions. Nonetheless it allowed us to independently confirm the assumption that I_{sat} is no longer constant. These results have to my knowledge never been reported before neither do any theoretical predictions exist.

Chapter 6

Summary & Outlook

In this work we started off to investigate the influence of density to the atomic response of an optical transition. As stated in the introduction many answers to the interaction between light and matter have been found till today, but this particular question about the density dependence has not received a lot of attention.

Additionally the contradicting works of the group of Charles Adams [26] and our group [25] required a more detailed study of these density induced effects to reach a conclusion. To improve on the reliability of our data taking major improvements to our experimental apparatus, which are described in chapter 2, had to be done. Those upgrades on the technical side of the experiment empowered us to improve significantly on the repetition rate (a factor of ~ 10) and the repeatability of our experiments. With these improvements in place it was possible to change to transmission measurements of a sub-micron cloud of Rubidium 87 and successfully gather a fair share of new data. As explained in the introduction going from fluorescence measurements to transmission, allowed us to investigate the validity of two well-established theories in the case of a dense cold sample. The first theory being a macroscopic theory describing the sample by an index of refraction n (continuous medium approach), by relating this macroscopic quantity, to a microscopic quantity, the single atom polarizability α. With such a theory it is possible to describe a sample consisting of thousands of microscopic elements by just one quantity. The second theory is a microscopic theory, which is called the "coupled-dipole equation", for this model it is necessary to have additional knowledge of the internal structure of the sample such as the individual position of each microscopic particle. Both theories are very successful in describing a plenitude of physical phenomena such as refractive indices of gaseous media, meta-materials and in general all sort of real-world scattering phenomena and can therefore be considered "well-established".

In chapter 3 we began probing the microscopic atomic cloud with a weak intensity beam $\frac{I}{I_{\text{sat}}} < 0.1$, while being in a situation where all m_F states are degenerate due to the low ambient magnetic field of $|\mathbf{B}| < 80\,\text{mG}$. In this setup it was possible to explore peak densities ranging from $\sim 10^{12}\,\text{atom}\,\text{cm}^{-3}$ up to $\sim 10^{14}\,\text{atom}\,\text{cm}^{-3}$

by varying the number of atoms inside a trap with constant volume. Operating without a spin polarized sample made it necessary to take all twelve levels of the $\left|5S_{1/2}, F = 2\right\rangle \leftrightarrow \left|5P_{3/2}, F = 3\right\rangle$ transition into account to model this measurement accurately. By doing so we found for the macroscopic model a correction term of $\frac{7}{15}$ for the dipole moment, with respect to an ideal two level system. For the microscopic model we took the internal structure into account by stochastically sampling the internal states. Comparing the outcome of these two models first revealed that for low atom numbers (low densities) they lead to the very same result, but when the atom number involved gets high enough a striking difference emerges. This discrepancy may be qualitatively explained by accounting for two different types of scattering events. One type which we call "multiple scattering" involving each scatterer in the sample maximally once and "recurrent scattering", which scatters at least twice on the same constituent. Comparing the result of the continuous media model and the coupled-dipole equation, to the performed transmission measurements it turned out that neither describes the experimental findings. Of course the difference is a bit smaller for low atom numbers and gets more striking for larger ones, but we find no true quantitative agreement. This finding supports the prior work [25] done in our group, but still left many questions unanswered. As theoretical descriptions always focus on the idealization of the actual experiment and experiments always struggle with technical imperfections we compiled a list of possible short-comings:

1. Alignment issues, which might have introduced a frequency shift
2. Uncertainty about the sample size, as it is smaller than our optical resolution
3. Motional effects, which are not taken into account in the model
4. The internal structure of Rubidium 87, which leads to imperfect knowledge about the initial state

Alignment issues

The first point on that list was tackled next, by simulating longitudinal and transversal displacement of the cloud with respect to the probe beam (chapter 3.11). Comparing these simulations we found good agreement with the measured data and were able to rule out any influence of a frequency shift. The longitudinal displacement causes an asymmetry, which was explained by an additional phase factor introduced due to the Gouy-phase within the Rayleigh range of the focused laser beam. The transverse

displacement simply causes a reduction in amplitude as the spatial mode-matching between beam and sample is not optimal any longer.

Internal structure and sample size

In order to simplify the system to an ensemble of two-level atoms thereby removing the possible influence of the internal structure on the measurements, we prepared spin-polarized samples (chapter 5). To our surprise it worked reasonably well to pump the atoms into the extreme m_F, which allowed us to prepare $\sim 80\%$ of the sample in the $\left|5S_{1/2}, F = 2, m_F = 2\right\rangle$ state. Normally this task is considered to be complicated due to the fact that the rescattered light of neighbouring atoms might lead to depumping. These spin polarized samples were then probed by a weak probe $I/I_{\text{sat}} < 0.01$ in an environment of $B_z = 310\,\text{G}$ lifting the degeneracy and preventing any depumping of the $\left|5S_{1/2}, F = 2, m_F = 2\right\rangle \leftrightarrow \left|5P_{3/2}, F = 3, m_F = 3\right\rangle$ transition. Repeating the measurements of chapter 3 with this new sample, allowed me to directly compare the case with internal structure and without.

This direct comparison revealed that the linewidth Γ_c seems to depend only on the density and not on the dipole moment. Indeed, although the absolute value of Γ_c differs slightly for the two cases, this discrepancy can be assigned to a combination of error bars and systematic bias, such as the finite laser linewidth and the offset of the locking point. The situation for Δ_c is not as clear the dataset as it is suggests that the expectation is fulfilled as we find increase in the slope by roughly 5/17, but taking the errorbars properly into account it could also be concluded that it does not. To finally settle on this a measurement over a larger density range is necessary. The measured amplitude of the dip for the case of 12 and 2-level atoms by the APD agrees extremely well with the theory, which predicts that the ratio between these two measurements should be ~ 0.66. The measurement performed with the CCD exhibited a very surprising discrepancy which is up to now unexplained. For small atom numbers (low density) the agreement with theory was clearly improved. By pumping the atoms to the extreme m_f state and applying a very large magnetic field we ensured that only this population would be addressed by the probe, thereby removing the uncertainty over the initial distribution that marred the 12-level experiment. Increasing the density of the sample leads to a stronger departure of the theory with respect to the experiment. By working with two-level rather than twelve level atoms, this disagreement is even enhanced: only 100 two-level atoms reach the same degree of disagreement as 180 twelve-level atoms. This is a clear confirmation that the internal

structure cannot be at the root of the failure of available theories to describe the behaviour of the dense sample we are studying. Having the theory agree well for low number of atoms also indicates that the size of the sample is reasonably well known assuming that the shape is independent of the atom number.

Motional effects

The last point of the possible influences is also the hardest to test experimentally and it was not possible to contribute to this point during this thesis. It might be that pairs of atoms which are fairly close together experience a strong repelling force from the induced dipole when the probe light is shone in, this could lead to a modification of the response of our sample. So far there are no theoretical attempts to integrate this influence in the existing theory which seems to be a rather challenging problem.

Pulse Propagation

As we were interested in gaining a consistent picture for the twelve-level system we embarked on measuring not just the steady-state magnitude for the transmission, but also the phase which gets imprinted on the light passing through the sample. To do so we substituted the square pulses shone on to the atomic cloud by Gaussian shaped pulses and measured their arrival time with respect to a reference case without the sample in the beam-path. The results of these measurements are shown in chapter 4. Using the fit function from the previous chapter as a linear transfer function together with the obtained fit parameters we were able to calculate the outcome of the pulse propagation without any further free parameter. With this experiment we now have the full knowledge about the interference process as we have measured phase and magnitude. Additionally, the outcome of these pulse propagation experiments showed remarkable properties: A slab of $3\,\mu$m thickness and the same density as our sample would have a group refractive index of up to $n_{\mathrm{g}} \approx -10^6$, which is the largest value known until today for this quantity. Another outstanding property is the large fractional pulse advancement, which was measured to be as high as 40% while still having $\sim 20\%$ transmission. By extrapolating these findings to a situation where the slab would be so thick that the pulse would be attenuated down to 1% we reach a fractional pulse advancement of ~ 2, which is neighbouring the theoretical limit for this value. No other material so far is offering such a promising system to test this

limit and it might be interesting to pursue this path in the future.

High intensity probing

In addition to the weak intensity probing scheme we also explored experimentally the field of high intensity response. So far we have only acquired three data points for $s \approx 0.01$, 1 and 8, which does not allow a quantitative conclusion, yet. Even with those three measurement points the variation in linewidth change was indicating that the saturation intensity is not constant with respect to the density ρ of the sample. I was able to confirm this assumption by independently measuring the saturation intensity $I_{\mathrm{sat}}(\rho)$ by varying the probe intensity and measuring at different moments of a time of flight experiment. With this experiment we saw that saturation intensity drops by roughly a factor 3 when the peak density drops from $6 \times 10^{12}\,\mathrm{atoms\,cm^{-3}}$ to $1 \times 10^{12}\,\mathrm{atoms\,cm^{-3}}$. Sadly this sudden drop is undersampled which does not allow to extract more quantitative information.

Outlook

Other groups have recently picked up interest in this topic and so the group of Dalibard has conducted measurements on a slab geometry [89]. This configuration, together with a homogeneous density distribution is especially relevant as it alleviates the uncertainty over the influence of the geometry of the sample. Even in this ideal, the coupled dipole equations do not fully match the experimental curves.

Another experiment was performed in JILA [22] in the context of atomic clocks. They studied the different responses of a narrow and a broad resonance ($\Gamma = 7.5\,\mathrm{kHz}$ and $\Gamma = 32\,\mathrm{MHz}$ respectively) in Strontium 88 at a density of $n\lambda\!\!\!^{-3} \approx 10^{-3}$. They find that the coupled dipole model explains the shift of the resonance for the broad transition well, but not the too large shift of the narrow transition. They also conducted a detailed theoretical study in which they conclude that none of the available theories can explain the density dependent shift they observed [90].

These very recent results corroborate our findings and the inadequacy of the current models to capture the behaviour of dense samples to a full extent. It is clear that further investigation is required to single out the factors which cause the disagreement between the existing theories and experiments for the low intensity probing. High-intensity probing poses a challenge of yet another league as a fully quantum mechanical

approach is required. The computational intensiveness of brute-force models leaves systems beyond ~ 30 atoms completely out of reach of any computer system available nowadays, thus completely new algorithms have to be developed.

Appendices

Appendix A

Geometry dependent spectra

Here are the simulated results when changing our sample from an aspect ratio of 1:6 to 1:1. First increasing the short axis to match with the long axis and the second plot where the long axis is shrunk to match the short axis. In both cases the number of atoms were kept constant at 200 particles. The initial axes have the following size: $(a_\perp, a_\mathrm{z}) = (0.2, 1.2)\mu$m.

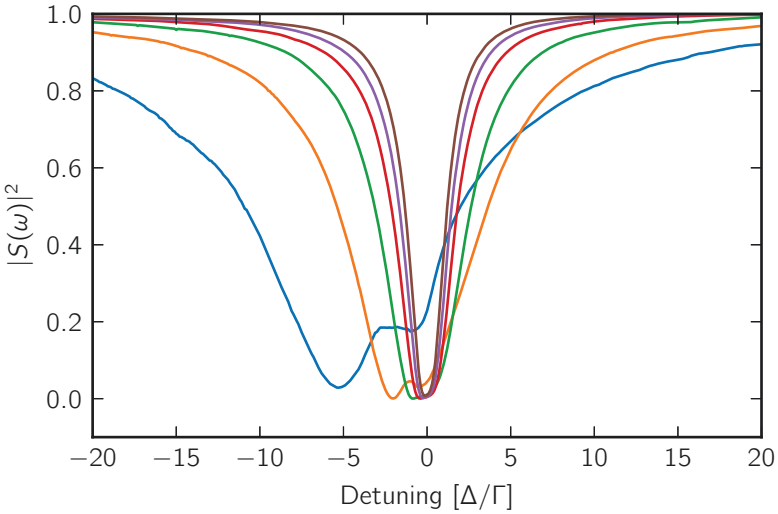

(a) blue: $(a_\perp, a_\mathrm{x}) = (0.2, 1.2)\mu\mathrm{m}$, orange: $(a_\perp, a_\mathrm{x}) = (0.4, 1.2)\mu\mathrm{m}$, green: $(a_\perp, a_\mathrm{x}) = (0.6, 1.2)\mu\mathrm{m}$, red: $(a_\perp, a_\mathrm{x}) = (0.8, 1.2)\mu\mathrm{m}$, purple: $(a_\perp, a_\mathrm{x}) = (1.0, 1.2)\mu\mathrm{m}$, brown: $(a_\perp, a_\mathrm{x}) = (1.2, 1.2)\mu\mathrm{m}$

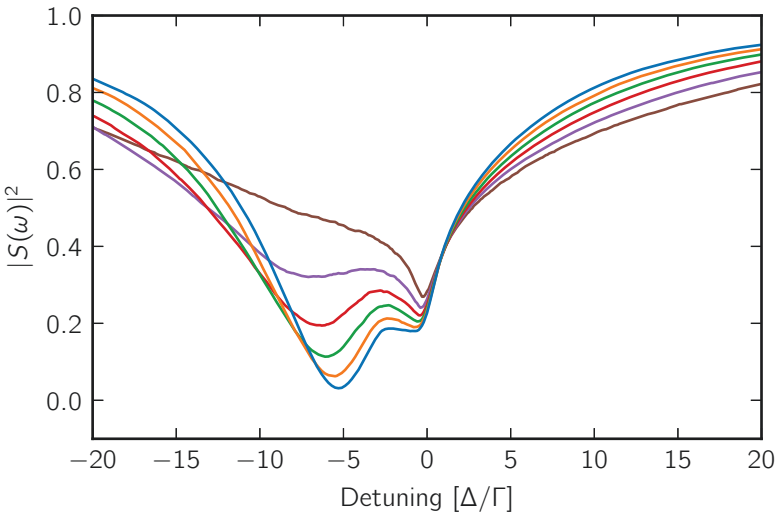

(b) blue: $(a_\perp, a_\mathrm{x}) = (0.2, 1.2)\mu\mathrm{m}$, orange: $(a_\perp, a_\mathrm{x}) = (0.2, 1.0)\mu\mathrm{m}$, green: $(a_\perp, a_\mathrm{x}) = (0.2, 0.8)\mu\mathrm{m}$, red: $(a_\perp, a_\mathrm{x}) = (0.2, 0.6)\mu\mathrm{m}$, purple: $(a_\perp, a_\mathrm{x}) = (0.2, 0.4)\mu\mathrm{m}$, brown : $(a_\perp, a_\mathrm{x}) = (0.2, 0.2)\mu\mathrm{m}$

Figure A.1.: Geometry dependent spectrum

Appendix B

Results of the Pulse propagation

Comparison of ab initio calculated transfer function response and measurement.

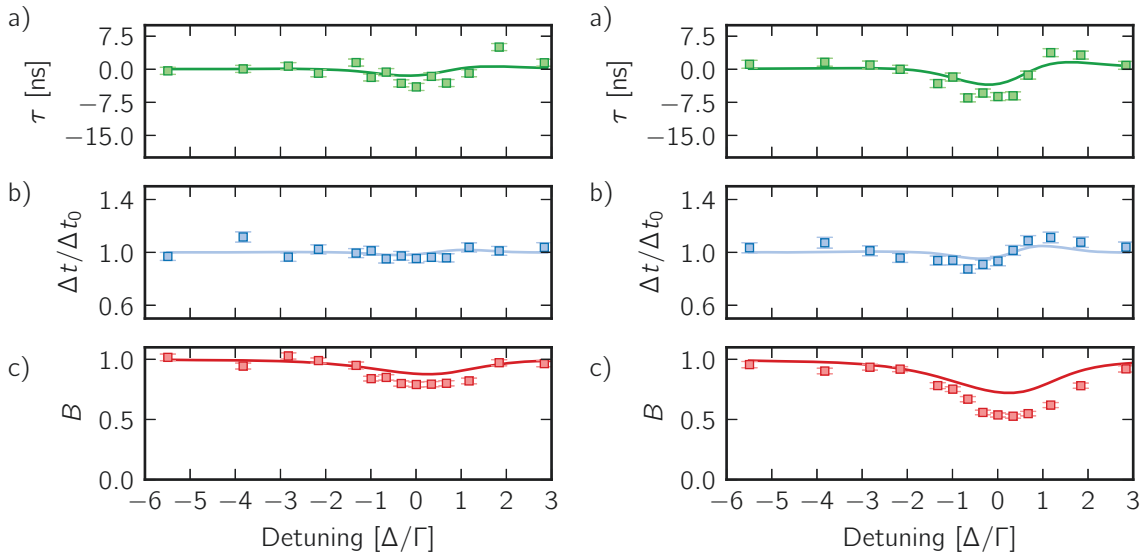

(a) 12 Atoms **(b)** 30 Atoms

Figure B.1.: For each group of figures corresponding to a given number of atoms: c) Ratio between the temporal width Δt of the pulse after transmission, and the width Δt_0 of the incident pulse measured in the absence of atoms. The markers are obtained from fits of the measured transmitted pulses. The solid lines are obtained from fits of the calculated pulses. Error bars are from the Gaussian fits to the data. a) Comparison between the delay τ obtained by fitting the measured pulse (markers) and the one obtained from the calculated pulse (solid line). c) Comparison between the amplitude B obtained by fitting the measured transmitted pulse (markers) and the one obtained from the fit of the calculated pulse (solid line).

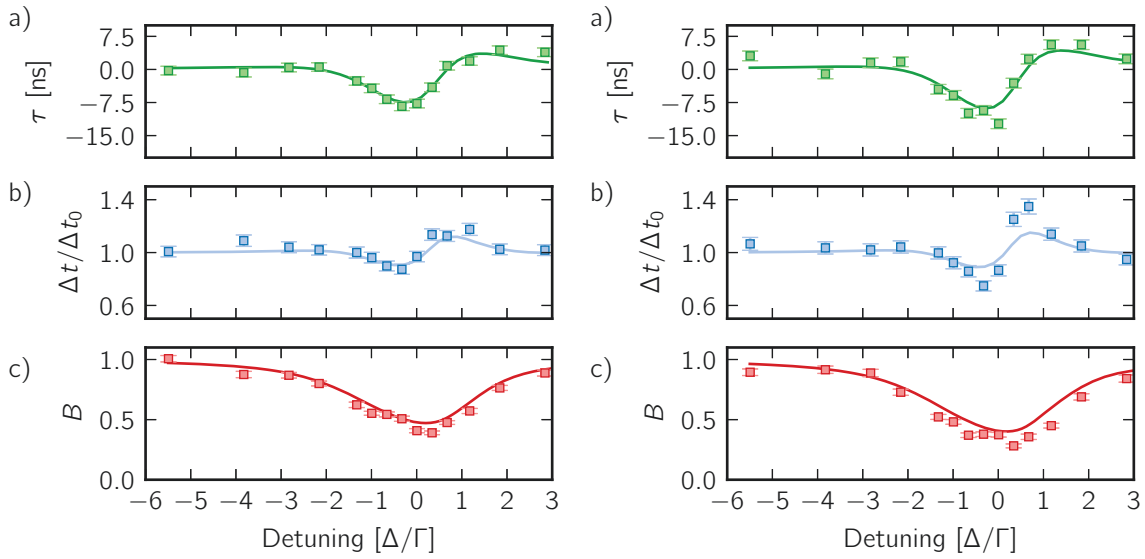

(a) 72 Atoms

(b) 90 Atoms

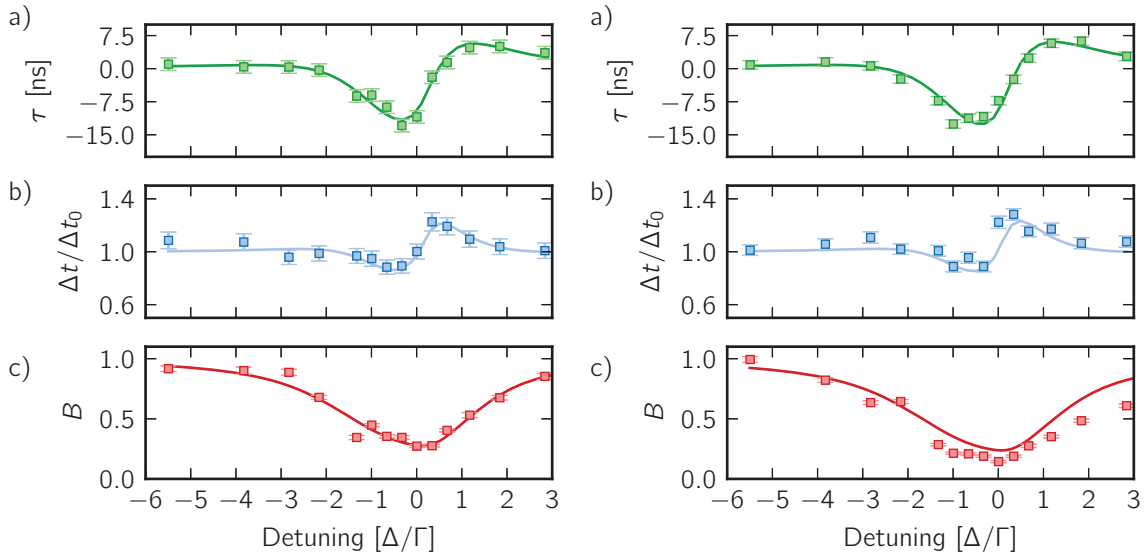

(c) 140 Atoms

(d) 170 Atoms

Figure B.2.: For each group of figures corresponding to a given number of atoms: c) Ratio between the temporal width Δt of the pulse after transmission, and the width Δt_0 of the incident pulse measured in the absence of atoms. The markers are obtained from fits of the measured transmitted pulses. The solid lines are obtained from fits of the calculated pulses. Error bars are from the Gaussian fits to the data. a) Comparison between the delay τ obtained by fitting the measured pulse (markers) and the one obtained from the calculated pulse (solid line). c) Comparison between the amplitude B obtained by fitting the measured transmitted pulse (markers) and the one obtained from the fit of the calculated pulse (solid line).

Appendix C

Parts of the Frequency Offset Lock

All parts are from the company *Mini-Circuits*.

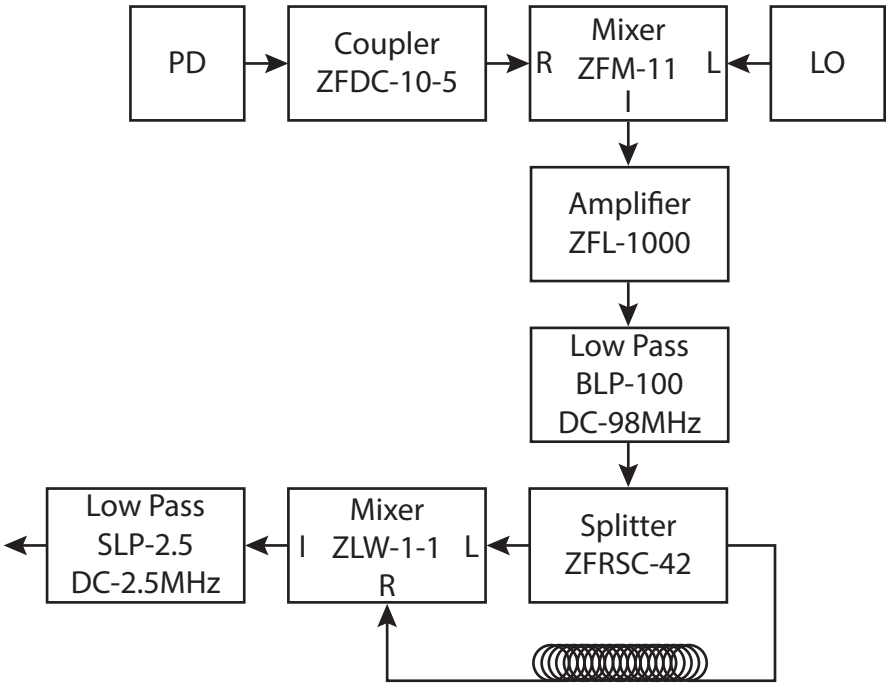

Figure C.1.: Schematic of the frequency offset lock together with the part names.

Appendix D

Fit Results of Figure 5.6

Fitting parameters for the response of a 2-level system with respect to the number of atoms.

Fit result for the amplitude A measured by the APD and CCD fitted by $A(N) = 1 - \sqrt{a + (1-a)\exp(-b\,N)}$

	APD	CCD
a	0.01 ± 0.05	0.47 ± 0.09
b	0.03 ± 0.005	0.02 ± 0.01

Fit result for the shift Δ_c/Γ_0 measured by the APD and CCD fitted by $\Delta_c(N)/\Gamma_0 = \alpha + \beta\,N$

	APD	CCD
α	-0.0016 ± 0.05	-0.3 ± 0.1
β	-0.004 ± 0.001	-0.001 ± 0.002

Fit result for the FWHM Γ_c/Γ_0 measured by the APD and CCD fitted by $\Gamma_c(N)/\Gamma_0 = \alpha + \beta\,N$

	APD	CCD
α	1.07 ± 0.01	1.3 ± 0.4
β	0.012 ± 0.002	0.01 ± 0.008

Appendix E

Fit Results of Figure 5.11

Fitting parameters for the response high intensity probing of a 2-level system with respect to the number of atoms. Fit result for the amplitude A measured by the CCD fitted by
$A(N) = 1 - \sqrt{a + (1-a)\exp(-b\,N)}$

	$s \approx 0.01$	$s \approx 1$	$s \approx 8$
a	0.47 ± 0.09	0.34 ± 0.33	0.7 ± 0.4
b	0.02 ± 0.01	0.03 ± 0.03	0.2 ± 0.3

Fit result for the shift Δ_c/Γ_0 measured by the CCD fitted by $\Delta_c/\Gamma_0 = \alpha + \beta\,N$

	$s \approx 0.01$	$s \approx 1$	$s \approx 8$
α	-0.26 ± 0.12	-0.34 ± 0.03	0.2 ± 0.9
β	-0.001 ± 0.002	-0.005 ± 0.0008	-0.003 ± 0.02

Fit result for the FWHM Γ_c/Γ_0 measured by the CCD fitted by $\Gamma_c/\Gamma_0 = \alpha + \beta\,N$

	$s \approx 0.01$	$s \approx 1$	$s \approx 8$
α	1.3 ± 0.4	1.58 ± 0.1	4.5 ± 1
β	0.01 ± 0.008	0.009 ± 0.003	-0.035 ± 0.02

Appendix F

High Intensity Spectra

Measurement results with Lorentzian fit for various atom number at $s \approx 1$ and $s \approx 8$ probe saturation.

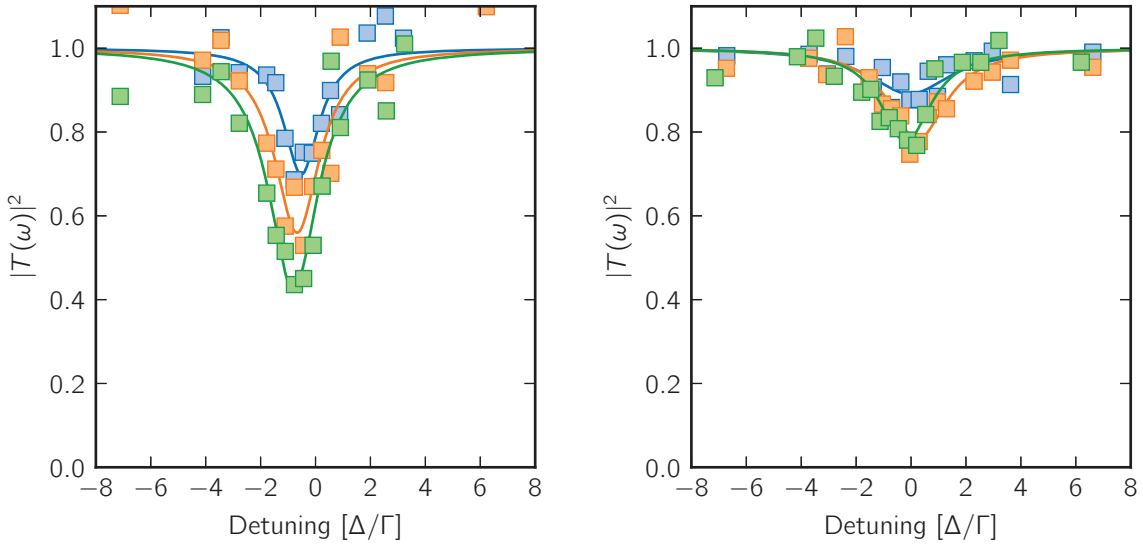

(a) Transmission measured by the CCD for $s \approx 1$. blue = 10 atoms, orange = 45 atoms, green = 70 atoms

(b) Transmission measured by the CCD for $s \approx 8$. blue = 28 atoms, orange = 50 atoms, green = 70 atoms

Figure F.1.: Transmission measurement for higher prober intensity

List of Publications

[1] *"Observation of suppression of light scattering induced by dipole-dipole interactions in a cold-atom ensemble,"* Pellegrino, J., Bourgain, R., Jennewein, S., Sortais, Y. R. P., Browaeys, A., Jenkins, S. D., and Ruostekoski, J., Phys. Rev. Lett. **113**, 133602 (2014).

[2] *"Direct measurement of the wigner time delay for the scattering of light by a single atom,"* Bourgain, R., Pellegrino, J., Jennewein, S., Sortais, Y. R. P., and Browaeys, A., Opt. Lett. **38**, 1963–1965 (2013).

[3] *"Optical resonance shifts in the fluorescence of thermal and cold atomic gases,"* Jenkins, S. D., Ruostekoski, J., Javanainen, J., Bourgain, R., Jennewein, S., Sortais, Y. R. P., and Browaeys, A., Phys. Rev. Lett. **116**, 183601 (2016).

[4] *"Coherent scattering of near-resonant light by a dense microscopic cold atomic cloud,"* Jennewein, S., Besbes, M., Schilder, N. J., Jenkins, S. D., Sauvan, C., Ruostekoski, J., Greffet, J.-J., Sortais, Y. R. P., and Browaeys, A., Phys. Rev. Lett. **116**, 233601 (2016).

[5] *"Polaritonic modes in a dense cloud of cold atoms,"* Schilder, N. J., Sauvan, C., Hugonin, J.-P., Jennewein, S., Sortais, Y. R. P., Browaeys, A., and Greffet, J.-J., Phys. Rev. A **93**, 063835 (2016).

[6] *"Collective resonance fluorescence in small and dense atom clouds: Comparison between theory and experiment,"* Jenkins, S. D., Ruostekoski, J., Javanainen, J., Jennewein, S., Bourgain, R., Pellegrino, J., Sortais, Y. R. P., and Browaeys, A., Phys. Rev. A **94**, 023842 (2016).

[7] *"Propagation of light through small clouds of cold interacting atoms,"* Jennewein, S., Sortais, Y. R. P., Greffet, J.-J., and Browaeys, A., Phys. Rev. A **94**, 053828 (2016).

Bibliography

[1] *"A Pioneer in Anaclastics: Ibn Sahl on Burning Mirrors and Lenses,"* Rashed, R., Isis **81**, 464–491 (1990).

[2] *"Geometry and dynamics in refracting systems,"* Wolf, K. B. and Krotzsch, G., European Journal of Physics **16**, 14 (1995).

[3] Foot, C. J., Atomic physics, Vol. 7 (Oxford University Press, 2005).

[4] *"Single-ion atomic clock with* 3×10^{-18} *systematic uncertainty,"* Huntemann, N., Sanner, C., Lipphardt, B., Tamm, C., and Peik, E., Physical Review Letters **116**, 063001 (2016).

[5] *"Observation of Single-Photon Superradiance and the Cooperative Lamb Shift in an Extended Sample of Cold Atoms,"* Roof, S. J., Kemp, K. J., Havey, M. D., and Sokolov, I. M., Physical Review Letters **117**, 073003 (2016), arXiv:1603.07268 .

[6] *"Superradiance in a Large and Dilute Cloud of Cold Atoms in the Linear-Optics Regime,"* Araújo, M. O., Krešić, I., Kaiser, R., and Guerin, W., Physical Review Letters **117**, 073002 (2016), arXiv:1603.07204 .

[7] *"More Is Different,"* Anderson, P. W., Science **177**, 393–396 (1972), arXiv:1011.1669v3 .

[8] *"A single-atom transistor."* Fuechsle, M., Miwa, J. a., Mahapatra, S., Ryu, H., Lee, S., Warschkow, O., Hollenberg, L. C. L., Klimeck, G., and Simmons, M. Y., Nature nanotechnology **7**, 242–6 (2012).

[9] *"BIPM Annual Report on Time Activities 2015,"* (2015).

[10] *"Systematic evaluation of an atomic clock at* 2×10^{-18} *total uncertainty,"* Nicholson, T., Campbell, S., Hutson, R., Marti, G., Bloom, B., McNally, R., Zhang, W., Barrett, M., Safronova, M., Strouse, G., Tew, W., and Ye, J., Nature Communications **6**, 6896 (2015), arXiv:1412.8261 .

[11] *"Coherent flash of light emitted by a cold atomic cloud,"* Chalony, M., Pierrat, R., Delande, D., and Wilkowski, D., Physical Review A **84**, 011401 (2011), arXiv:1103.6098 .

[12] *"Cooperative emission of a coherent superflash of light,"* Kwong, C. C., Yang, T., Pramod, M. S., Pandey, K., Delande, D., Pierrat, R., and Wilkowski, D., Physical Review Letters **113**, 223601 (2014), arXiv:1405.5413v1 .

[13] *"Direct measurement of the Wigner time delay for the scattering of light by a single atom."* Bourgain, R., Pellegrino, J., Jennewein, S., Sortais, Y. R. P., and Browaeys, a., Optics letters **38**, 1963–1965 (2013), arXiv:1210.0389 .

[14] *"Observation of cooperative Mie scattering from an ultracold atomic cloud,"* Bender, H., Stehle, C., Slama, S., Kaiser, R., Piovella, N., Zimmermann, C., and Courteille, P. W., Physical Review A **82**, 011404 (2010), arXiv:1004.5096 .

[15] *"Observation of a cooperative radiation force in the presence of disorder,"* Bienaimé, T., Bux, S., Lucioni, E., Courteille, P. W., Piovella, N., and Kaiser, R., Physical Review Letters **104**, 183602 (2010), arXiv:1003.3912 .

[16] *"Coherent and incoherent multiple scattering,"* Chabé, J., Rouabah, M.-T., Bellando, L., Bienaimé, T., Piovella, N., Bachelard, R., and Kaiser, R., Physical Review A **89**, 43833 (2014), arXiv:1211.1587 .

[17] *"Phase shift of a weak coherent beam induced by a single atom,"* Aljunid, S. A., Tey, M. K., Chng, B., Liew, T., Maslennikov, G., Scarani, V., and Kurtsiefer, C., Physical Review Letters **103**, 153601 (2009), arXiv:0905.3734 .

[18] *"Far-off-resonance optical trapping of atoms,"* Miller, J. D., Cline, R. A., and Heinzen, D. J., Physical Review A **47**, R4567 (1993).

[19] *"Quantum field theory of cooperative atom response: Low light intensity,"* Ruostekoski, J. and Javanainen, J., Physical Review A **55**, 513 (1997), arXiv:cond-mat/9701087 .

[20] *"Light scattering from a dense and ultracold atomic gas,"* Sokolov, I. M., Kupriyanova, M. D., Kupriyanov, D. V., and Havey, M. D., Physical Review A **79**, 053405 (2009).

[21] *"Lorentz-Lorenz shift in a Bose-Einstein condensate,"* Ruostekoski, J. and Javanainen, J., Physical Review A **56**, 2056 (1997), arXiv:cond-mat/9701088 .

[22] *"Collective atomic scattering and motional effects in a dense coherent medium."* Bromley, S. L., Zhu, B., Bishof, M., Zhang, X., Bothwell, T., Schachenmayer, J.,

Nicholson, T. L., Kaiser, R., Yelin, S. F., Lukin, M. D., Rey, A. M., and Ye, J., Nature communications **7**, 11039 (2016), arXiv:1601.05322 .

[23] *"Cooperative Emission of a Pulse Train in an Optically Thick Scattering Medium,"* Kwong, C. C., Yang, T., Delande, D., Pierrat, R., and Wilkowski, D., Physical Review Letters **115**, 223601 (2015), arXiv:1504.05077 .

[24] *"Maximal refraction and superluminal propagation in a gaseous nanolayer,"* Keaveney, J., Hughes, I. G., Sargsyan, A., Sarkisyan, D., and Adams, C. S., Physical Review Letters **109**, 233001 (2012), arXiv:1208.4309v1 .

[25] *"Observation of suppression of light scattering induced by dipole-dipole interactions in a cold-atom ensemble,"* Pellegrino, J., Bourgain, R., Jennewein, S., Sortais, Y. R. P., Browaeys, A., Jenkins, S. D., and Ruostekoski, J., Physical Review Letters **113**, 1–5 (2014), arXiv:1402.4167 .

[26] *"Cooperative Lamb shift in an atomic vapor layer of nanometer thickness,"* Keaveney, J., Sargsyan, A., Krohn, U., Hughes, I. G., Sarkisyan, D., and Adams, C. S., Physical Review Letters **108**, 173601 (2012), arXiv:1201.5251 .

[27] *"The Feynman lectures on physics, vol. 2: Mainly electromagnetism and matter,"* Feynman, R. and Leighton, R. B., Addison-Wesley (1979).

[28] *"Light scattering in dense mesoscopic cold atomic clouds,"* Bourgain, R., (2014).

[29] *"collective scattering of near-resonant light by dense nano-clouds of cold atoms,"* Pellegrino, J., (2014).

[30] *"Light scattering by a random distribution of particles embedded in absorbing media: full-wave Monte Carlo solutions of the extinction coefficient."* Durant, S., Calvo-Perez, O., Vukadinovic, N., and Greffet, J.-J., Journal of the Optical Society of America. A **24**, 2953–2962 (2007).

[31] *"Optimal superluminal systems,"* MacKe, B., Ségard, B., and Wielonsky, F., Physical Review E **72**, 035601 (2005).

[32] *"Maximum time delay achievable on propagation through a slow-light medium,"* Boyd, R. W., Gauthier, D. J., Gaeta, A. L., and Willner, A. E., Physical Review A **71**, 023801 (2005).

[33] *"Diffraction-limited optics for single-atom manipulation,"* Sortais, Y. R. P., Marion, H., Tuchendler, C., Lance, A. M., Lamare, M., Fournet, P., Armellin, C., Mercier, R., Messin, G., Browaeys, A., and Grangier, P., Physical Review A **75**, 013406 (2007), arXiv:quant-ph/0610071 .

[34] *"Production of sodium BoseEinstein condensates in an optical dimple trap,"* Jacob, D., Mimoun, E., De Sarlo, L., Weitz, M., Dalibard, J., and Gerbier, F., New Journal of Physics **13**, 65022 (2011), arXiv:1104.1009 .

[35] *"Sub-Poissonian atom-number fluctuations using light-assisted collisions,"* Sortais, Y. R. P., Fuhrmanek, A., Bourgain, R., and Browaeys, A., Physical Review A **85**, 035403 (2012), arXiv:1111.5203 .

[36] *"From single to many atoms in a microscopic optical dipole trap,"* Fuhrmanek, A., (2011).

[37] *"Interfacing light and single atoms with a lens,"* Tey, M. K., Maslennikov, G., Liew, T. C. H., Aljunid, S. A., Huber, F., Chng, B., Chen, Z., Scarani, V., and Kurtsiefer, C., New Journal of Physics **11** (2009), 10.1088/1367-2630/11/4/043011, arXiv:0804.4861 .

[38] *"Rubidium 87 d line data,"* Steck, D. A., (2001).

[39] *"Nobel Lecture: Laser cooling and trapping of neutral atoms,"* Phillips, W. D., Reviews of Modern Physics **70**, 721–741 (1998).

[40] *"Sympathetic cooling of ^{85}Rb and ^{87}Rb: Dependence on trap parameters,"* Bloch, I., Greiner, M., Mandel, O., Hänsch, T. W., and Esslinger, T., Physical Review A **64**, 021402 (2001).

[41] *"Evaporative cooling of a small number of atoms in a single-beam microscopic dipole trap,"* Bourgain, R., Pellegrino, J., Fuhrmanek, A., Sortais, Y. R. P., and Browaeys, A., Physical Review A **88**, 023428 (2013), arXiv:1305.3802 .

[42] *"Optical Dipole Traps for Neutral Atoms,"* Grimm, R., Weidemüller, M., and Ovchinnikov, Y. B., Advances in Atomic, Molecular and Optical Physics **42**, 95–170 (2000), arXiv:physics/9902072 .

[43] *"Combining red and blue-detuned optical potentials to form a Lamb-Dicke trap for a single neutral atom,"* He, X., Yu, S., Xu, P., Wang, J., and Zhan, M., Optics Express **20**, 3711 (2012), arXiv:1011.2687 .

[44] *"Two-dimensional lattice of blue-detuned atom traps using a projected Gaussian beam array,"* Piotrowicz, M. J., Lichtman, M., Maller, K., Li, G., Zhang, S., Isenhower, L., and Saffman, M., Physical Review A **88**, 013420 (2013), arXiv:1305.6102v1 .

[45] *"Principles of Optics M. Born and E. Wolf, 7th (expanded) edition,"* Steen, W., Cambridge University Press **32**, 385 (2000).

[46] *"Theoretical study of light scattering and emission from dense ensembles of resonant dipoles,"* Schilder, N., (2016).

[47] *"Microscopic theory of scattering of weak electromagnetic radiation by a dense ensemble of ultracold atoms,"* Sokolov, I. M., Kupriyanov, D. V., and Havey, M. D., Journal of Experimental and Theoretical Physics **112**, 246–260 (2011), arXiv:1102.3744v1 .

[48] *"Coherent Scattering of Near-Resonant Light by a Dense Microscopic Cold Atomic Cloud,"* Jennewein, S., Besbes, M., Schilder, N. J., Jenkins, S. D., Sauvan, C., Ruostekoski, J., Greffet, J. J., Sortais, Y. R. P., and Browaeys, A., Physical Review Letters **116**, 233601 (2016), arXiv:1510.08041 .

[49] *"Shifts of a resonance line in a dense atomic sample,"* Javanainen, J., Ruostekoski, J., Li, Y., and Yoo, S. M., Physical Review Letters **112**, 113603 (2014), arXiv:1308.6254 .

[50] *"Refractive index of a dilute Bose gas,"* Morice, O., Castin, Y., and Dalibard, J., Physical Review A **51**, 3896 (1995), arXiv:1011.1669v3 .

[51] *"Resonant multiple scattering of light,"* Lagendijk, A. and van Tiggelen, B. A., Physics Reports **270**, 143–215 (1996).

[52] *"Polaritonic modes in a dense cloud of cold atoms,"* Schilder, N. J., Sauvan, C., Hugonin, J. P., Jennewein, S., Sortais, Y. R. P., Browaeys, A., and Greffet, J. J., Physical Review A **93**, 063835 (2016), arXiv:1510.07993v2 .

[53] *"Local fields in solids: Microscopic aspects for dielectrics,"* Schnatterly, S. E. and Tarrio, C., Reviews of Modern Physics **64**, 619–622 (1992).

[54] *"Absorption imaging of a quasi-two-dimensional gas: A multiple scattering analysis,"* Chomaz, L., Corman, L., Yefsah, T., Desbuquois, R., and Dalibard, J., New Journal of Physics **14**, 055001 (2012), arXiv:1112.3170 .

[55] *"Weak localization of light by cold atoms: The impact of quantum internal structure,"* Müller, C. A., Jonckheere, T., Miniatura, C., and Delande, D., Physical Review A **64**, 538041–5380420 (2001), arXiv:quant-ph/0107030 .

[56] *"Experimental Evidence for Recurrent Multiple Scattering Events of Light in Disordered Media,"* Wiersma, D. S., van Albada, M. P., van Tiggelen, B. A., and Lagendijk, A., Physical Review Letters **74**, 4193–4196 (1995).

[57] *"Light propagation beyond the mean-field theory of standard optics,"* Javanainen, J. and Ruostekoski, J., Optics Express **24**, 993 (2016), arXiv:1409.4598 .

[58] *"Perturbation theory of super-radiance. ii. cooperative and non-cooperative level shifts,"* Saunders, R. and Bullough, R., Journal of Physics A: Mathematical, Nuclear and General **1360**, 1360–1374 (1973).

[59] *"Optical Linewidth of a Low Density Fermi-Dirac Gas,"* Ruostekoski, J. and Javanainen, J., Physical Review Letters **82**, 4741–4744 (1999), arXiv:cond-mat/9902172 .

[60] *"Frequency shifts in emission and absorption by resonant systems ot two-level atoms,"* Friedberg, R., Hartmann, S., and Manassah, J., Physics Reports **7**, 101–179 (1973).

[61] *"Cooperative radiation from atoms in different geometries: decay rate and frequency shift,"* Manassah, J. T., Advances in Optics and Photonics **4**, 108 (2012).

[62] *"Physical origin of the Gouy phase shift."* Feng, S. and Winful, H. G., Optics letters **26**, 485–487 (2001).

[63] *"Microscopic lensing by a dense, cold atomic sample,"* Roof, S., Kemp, K., Havey, M., Sokolov, I. M., and Kupriyanov, D. V., Optics Letters **40**, 1137 (2015), arXiv:1412.0577v1 .

[64] *"Interference model for back-focal-plane displacement detection in optical tweezers,"* Gittes, F. and Schmidt, C. F., Optics Letters **23**, 7 (1998).

[65] *"Interferometry of a single nanoparticle using the Gouy phase of a focused laser beam,"* Hwang, J. and Moerner, W. E., Optics Communications **280**, 487–491 (2007), arXiv:physics/0702243 .

[66] *"Depolarization of multiply scattered waves by spherical diffusers: Influence of the size parameter,"* Bicout, D., Brosseau, C., Martinez, A. S., and Schmitt, J. M., Physical Review E **49**, 1767–1770 (1994).

[67] *"Light speed reduction to 17 metres per second in an ultracold atomic gas,"* Hau, L. V., Harris, S. E., Dutton, Z., and Behroozi, C. H., Nature **397**, 594–598 (1999).

[68] *"Controllable optical phase shift over one radian from a single isolated atom,"* Jechow, A., Norton, B. G., Händel, S., Blums, V., Streed, E. W., and Kielpinski, D., Physical Review Letters **110** (2013), 10.1103/PhysRevLett.110.113605, arXiv:1208.5091 .

[69] *"Observation of the nonlinear phase shift due to single post-selected photons,"* Feizpour, A., Hallaji, M., Dmochowski, G., and Steinberg, A. M., Nature Physics **11**, 905–909 (2015), arXiv:1508.05211 .

[70] *"Modern electrodynamics,"* Zangwill, A., (2013).

[71] *"Propagation of a Gaussian light pulse through an anomalous dispersion medium,"* Garrett, C. G. B. and McCumber, D. E., Physical Review A **1**, 305–313 (1970).

[72] *"Linear Pulse Propagation in an Absorbing Medium,"* Chu, S. and Wong, S., Physical Review Letters **48**, 738–741 (1982).

[73] *"Propagation of optical pulses in a resonantly absorbing medium: Observation of negative velocity in Rb vapor,"* Tanaka, H., Niwa, H., Hayami, K., Furue, S., Nakayama, K., Kohmoto, T., Kunitomo, M., and Fukuda, Y., Physical Review A **68**, 053801 (2003).

[74] *"Slow- and fast-light: fundamental limitations,"* Boyd, R. W. and Narum, P., Journal of Modern Optics **54**, 2403–2411 (2007).

[75] *"A systemized view of superluminal wave propagation,"* Withayachumnankul, W., Fischer, B. M., Ferguson, B., Davis, B. R., and Abbott, D., Proceedings of the IEEE **98**, 1775–1786 (2010).

[76] *"Linear response laws and causality in electrodynamics,"* Yuffa, A. J. and Scales, J. A., European Journal of Physics **33**, 1635 (2012).

[77] *"Understanding subluminal and superluminal propagation through superposition of frequency components,"* Guo, W., Physical Review E **73**, 016605 (2006).

[78] *"Causality and the nature of information,"* Wynne, K., Optics Communications **209**, 85–100 (2002).

[79] *"Observation of Backward Pulse Propagation Through a Medium with a Negative Group Velocity,"* Gehring, G. M., Science **312**, 895–897 (2006).

[80] *"Optical pumping in dense atomic media: Limitations due to reabsorption of spontaneously emitted photons,"* Fleischhauer, M., EPL (Europhysics Letters) **45**, 659 (1999).

[81] *"Simple scheme for tunable frequency offset locking of two lasers,"* Schunemann, U., Engler, H., Grimm, R., Weidemuller, M., and Zielonkowski, M., Review Of Scientific Instruments **70**, 242–243 (1999).

[82] *"Collective Lamb shift in single-photon superradiance."* Röhlsberger, R., Schlage, K., Sahoo, B., Couet, S., and Rüffer, R., Science (New York, N.Y.) **328**, 1248–1251 (2010).

[83] *"Superradiance,"* Rehler, N. E. and Eberly, J. H., Physical Review A **3**, 1735–1751 (1971), arXiv:1011.1669v3 .

[84] *"Subradiance in a Large Cloud of Cold Atoms,"* Guerin, W., Araújo, M. O., and Kaiser, R., Physical Review Letters **116**, 083601 (2016), arXiv:1603.07204 .

[85] *"Observation of Superradiant and Subradiant Spontaneous Emission of Two Trapped Ions,"* DeVoe, R. G. and Brewer, R. G., Physical Review Letters **76**, 2049–2052 (1996).

[86] *"Controlled Production of Subradiant States of a Diatomic Molecule in an Optical Lattice,"* Takasu, Y., Saito, Y., Takahashi, Y., Borkowski, M., Ciuryło, R., and Julienne, P. S., Physical Review Letters **108**, 173002 (2012), arXiv:1203.2989 .

[87] *"Precise study of asymptotic physics with subradiant ultracold molecules,"* McGuyer, B. H., McDonald, M., Iwata, G. Z., Tarallo, M. G., Skomorowski, W., Moszynski, R., and Zelevinsky, T., Nature Physics **11**, 32–36 (2014), arXiv:1407.4752 .

[88] *"Vacuum-Induced Processes in Multilevel Atoms,"* Kiffner, M., Macovei, M., Evers, J., and Keitel, C., Progress in Optics **55**, 85 (2010).

[89] *"The two-dimensional Bose Gas in box potentials,"* Corman, L., (2016).

[90] *"Light scattering from dense cold atomic media,"* Zhu, B., Cooper, J., Ye, J., and Rey, A. M., Physical Review A **94**, 023612 (2016), arXiv:1605.06219 .

université PARIS-SACLAY | ÉCOLE DOCTORALE Ondes et Matière (EDOM)

Titre : Réponse optique de nuage Rb87 dense

Mots clés : optique, atomique, dense nuage

Résumé : Cette thèse présente les résultats issus de l'investigation de la réponse optique de la transition D2 du Rubidium 87 en fonction de la densité de l'ensemble atomique. Afin de sonder cette transition nous utilisons un faisceau laser proche de la résonance (780nm) sur un échantillon de Rubidium ultra-froid (100µK). Nous observons ainsi la transmission en fonction de la longueur d'onde pour des densités allant de 10^12 atomes/cm^3 à 10^14 atomes/cm^3. Lorsque la densité augmente, on s'attend à ce que les interactions dipôle-dipôle jouent un rôle de plus en plus important du fait de la proximité des éléments diffusants. Quantitativement, les dipôles induits par le faisceau sonde commencent à jouer un rôle important lorsque la densité n atteint n*(lambda/2Pi)^3 = 1, une densité que nous atteignons dans notre système.
Deux études systématiques seront présentées. La première montre les résultats obtenus pour un système à 12 niveaux, la deuxième pour un système à 2 niveaux obtenu par polarisation de l'ensemble atomique. Les résultats issus de ces études sont ensuite comparés aux théories existantes. La première approche est microscopique et décrit les interactions des dipôles couplés, la deuxième approche, macroscopique, est donnée par l'équation de Clausius-Mossotti.
Les propriétés de propagation d'impulsions à travers ce système sont étudiées et révèlent en particulier un avancement fractionnel de l'impulsion et un indice de groupe inégalés.

Title : Optical response of dense Rb87 clouds

Keywords : optics, atoms, dense clouds

Abstract : This thesis investigates the response of the D2 transition of Rubidium 87 for various densities. To probe this transition we illuminate an ultra cold (100microK) sample of Rubidium 87 with close to resonance of lambda = 780 nm laser light. We observe the transmitted light while scanning the frequency over the atomic resonance. Such a spectrum is taken for peak densities ranging from 10^12 atoms/cm^3 to 10^14 atoms/cm^3. As matter gets denser and denser dipoie-dipole interaction start playing a role due to the close proximity of neighbouring scatteres. These interactions are caused by the probe light induced dipoles and start being important when the density reaches n*(lambda/2Pi)^3 = 1, which for us is the case at the upper end of the explored density range. We start off measuring these transmission data for degenerate 12-level Rubidium 87 and afterwards for Rubidium 87, which we first spin polarize and then by lifting the degeneracy generate an artifical 2-level system. These results are systematically compared to the two available theories. A microscopic one, which is described by coupled dipoles and a macroscopic one the so called Clausius-Mosotti equation. None of the ab initio theories can explain the results obtained during this thesis.The rigerous comparison of the various acquired datasets shows that the data in itself is consistent and relative changes going from a 12-level system to a 2-level system are understood. Additionally we also investigate the pulse propagation behaviour through such a system revealing stunning values for the fractional pulse advancement and the group index.

Université Paris-Saclay
Espace Technologique / Immeuble Discovery
Route de l'Orme aux Merisiers RD 128 / 91190 Saint-Aubin, France